2019

EFFECTS OF DEPOSITIONAL PROCESSES ON STRENGTH AND COMPRESSIBILITY OF SEDIMENTS USING ELASTIC SHEAR WAVE VELOCITY

Wisam Razzaq Muttashar
University of Kentucky, wrmu224@g.uky.edu

Digital Object Identifier: https://doi.org/10.13023/etd.2019.116

Recommended Citation

Muttashar, Wisam Razzaq, "EFFECTS OF DEPOSITIONAL PROCESSES ON STRENGTH AND COMPRESSIBILITY OF SEDIMENTS USING ELASTIC SHEAR WAVE VELOCITY" (2019). *Theses and Dissertations--Earth and Environmental Sciences*. 66.
https://uknowledge.uky.edu/ees_etds/66

STUDENT AGREEMENT:

I represent that my thesis or dissertation and abstract are my original work. Proper attribution has been given to all outside sources. I understand that I am solely responsible for obtaining any needed copyright permissions. I have obtained needed written permission statement(s) from the owner(s) of each third-party copyrighted matter to be included in my work, allowing electronic distribution (if such use is not permitted by the fair use doctrine) which will be submitted to UKnowledge as Additional File.

I hereby grant to The University of Kentucky and its agents the irrevocable, non-exclusive, and royalty-free license to archive and make accessible my work in whole or in part in all forms of media, now or hereafter known. I agree that the document mentioned above may be made available immediately for worldwide access unless an embargo applies.

I retain all other ownership rights to the copyright of my work. I also retain the right to use in future works (such as articles or books) all or part of my work. I understand that I am free to register the copyright to my work.

REVIEW, APPROVAL AND ACCEPTANCE

The document mentioned above has been reviewed and accepted by the student's advisor, on behalf of the advisory committee, and by the Director of Graduate Studies (DGS), on behalf of the program; we verify that this is the final, approved version of the student's thesis including all changes required by the advisory committee. The undersigned agree to abide by the statements above.

Wisam Razzaq Muttashar, Student

Dr. L. Sebastian Bryson, Major Professor

Dr. Edward W. Woolery, Director of Graduate Studies

EFFECTS OF DEPOSITIONAL PROCESSES ON STRENGTH AND COMPRESSIBILITY OF SEDIMENTS USING ELASTIC SHEAR WAVE VELOCITY

DISSERTATION

A dissertation submitted in partial fulfillment of the
requirements for the degree of Doctor of Philosophy in the
College of Arts and Sciences at the University of Kentucky

By

Wisam Razzaq Muttashar

Lexington, Kentucky

Co-Directors: Dr. L. Sebastian Bryson, Professor of Civil Engineering
and Dr. Edward W. Woolery, Professor of Earth and Environmental Sciences

Lexington, Kentucky

ABSTRACT OF DISSERTATION

EFFECTS OF DEPOSITIONAL PROCESSES ON STRENGTH AND COMPRESSIBILITY OF SEDIMENTS USING ELASTIC SHEAR WAVE VELOCITY

Depositional processes are the most critical, complicated conditions that govern sediment properties and their variations, which in turn significantly affect the geotechnical behavior of the sediment. The complexity of depositional and post-depositional processes, which results in a variety of depositional environments, makes constructing a plausible model for the consolidation process of sediments difficult. The mutual influence between the temporal and spatial variation of depositional environments with their resultant physical and mechanical properties cause several compression issues, such as consolidation settlement and land subsidence, which mostly occur in estuarine-riverine regions throughout the world.

The first aim of this study is proposing a new grain-size based scheme to classify unconsolidated inorganic sediments that cover a wide range of natural depositional environments with a special emphasis on fine-grained deposits. The proposed classification depends on the linear relationship between percent Fines and the silt fraction. By combining grain size characteristics and plasticity, the proposed scheme provides further characterization of depositional environments. The proposed scheme extends the utility of the scheme beyond simply classifying the sediment class, towards inferring the potential mechanical behavior of sediments having various Grain Size Distribution (GSD) proportions and mineralogy.

Addressing elastic wave properties as a geotechnical parameter, in particular, shear wave velocities to determine the mechanical behavior of sediments is because shear wave velocities is strongly influenced by the change in those physical state properties during compression and cementation processes. This study presents a continuous function that explicitly uses shear wave velocity to predict the non-linear function of consolidation process ($e-\log p'$).

This approach also defines factors that describe the depositional environment, such as grain size and plasticity limits. These factors are shown to influence and control the $e-\log p'$ relationship. Thus, the resulting function is shown to be applicable to a variety of sedimentary materials.

Also, in this dissertation, elastic shear-wave velocity under critical state framework was employed. A shear wave-based constitutive model was developed that is able to predict the stress-strain behavior of a normally consolidated sediments, under undrained loading. A new power-type relationship that predicts the shear strength behavior and critical stress paths of fine-grained sediments under undrained conditions. Also, it investigates the reliability of the link between input model parameters with the basic properties of a variety of fine-grained sediments. As importance of measuring of elastic wave velocities, a number of soil tests performed during particular construction stages can be reduced and compensated. This reduces the cost of evaluating the stability level, monitoring stress path distributions, and determining undrained shear strength behavior during particular stages of the construction process. The study also provides correlations that can be applied in various fine-grained depositional environments that have weak, fine-grained soil layers, on which the constructions are built.

KEYWORDS: Depositional processes, Sediment Classification, Compressibility behavior, Shear Strain Modeling, Shear Wave Velocity.

Wisam Razzaq Muttashar

April 08, 2019

EFFECTS OF DEPOSITIONAL PROCESSES ON STRENGTH AND COMPRESSIBILITY OF SEDIMENTS USING ELASTIC SHEAR WAVE VELOCITY

By

Wisam Razzaq Muttashar

L. Sebastian Bryson
Co-Director of Dissertation

Edward W. Woolery
Co-Director of Dissertation

Edward W. Woolery
Director of Graduate Studies

April 08, 2019

ACKNOWLEDGMENTS

I gratefully would like to thank the High Committee of Education Development in Iraq, the Iraqi ministry of higher education, and the University of Basrah for granting full financial support and facilities to fulfill the doctoral degree.

I would like to thank all my committee members, L. Sebastian Bryson, Edward Woolery, Zhenming Wang, and Michael McGlue, who provided valuable technical advise related to the research. I especially want to thank my co-advisor Dr. Sebastian Bryson for being not only as an academic advisor but also as a really great friend in my life. His knowledge and life experience have enlightened my way to the best.

I would like to thank the University of Kentucky Earth and Environmental Sciences Department faculty, staff, and graduates students who helped for facilities, technical, and academic advises. Special thanks are given to Dr. Christopher J. Matocha and Ms. Yvonne Thompson in the University of Kentucky and Agriculture Soil Sciences for the XRD analysis, and technical advice regarding the process of the XRD analysis and interpretation.

Finally, I would never forget to thank my parents and my wife for their patiently standing with me during the period of my study.

TABLE OF CONTENTS

LIST OF TABLES

LIST OF FIGURES

CHAPTER 1

Introduction

1.1 PROBLEM SYNOPSIS

Depositional and Post-depositional processes are the most critical, complicated conditions that govern sediment properties and their variations, which in turn significantly affect the geotechnical behavior of the sediment. The various depositional environments are arduous for researchers to model and interpret (Brierley and Fryirs 2013). Issues, such as the soil system instability and deformation processes are very complicated and require multiple disciplines working together to better understand the factors influencing these processes (Vanneste et al., 2014). For instance, rapid deposition of sediments, often result in sediments with low strength and high in situ pore water pressures (Moore 1964, Masson et al., 2006). Excess pore pressure is most likely the primary factor causing instability conditions (Vanneste et al., 2014), specifically in fine-grained sediments with low permeability. Figure 1-1 shows the landslide that occurred at the Nice Airport Site, on the Canary Islands in 1979 (Assier-Rzadkieaicz et al., 2000). The sea bed landslide was caused by the rapid deposition of sediments, which led to significant increases in pore pressure during loading and over-steepening of slopes.

Understanding the depositional processes of the sedimentary environments is a crucial engineering concern. Infrastructures projects specifically developed in estuarine and riverine depositional environments (e.g. oil and gas projects, railway and roads projects, ports, navigational channels, and recreational and housing projects) put demands on scientists and developers to assess better the depositional processes and their factors governing the sediment behavior.

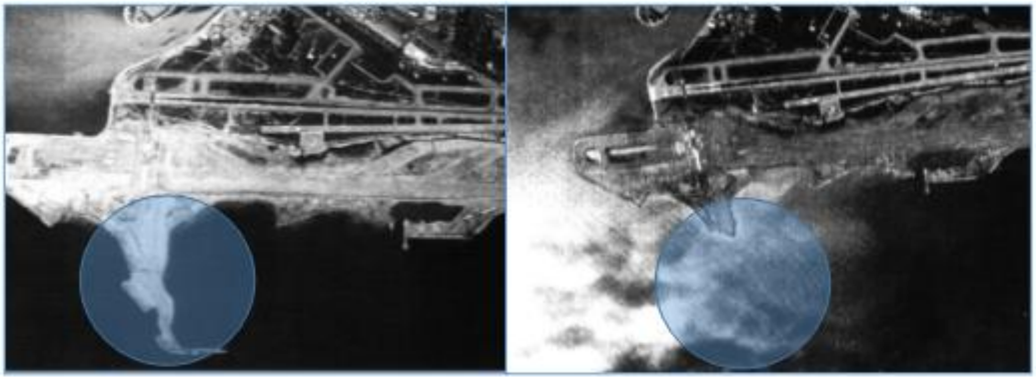

Figure 1-1 Aerial photographs of the construction site (left) before the landslide, and (the right) landslide (Assier-Rzadkieaicz et al., 2000).

1.2 DEPOSITIONAL PROCESSES

Depositional processes refer to initial sedimentary layers that deposit, erode or transport sediment materials. Post-depositional processes refer to the conditions that happen after initial deposition such as, the consolidation of the deposited layers, as well as the bioturbation and re-suspension of surficial sediments. Both depositional and post-depositional conditions alter the geotechnical behavior of sediments, such as strength and compressibility (Geyer and Ashwell 1991).

Depositional processes are complex conditions referring to the geological environment in which sediment is transported via a fluid medium (i.e. wind, water, ice). As kinetic energy is lost during transport, gravity removes solid materials from fluid suspension, accumulating layered sediment deposits. These processes include the consolidation (or geologically called compaction) of the deposited layers. Sediment deposits arise from the interactions of the initial and post-depositional conditions and controlled by complex hydrodynamics. Figure 1-2 shows the interaction of these hydrodynamic processes within a fluvial-to-marine transition zone. The complexity ascribes to the spatially and temporally hydrodynamics interaction of various energy associated with waves, tide, and riverine (fluvial) environments. The transition is a mixed energy area, and includes smaller scale geological changes between estuarine zone and riverine zones, rendering different types of deposits, such as tidal flat, marsh, and sandy sediment deposits. Grain-size distribution is a significant indication of certain hydrodynamic and depositional conditions (Caldwell and Edmonds 2014).

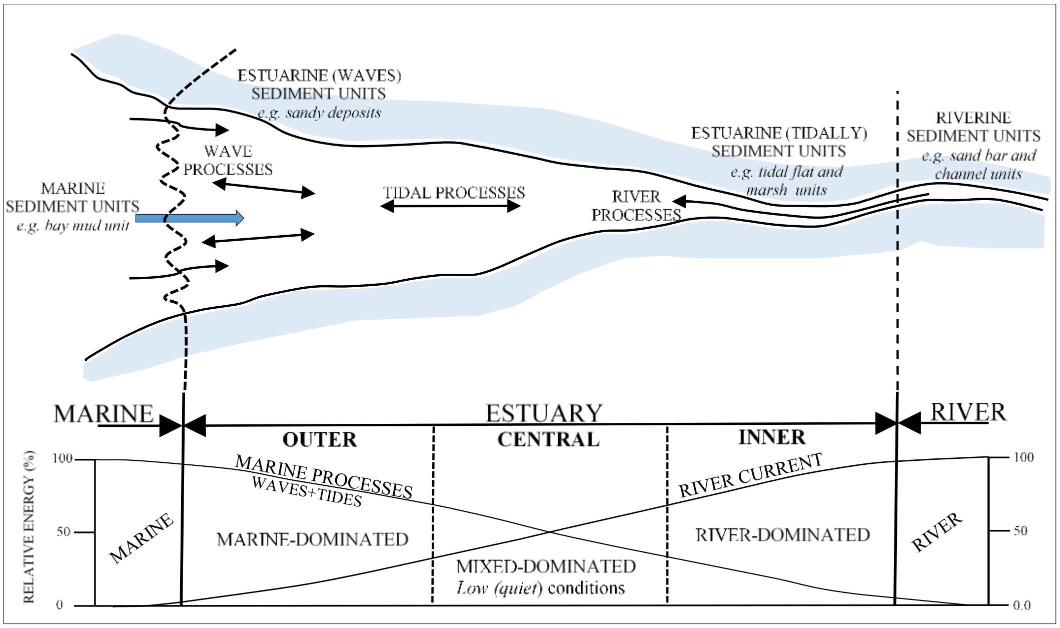

Figure 1-2 Estuarine and river zones with the controlling energy type (tide, wave or current) through the entire transitional area after (Dalrymple et al., 1992).

1.2.1 Grain Size Distribution Characterizing Depositional Environments

Mason and Folk (1958) interpreted different kinds of depositional processes depending on the grain size distribution and their statistical parameters, such as median, skewness, and standard deviation. Stewart Jr (1958) also used grain-size distribution characteristics in a study of sedimentary reflections of depositional environment in San Miguel Lagoon.

Moreover, the percentage of fine particles is most likely a basic function to govern grain-size distributions parameters. Caldwell and Edmonds (2014) identified fine particles as particles sizes that include clay (>0.002 mm) and silt fractions, which both together are called mud particles. Fine particulate matter not only effects sediments behavior by filling and reducing voids of coarse-grained sediments, but also activity of clays may change physical properties of soils such as water content, Atterberg (plasticity) limits, and swelling index. This activity is caused by the content of active or inactive clay minerals. Active clay minerals such as Na-Montmorillonite (bentonite) have much more capability to absorb water and expand their structure than inactive minerals such as Kaolinite and Illite. Skempton (1953) was able to quantify the activity of clay fractions and differentiate among different types of activity of clays depended on the mineralogy. His quantification represents the linear relationship between the plasticity index (PI) of sediments and clay fractions (>0.002). This general linear association between PI and clay fraction covers wide main types of clay minerals. Further, for shear strength, Moore (1964) reported that shear strength increased much more in kaolinite and illite mixtures than montmorillonite mixtures. Thus, the basic properties of sediments, such as grain size, void ratio, density, and water content, which vary with alternating. The depositional conditions primarily affect the mechanical behavior of the geotechnical parameters.

1.2.2 Depositional Processes and Mechanical Sediment Behavior

The complexity of depositional processes resulting in a variety of depositional environments causes difficulties to approach a plausible model that determines the mechanical compression behavior of sediment. Both initial deposits, as a result of the depositional processes, and their compression conditions (or compaction), as a result of the post-depositional processes, influence the compression behavior of the sediment (Wu 1958, Chung and Finno 1992). The compression process is particularly important to ascertain the deformation characteristics of the depositional environments, and this process is also considered a crucial to estimate other important geotechnical parameters, such as the undrained shear strength of sediments. The compression and shear strength parameters change during continuous deposition loading over time (Geyer 2018) because of change in the initial basic properties of the sediment, such as void ratio (or porosity), particle density, and water content (Mitchell and Soga 2005). That means those initial physical properties are key to soil behavior prediction (Bartetzko and Kopf 2007, Marinho 2017) During compression, the change in volume means the amount of water within voids is reduced and dissipated from the sample’s structure, and those properties, (water content, density, and void ratio) change. Attempts (Chung and Finno 1992, Bartetzko and Kopf 2007, Marinho 2017) have addressed geotechnical properties and their alterations due to depositional processes. These studies have been focused on understanding factors that could be controlling the complicated depositional processes to estimate the effects of these processes and their variations on the physical and mechanical properties of sediments.

Studies (Burland 1990, Chung and Finno 1992, Kuecher 1994, Brain et al., 2011, Dipova 2011, Truong et al., 2011) mostly have addressed the relationship between the change in geotechnical properties and variability of sedimentary materials. Since, unfortunately, most of these efforts have been costly and time-consuming, the studies have tended to use the prediction models to represent the compression behavior of sediment. For example, Brain et al., (2011) have advocated a compression behavior approach that could be used to characterize different environmental conditions. Other efforts have used geophysical tools to characterize mechanical sediments behavior.

1.2.3 Elastic Shear Wave-Velocity

Shear wave velocity V_s, as non destructive geophysical method, has been increasingly used to provide reliable, rapid, and inexpensive estimates of the geotechnical parameters (Hardin and Drnevich 1972, Petrakis and Dobry 1987, Santamarina and Cascante 1996, Leong et al., 2009, Irfan et al., 2017, Oh et al., 2017). Shear wave velocity is used as an index to characterize the mechanical behavior of sediments since the shear wave velocity strongly affected by several geotechnical factors, such as fabric, relative density, void ratio (or porosity), effective stresses, stress history, cementation and age of deposit (Aris et al., 2012). Increasing, for an example, the mean effective stress of a particulate material (e.g. sediments) results in an increase in the packing of particles during the compression process, thus researchers (Cha et al., 2014, Oh et al., 2017) have used shear wave velocity V_s to predict the compression process of sediment.

1.3 CONCEPTUAL OVERVIEW

The research believes that grain size distribution characteristics and consistency (plasticity) limits are adequate parameters to establish a classification scheme describing the sedimentary environments for engineering geology application. Also, this study essentially hypothesizes that the effects of the depositional process on the mechanical behavior of sediments can be determined and modeled using shear wave velocity. On another word, The shear wave velocity, including the grain size distribution and plasticity parameters, provides a plausible approach to model, predict, and interpret the compression behavior and stress baths distribution under critical state framework concept.

1.4 OBJECTIVES.

The research serves to advance the current state-of-knowledge in the following manner:

Develop a rational methodology that can be used for plausibly classifying sediment types and to better understand the linkage between sedimentation conditions, sediment types, and physical and mechanical properties of that sediment.

Predict the entire compression behavior ($e - \log p'$) of sediment in normally consolidated states using elastic shear wave velocity. This developed approach uses a formula that essentially depends upon the association between shear wave velocity, mean effective stress, and volumetric change (or void ratio). Since it is believed that the depositional factors influence and control the ($e - \log p'$) relationship, aim to correlate the depositional factors, such as particle grain sizes and sediment types parameters, to the experimental constants resulted from ($V_s - p'$) relation

Predict shear strain behavior and critical stress paths of sediments using elastic shear wave velocity under the critical stress state framework. Accordingly, the study uses the critical state constitutive models to predict shear and pore pressure behavior as functions of shear wave velocity. Moreover, this process requires,

Investigate reliability of the link between basic sediment properties and mechanical behavior of sediment that leads to establishing correlations basically allowing the input parameters of the critical state constitutive models to be predicted.

1.5 CONTENTS OF DISSERTATION

Chapter 1- is the introduction presenting the problem statement, the definition of depositional processes, conceptual overview, and the objectives of the dissertation.

Chapters 2–4 consist of submitted and published papers, and the contents in verbatim.

- Chapter 2- A new unified scheme proposes that identifies sediment types ranging from fine sand to clays. This proposed scheme represents the relationship between percent Fines and silt, and it supposes that the behavior of grain size distribution curves significantly is controlled by the silt portion. Furthermore, an indicative correlation between the sediment mineralogy and plasticity parameters was established. Unifying the proposed diagram with the plasticity parameter (liquid limit) was mathematically calculated and projected in three interfaces (zones) which were low-, intermediate-, and high- plasticity zone. Plasticity was presented as a useful proxy to identify mineralogy of the sediment unit. The proposed scheme extends the utility of the scheme beyond simply classifying the sediment class, towards inferring the potential mechanical behavior of sediments having various GSD proportions and mineralogy. This paper has been submitted for publication to Bulletin of Engineering Geology and the Environment.

Muttashar, W. R., L. S. Bryson, M. McGlue and E. Woolery. 2019. The Integration Grain-Size Distribution and Plasticity Parameters for Better Characterizing and Classifying Unconsolidated Fine-Grained Sediments. Bulletin of Engineering Geology and the Environment. [submitted].

- Chapter 3- determines the effects of depositional processes on the sediments compression behavior using shear wave velocity. The study proposed a general prediction equation that simulates the compression behavior of sediments of normally consolidated-sediments. This developed equation is a decline exponential model that presents the decrease of void ratio (or porosity) as a function of an increase of the mean effective stress. Finding was well matching between the measured consolidation data and the general relationship. In this prediction relationship, the void ratio was a function of shear wave velocity and coefficient of compressibility. This paper was published in Marine Georesources & Geotechnology in November 2018.

  Muttashar, W. R., L. S. Bryson, and E. Woolery. 2018. Determining the effects of depositional processes on consolidation behavior of sediment using shear-wave velocity. Marine Georesources & Geotechnology, 1-12. https://doi.org/10.1080/1064119X.2018.1524953.

- Chapter 4- determine effects of depositional processes on shear behavior of sediments and undrained shear strength parameter by means of seismic shear waves within critical state model framework. In this regard, triaxial tests were conducted under isotropic consolidated undrained triaxial conditions named CIU Triaxial Test to observe the sediment consolidation and shear behavior at various grain size distribution states. This paper has been submitted for publication to Marine Georesources & Geotechnology.

  Muttashar, W. R. and L. S. Bryson 2018. Constitutive Model for Predicting Stress-Strain Behavior of Fine-Grained Sediments using Shear Wave Velocity. Marine Georesources & Geotechnology [submitted].

Chapter 5- Conclusions: This chapter briefly presents the findings and conclusions of the research prescribed in the published and submitted papers, Chapters 2–4.

CHAPTER 2

The Integration Grain-Size Distribution and Plasticity Parameters for Better Characterizing and Classifying Unconsolidated Fine-Grained Sediments

2.1 INTRODUCTION

Modeling and interpreting many temporal and spatial variations in depositional environments can be difficult, particularly within modern sedimentary systems that are influenced by both natural and anthropogenic processes (Brierley and Fryirs 2013). One common measure for characterizing sediments associated with different modern sedimentary environments is grain size (texture). Grain size is typically sensitive to hydrodynamic processes, and varies with relative environmental energy (Dalrymple et al., 1992).

A number of sedimentological and hydromorphic studies (Friedman 1979, Edmonds and Slingerland 2010, Zhang et al., 2015, Allen et al., 2017) have investigated the relationship between grain-size distribution (GSD) and the dominant depositional processes. For instance, For instance, Caldwell and Edmonds (2014) used GSD parameters to indicate depositional conditions, and they reported that the diameter associated with 84 percent passing (D84) was sensitive to changes in grain-size statistical parameters such as median, standard deviation, and skewness. However, those statistical parameters do not consistently distinguish the different types of fine-grained sediments having varying clay and silt contents. The evaluation of fine-grained sediments can be very complicated due to the appreciable influence of clay mineralogy as well.

It is apparent that GSD properties are paramount for classifying and analyzing basic properties of a sediment unit (Cheng and Liu 2015, Erguler 2016). The term “sediment unit”, herein, is the initial sedimentation characterizing inorganic unconsolidated sediment. Many sediment classification systems used for geological, engineering, and agricultural purposes Folk (1980), Flemming (2000), Connor et al., (2004), Blott and Pye (2012) are based on the proportion of grain size. Blott and Pye (2012) reviewed these previous classification schemes and found that the schemes lacked a logical basis in describing the sediment.

These previous studies and classification systems focus on grain size percentages without reference to the composition mineralogy. Yet composition clearly plays an important role in depositional processes history (Net et al., 2002, Garcia-Romero et al., 2005), and the mineralogy has been used in the context of provenance. In engineering applications, consistency limits (also called Atterberg limits) such as the liquid limit (LL) and plasticity index (PI) are used to quantify mineralogy, and to classify the silts from clays of the fine-grained sediments using the traditional plasticity (Casagrade) chart.

In sedimentological perspective, the studies have paid less attention to the consistency limits for inferring mineralogy even though Consistency limits refer to the physical change limits in moisture content of sediment. This characteristic is strongly controlled by mineral types and the percent of silt + clay (hereafter, percent Fines).

The current research hypothesizes that consistency limits (LL and PI) can be used in the study of unconsolidated fine grained sediments to identify most common clay mineral types (e.g., kaolinite, illite, and montmorillonite). The research aims to combine the consistency limits with the proposed grain size scheme. The proposed concept is integrated classification system in this study considered a step forward for environmental and engineering geology in providing detailed characterizations of sediment units, high resolution in the discrimination between silts and clays sediment classes, and with implications for the mechanical behavior of sediments.

2.2 GRAIN-SIZE CHARACTERISTICS

The variation in percent Fines (diameter < 0.075 mm) has been used by other researchers (Edmonds and Slingerland 2010, Caldwell and Edmonds 2014) to model a change in GSD parameters. These studies found that percent Fines has a significant effect on depositional conditions of deltaic environments, and that the actual percentages of clay and silt particle sizes changed, even though the percent Fines in the sediment units remained the same.

2.2.1 Grain-Size Distribution Curve Behavior

Figure 2-1 shows grain-size data for some sedimentary environments in the United States. These data, taken from Hathaway (1971), were plotted to demonstrate the GSD for a broad range of estuarine and associated riverine sedimentary environments. The sediment size ranges from medium-fine sand (coarse-grained sediment) to clay-to-silty clay (fine-grained sediment). The GSD curves show that the behavior of the curves is related to the percent Fines and the change in percentages of the clay fraction (CF) and silt fraction (SF).

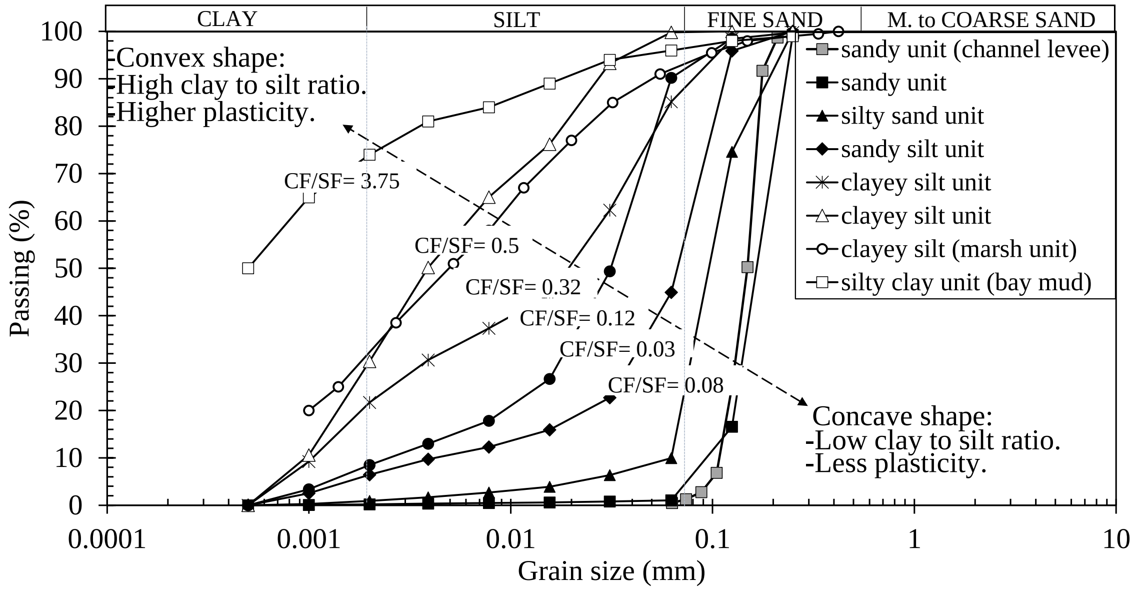

Figure 2-1 Grain-size distribution curves of some sedimentary environments, showing the change in clay and silt percentage and their effect on the GSD shape (data from Hathaway, 1971).

The slope of the silt portion of the GSD curve in Figure 2-1 changes from steeper to flatter as the sediments progress from a coarser grain material to a finer grain material. Analysis of the data revealed that the slope of the GSD curves is fundamentally controlled by the SF and its variability. Therefore, the SF can be used to quantify the slope of the GSD curve. The curvature of the curves also correspond to the texture of the sediment (i.e. coarse grain versus fine grain), but more so, the curvature corresponds to the plasticity of the sediment. For example, the GSD curves transitions from convex for fine-grained sediments to concave for coarse-grained sediments. The convex to concave transition further indicates the progression from higher plasticity sediments to lower plasticity sediments, respectively. From Figure1, it is seen that the clay-to-silt ratio (CF/SF) quantifies the shape transition and the consequent plasticity transition.

2.2.2 *Variation of Silt Fraction (SF) with Respect to Percent Fines*

Figure 2-2 shows the silt fraction (SF) plotted as a function of the percent Fines. In general, the data show a positive association of SF versus percent Fines. However, there is scatter in the data that increases when percent Fines increases, as shown in Figure 2-2a. The data becomes more uniform when sorted based on the CF/SF ratio. The CF/SF ratio appears to govern the slope of the relationship between SF versus percent Fines (Figure 2-2b).

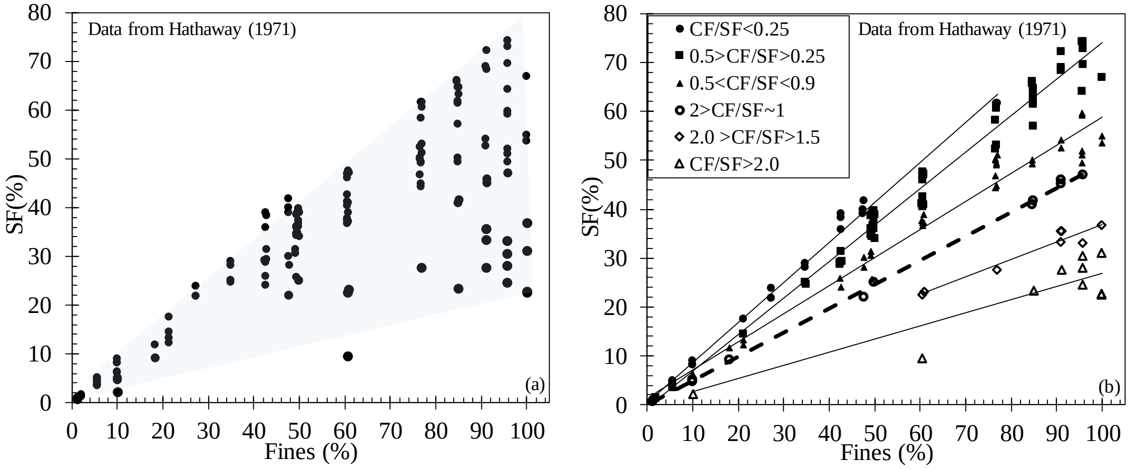

Figure 2-2 Silt fraction (SF) is a function of percent Fines, including an effect of the CF/SF ratio, (a) without sorting and (b) with sorting, depending on the CF/SF ratio.

There is a distinct division in the data when CF is the same as SF (i.e., CF = SF), as shown by the thick dash line in Figure2b. This CF/SF = 1.0 line distinguishes between predominantly silt and predominantly clay sediment zones. Therefore, the zone above the thick dash line (CF = SF) is called the silt zone, and the lower zone is called the clay zone. Thus, this study observes in the literature that SF is a linear function of percent Fines, and the linear regression slope is governed by CF/SF ratio. This study tested this hypothesis by creating synthetic sediments and analyzing their physical GSD properties for classification purposes.

2.3 MEANS AND METHODS

2.3.1 *Mixing Process*

To investigate the relationship of SF versus percent Fines, a mixing procedure was performed in which percent Fines, SF, and CF/SF ratios were controlled. In this procedure, source soils were used to mix and create different sediment properties, in specific, different grain size distribution curves such that each has a different percent Fines, and silt percent (SF). Various CF/SF ratios used were that represented both predominately silt and predominantly clay samples. The specific procedures used to create the samples are as follows:

1. Obtain a GSD curve from selected source soils.
2. Divide all percentages of the finer passing (%) that form the GSD source soil curve into 10, 20, 25, 30, 40, 50, 60, 70, 75, 80, and 90 percent in a spreadsheet.
3. Design a specific GSD curve (new sample) by combing specific percentages of those divided percentages in the previous step.
4. Mix the specified percentages together to create a new designed sample that produces a targeted GSD curve with the required particle sizes percentages.
5. Conduct the grain-size test for the designed sample (the mixture) to obtain a measured GSD curve having the required grain size percentages.
6. Repeat steps 2- 5 for the other designed samples to generate the other new GSD curves.

In this study, five CF/SF ratios were generated at the same percent Fines. This percent Fines was reduced with an addition of fine sand (<425μm), which changed the percent Fines yet allowed the CF/SF to remain constant. In this way, the mixture procedure allowed the CF/SF at a particular percent Fines to be controlled with a degree of precision.

2.3.2 Source Soils Used For Sample Development

The source soils used to create the study mixtures were natural inorganic soils obtained from Fayette, Lee, and Henderson Counties, Kentucky. Table 2-1 gives the index properties of the source materials that were used to make synthetic samples for this study. Grain size, plasticity index (PI) and liquid limit (LL), and specific gravity (G_s) of those source samples were obtained according to the standard ASTM methods (ASTM D4318 1994, ASTM D422 2007). A commercially available kaolin clay sample was included with the three natural inorganic sediment samples. Figure 2-3 shows the GSD curves for the four samples. The GSD indicates that the sediments were predominantly composed of silt- and clay-size particles.

Table 2-1 Index properties of the source sampling used

Soil Location	Kaolin (K)	Henderson County (H)	Fayette County (F)	Lee County (L)
Specific Gravity G_s,	2.63	2.69	2.86	2.7
Liquid Limit (%)	48	25	74.5	55
Plasticity Index (%)	13	8.5	31	25
Fines (%)	100	99.4	86.8	82
Clay Fraction (%)	45	20	74	45

Fines = percentage passing #200 sieve (diameter < 0.075 mm); clay fraction = percentage <0.002 mm.

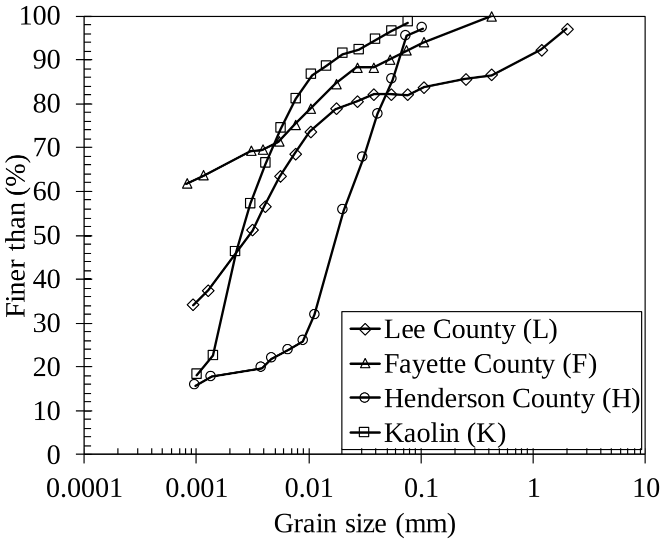

Figure 2-3 Grain-size distribution curves of the source sediments

In addition, fine to very fine sand (0.425mm > diameter > 0.075 mm) was used as additional source material for the mixing process. The sand was from Ohio River fluvial deposits without appreciable amount of organic matter. This material provided selected particle sizes that are used for controlling sand percentage throughout the mixing procedure.

2.3.3 Resultant Grain-Size Distribution Curves

Figure 2-4 shows the different designed GSD curves. The samples represent fine-grained sediments ranging between fine sand and silty clay. These samples have grain size characteristics consistent with some specific estuarine sediment units such as channel-levee and bay mud. Although there were trace amounts of fine sand particles, the sediment adequately simulated environments representative of most riverine and estuarine deposits.

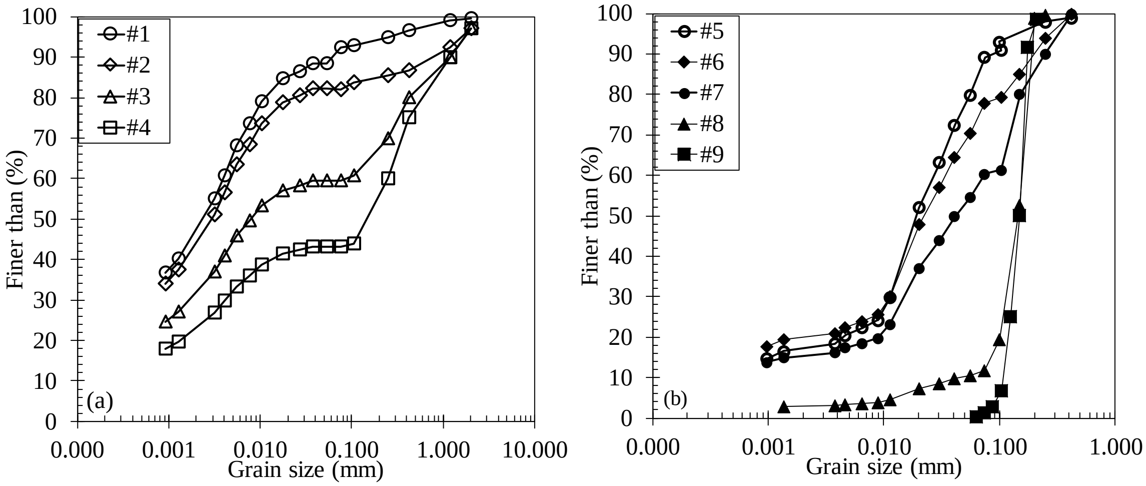

Figure 2-4 The designed grain-size distribution curves show the GSD behavior of sediment having different percent Fines, in which (a) are convexity shapes when (CF/SF) equals or is greater than 1.0, while, (b) being in concavity shapes when (CF/SF) is lower than 1.0.

Table 2-2 summarizes the grain-size parameters for each sample. The broad range of values in the table was used to depict variations in sedimentary conditions between fine-grained and coarse-grained sediments and to determine which grain-size factor best captures those variations. It is noted that the variation in the CF/SF ratio corresponds to a transition in the shape of the GSD curves, which progresses from convexity to concavity. This transition also correspond to the sediment progressing from higher plasticity clay to lower plasticity silt.

Table 2-2 Grain-size parameters of the samples developed for this study.

Sample#	Fines (%)	CF/SF	Sediment Type
1	91.5	1.1	Silty clay
5	90	0.23	Clayey silt
2	82	1.2	Sandy silty clay
6	77	0.23	Sandy clayey silt
3	60	1.1	Sandy clayey silt
7	60	0.38	Clayey silty sand
4	44	1.2	Clayey silty sand
8	19.5	0.27	Silty sand
9	4	N/P	Fine sand

2.4 DEVELOPMENT OF SF-FINES MODEL

Figure 2-5 shows SF as a function of percent Fines for the test samples, sorted according the CF/SF ratio. Sediment units, specifically fine-grained sediments, could not be distinguished clearly when the CF/SF ratio was neglected. CF/SF = 1 represents the interface in which fine sediments have equal amounts of silt and clay fractions. A CF/SF ratio greater than 1.0 indicates that the sediment is predominantly clay. Conversely, a CF/SF ratio less than 1.0 indicates that the sediment is predominantly silt. Linear regressions show a strong correlation between these three grain-size parameters. The slopes of the regression lines reflect changes in the CF/SF ratio.

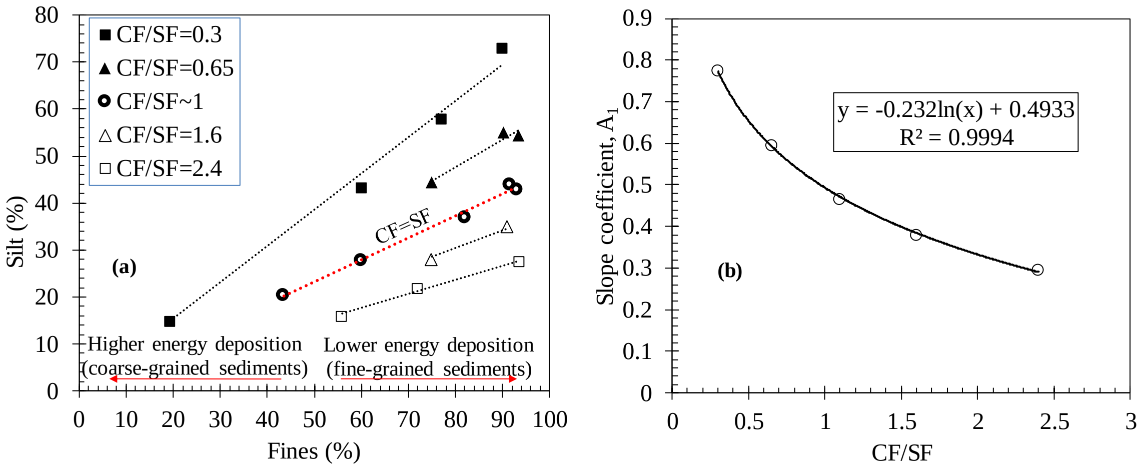

Figure 2-5 The proposed scheme, (a) distinguishes between the different percentages of CF/SF for various fine-grained sediments; (b) shows CF/SF ratio controls the slope of the linear relation between percent Fines and SF.

The regression lines appear to have zero intercept along the SF axis, which indicates pure sand sediments, with no percent Fines. This suggests high-energy conditions during deposition, resulting in well-sorted sediments (or poorly graded soils). As the percent Fines increases, the sorting decreases (i.e. well graded soils), which reflects a decrease in the energy level of depositional conditions. The quieter depositional energy, the higher the percent Fines, and the poorer sorting of sediments. Figure 2-5a also differentiates between silt-dominated fine sediment and clay-dominated units. The general equation that describes the sediment units is:

$$SF = A_1 \left[Fines(\%) \right] \tag{2-1}$$

The slope coefficient A_1 is of particular importance, as it describes the relative energy of deposition. Steep slope coefficients correspond to high relative energy conditions relating to wave, tidal, or fluvial conditions that are responsible for depositional processes. Because the slope coefficient smoothly correlates to the CF/SF ratio, the CF/SF ratio can be inferred to describe the relative energy of deposition.

Relating the slope coefficient to the CF/SF ratio provides a means to quantify the relative energy. Figure 5b shows the slope coefficient as a function of the CF/SF ratio. The figure indicates that a logarithmic function best describes the relationship. The expression for the slope coefficient is given as:

$$A_1 = 0.4932 - 0.232\ln\left(\frac{CF}{SF}\right) \tag{2-2}$$

2.4.1 *Reference Classification Scheme Delineation*

Figure 6 is the scheme that presents the interaction of the percent Fines, SF, and CF/SF data. This interaction allows better delineation of regions of high and low energy deposition, regions of coarse- and fine-grained sediments, and different sediment units.

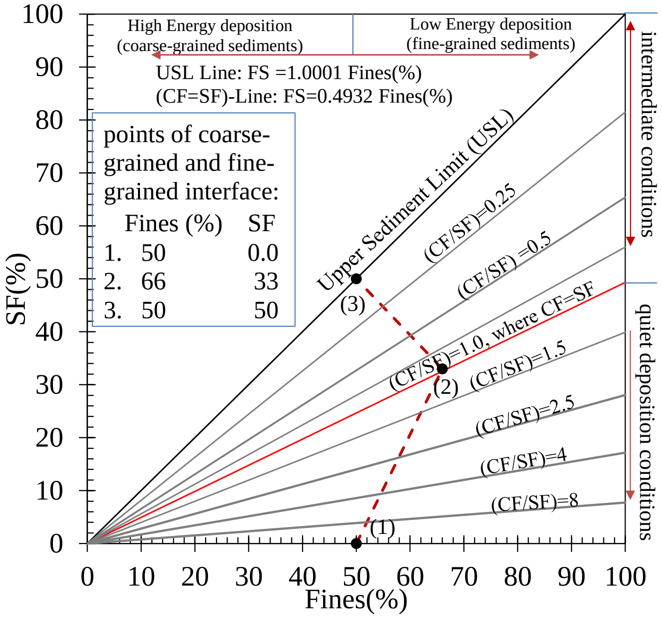

Figure 2-6 Reference scheme for determining sediment type.

In Figure 2-6, the interface between the silt and clay zones is represented by setting CF/SF = 1.0 in Equation 2-2 and then combing with Equation 2-1. The resulting equation is given in Equation 2-3 as:

$$SF = 0.4932 \times Fines(\%) \tag{2-3}$$

Indicative CF/SF ratio: The CF/SF ratio differentiates different depositional conditions and degrees of the predominant energy relative to the CF/SF = 1 line. A CF/SF ratio that is greater than 1.0 (below the CF = SF line) is indicative of a mostly quiet depositional environment, typically associated with predominantly clay sediments, whereas a CF/SF ratio that is less than 1.0 (above the CF = SF line) represents predominantly silt sediment with intermediate depositional conditions.

Upper Sediment Limit line (USL): No data plotted at a CF/SF ratio above approximately 0.11, which represents high percentages of silt within the percent Fines. The upper limit was designated the Upper Sediment Limit (USL) line (Figure 2-6) and is the condition in which the SF is roughly equal to the percent Fines (Equation 2-4):

$$SF = Fines\left(\%\right) \tag{2-4}$$

Fine-Coarse Interface: The interface between fine-grained and coarse-grained sediments is prismatic (red dashed line) toward the fine-grained sediment side, as shown in Figure 2-6. The process that was followed to delineate this coarse-fine interface assumes that the fine-grained sediments have a sand percentage lower than the silt or clay percentage, and sediments are either predominantly silt or predominantly clay. The interface is not a vertical line at 50 percent Fines for sediments with a mixture of grain sizes ranging from fine sand to silt to clay. To clarify, if a sample has 40 percent sand and 60 percent Fines, the sample is classified as fine-grained sediment because it has more than 50 percent Fines. However, if the percent Fines is a combination of 30 percent silt and 30 percent clay, each of these percentages would be less than the percentage of sand (40 percent); in this case, the sample would be classified as coarse-grained sediment, even though the percent Fines is greater than 50 percent. This means there is a non-vertical interface between fine- and coarse-grained sediments in the current SF-Fines scheme. To identify this critical interface on the scheme, the study looked at critical points in each sample in which the sand percentage was equal to or greater than the clay percentage, and also equal to or greater than the silt percentage. The SF and percent Fines were subsequently determined for these critical grain-size points to locate them on the scheme and delineate the coarse-fine interface. The three critical points, shown in the Figure 2-6 (shown as Points 1, 2, and 3 in the figure), create the fine-sand interface. Table 3 gives the coordinates of the critical points in terms of Sand percentage, SF, CF, and percent Fines. The midpoint has SF = CF = 33 percent (e.g., fines = 66 percent), and has sand = 34 percent, could be classified as coarse-grained sediment (the sand zone). This is because the percentage of sand (34 percent) is greater than the percentage of silt (33 percent) and also greater than the percentage of clay (33 percent). This point is most likely considered the inflection point of the interface line, as shown in Point #2 in Figure 6 and Table 2-3.

Table 2-3 Critical points used to identify the fine-sand interface.

No.	Sand (%)	Silt, SF, (%)	Clay, CF,(%)	Fines (%)	Notes
1.	50	0.0	50	50	The first point on the horizontal axis
2.	34	33	33	66	The midpoint on CF = SF line
3.	50	50	0.0	50	The point on the Upper Soil Limit line

The additional points required to delineate the coarse-fine interface on the classification scheme, are given in Table 2-3 as Point #1 and Point #3. Point #1 had 50 percent clay (CF), 0 percent silt (SF), and 50 percent sand, whereas Point #3 had CF = 0.0 percent, SF=50 percent, and sand= 50 percent. As a result, the interface represented by these three points forms the boundary between the coarse-grained sediments (sand zone) and the fine-grained sediments.

2.5 ESTABLISHING OF SEDIMENT-TYPE ZONES

Figure 2-7 introduces six sediment-type zones, which are classified and named depending on the limits between the interfaces, CF = SF line, and the fine-coarse line. In general, the nomenclature of (Blott and Pye 2012) was used to name each sediment units. The symbols s, si, and c are used to indicate sand, silt, and clay components, respectively. The uppercase characters (S, SI, and C) indicate the largest components, whereas the lowercase characters are descriptive of the secondary component. For example, if the percentages of a component are sand = 20 percent, silt = 50 percent, and clay = 30 percent, then the sediment class is sandy clayey Silt (scSI).

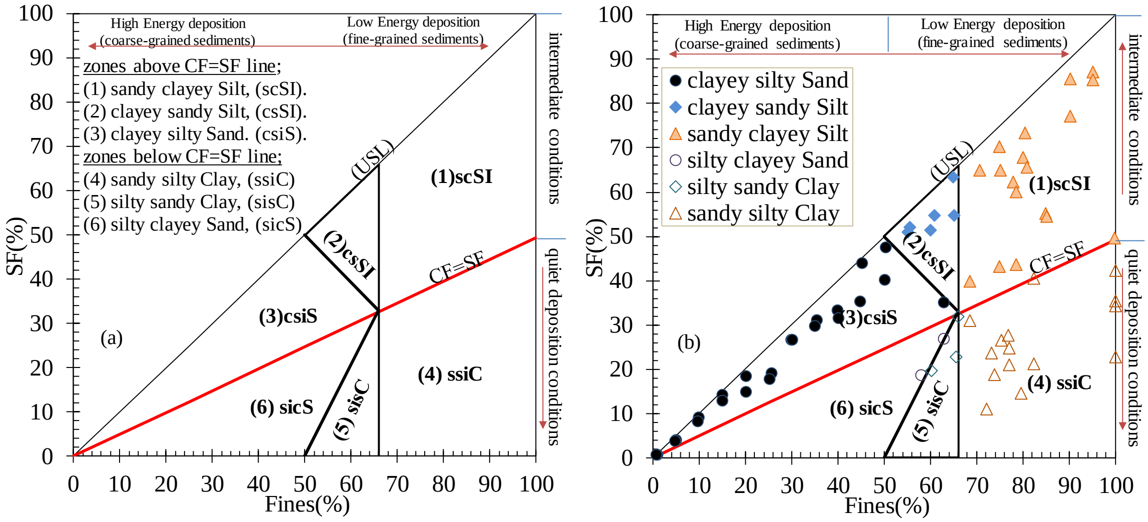

Figure 2-7 Fines-SF scheme showing (a) the six sediment-type zones classified and named depending on the limits between the interfaces, CF = SF line, and the fine-coarse line, (b) Example of identification of the type of sediments (data from Hathaway, 1971).

Three zones are above the CF = SF line: (1) sandy clayey Silt (scSI), (2) clayey sandy Silt (csSI), and (3) clayey silty Sand (csiS). The other three zones, located below the CF = SF line, are (4) sandy silty Clay (ssiC), (5) silty sand Clay (sisC), and (6) silty clayey Sand (sicS). Samples located on the scheme boundaries have two sizes of particles. For instance, a sample located on the upper boundary on USL is named silty Sand (siS) or sandy Silt (sSI), depending on whether it is below or above the fine-coarse interface, respectively. This is because the clay percentage equals zero at USL. For the sample having 100 percent Fines, which is located on the right vertical axis in the scheme, would be called silty Clay (siC) or clayey Silt (cSI), depending on whether it is located below or above the CF = SF line, respectively, where sand equals zero.

Figure 2-7b is an example of using the proposed scheme to identify the type of sediments. From literature, 74 samples were selected and plotted. The samples represent different estuaries in different parts of the United States. The samples distributed on the scheme were classified according to the six sediment classes. Distribution of the samples corresponds with the type of sediment and energy conditions. Samples that have percent Fines lower than 20 percent and SF greater than 20 percent, trending toward the zero intercept, came from high-energy conditions and reflected well-sorted (poorly graded) sediment. These groups are mainly sandy sediment with very small amounts of silt and clay. Conversely, samples with high percent Fines reflect low to intermediate energy conditions. Samples having CF/SF ratio >1.0 reflect low-energy levels of deposition, which represent ssiC and sisC zones, whereas samples having CF/SF ratio <1.0 most likely reflect intermediate depositional conditions, which represent scSI and scSI zones. The data were well represented and plausibly described the type of sediments in the proposed classification. The percent Fines versus SF scheme allows the six sediment classes based on grain size distribution proportions to be identified. This accomplishment, however, needs to be integrated and combined with consistency (Atterberg) limits for further discrimination of these six sediment classes. Herein, the next challenge in this study was to present the sediment plasticity in SF-Fines space.

2.6 CONSIDERATIONS FOR PLASTIC FINES

Plasticity indices such as Liquid limit (LL) and plasticity index (PI), describe the consistency of fine-grained sediment at specific water content. These limits indicate the capacity of a sediment to absorb water, which relates significantly to the mineralogy of the sediment. A high PI implies a high percentage of active clay minerals (i.e., clay minerals with a greater capacity to absorb water), whereas a low PI implies the converse. The activity of clay, A is a useful parameter to classify the predominant minerals in the sediment. The activity A is simply expressed as the ratio of the plasticity index to the amount of clay fraction (Skempton 1953), as expressed in Equation 2-5. Mitchell and Soga (2005) classified the major mineralogy groups based on A. Table 2-4 shows the activity of these major groups of sediment.

$$A = \frac{PI}{CF(\leq 2\mu)} \tag{2-5}$$

Table 2-4 Activity of clay minerals after (Mitchell and Soga 2005).

Mineral	Activity *(A)*	Group Type
Montmorillonite	≥1.0	Platey minerals
Illite	(0.5-1)~ (0.75)	
Kaolinite	0.5	
Halloysite	0.5	Non-platey minerals (not included in this study)
Attapulite	0.5-1.2	
Allophane	0.5-1.2	

Polidori (2009) investigated the interaction of PI, LL, and CF for fine-grained soils. The researcher reported that the LL could be described as a function of the CF. Given that the PI is simply the LL minus PL, Equation 2-6 represents the association between CF and plasticity parameters (Polidori 2009). This expression facilitates using plasticity with the grain-size scheme (Figure 2-8) to develop a unified scheme that considers mineralogy.

$$PI = 0.96 \cdot LL - \left(0.26 \cdot CF + 10\right) \tag{2-6}$$

Since $PI = A \cdot CF$, Equation 2-6 can be rearranged:

$$LL = 1.04\left[\left(A \cdot CF\right) + \left(0.26 \cdot CF + 10\right)\right] \tag{2-7}$$

The current study used Equation 2-7 to estimate the interface between high and low plasticity, which is at $LL = 50$ percent according to the Unified Soil Classification System (USCS). Equation 7 was used to identify the points having $LL = 50$ percent in the proposed scheme and to delineate the high-low interface (herein called the 50 percent-LL line). Recognition of the high- and low-plasticity zones in the SF-Fines scheme established an associated scheme that characterizes the type of sediment units and their plasticity level. Providing a scheme for sediment classification by grain size and plasticity parameters is a practical way to identify the sediment type and its predominant clay minerals.

However, Equation 2-7 does not result in a unique 50 percent-LL line because of the different clay activity values used. The 50 percent-LL line will change, based on the clay activity value. From Table 2-4, the values A = 1, A = 0.75, and A = 0.5 reflect sediments dominated by montmorillonite, illite-montmorillonite, and kaolinite-illite, respectively. These values represent the three main platey minerals that constitutes the majority of sediments. Thus, the range of clay activity of major mineral groups (0.5, 0.75, and 1.0) allowed three 50 percent-LL lines to be established. For example, the interface for the kaolinite-illite clay minerals was established by substituting $A = 0.5$ and $LL = 50$ percent into Equation 2-7 and re-writing the CF term as $CF = Fines\left(\%\right) - SF$. The resulting equation written in terms of SF yields the 50 percent-LL line equation (Equation 2-8) corresponding to sediment predominated by Kaolinite-illite clay minerals.

$$SF = Fines\left(\%\right) - 50.1 \Rightarrow \left(A \le 0.5\right) \tag{2-8}$$

Table 2-5 gives the equations that delineate the three 50 percent-LL linear lines for each type of mineral group.

Table 2-5 exhibits the equations that delineate the three 50 percent -LL lines.

Type of Sediment Group	Activity *(A)*	Equations Delineating 50 Percent-LL Lines
Kaolinite-illite predominant sediment	≤ 0.50	(a-b): $SF = 1.0879 Fines(\%) - 59.472$
Illite-montmorillonite predominant sediment	0.75 (0.5-1)	(c-d): $SF = 1.1566 Fines(\%) - 52.836$
Montmorillonite predominant sediment	> 1.00	(e-f): $SF = 1.1099 Fines(\%) - 39.967$

Figure 2-8 shows the three 50 percent-LL lines delineating clay mineral groups applied to the sediment zone graph presented previously as Figure 2-7. In Figure 2-8, the Kaolinite-illite group is given as Line (a-b); the Illite-montmorillonite group is given as Line (c-d); and the Montmorillonite group is given as Line (e-f). Also, given that the 50 percent-LL line represents the interface between high plasticity and low plasticity minerals, Figure 2-8a shows that zones below the 50 percent-LL line represents high plasticity, while zones above the line represents low plasticity.

An observation of this study was that many estuarine and riverine sediments contain clay minerals of medium to low plasticity. Therefore, to further distinguish the clay minerals that plot above the 50 percent-LL lines, the 30 percent-LL lines were also established. The

30 percent-LL lines were determined using the same process used for determining the 50 percent-LL lines, with the exception that $LL = 30$ percent was substituted into Equation 2-7. The 30 percent-LL line provides a limit and identifies the intermediate plasticity zone (MP), which is located between the 50 percent-LL and 30 percent-LL lines. Figure 2-8b shows the 30 percent-LL linear lines, which characterize the interfaces between the intermediate- and low-plasticity zones. Equation 2-9 gives the 30 percent-LL line equation corresponding to sediment predominated by Kaolinite-illite clay minerals. The equations that delineate the 30 percent-LL linear lines for the Illite-montmorillonite and the Montmorillonite groups are given in Table 2-5.

$$SF = Fines(\%) - 24.798 \Rightarrow (A \leq 0.5) \qquad \text{(2-9)}$$

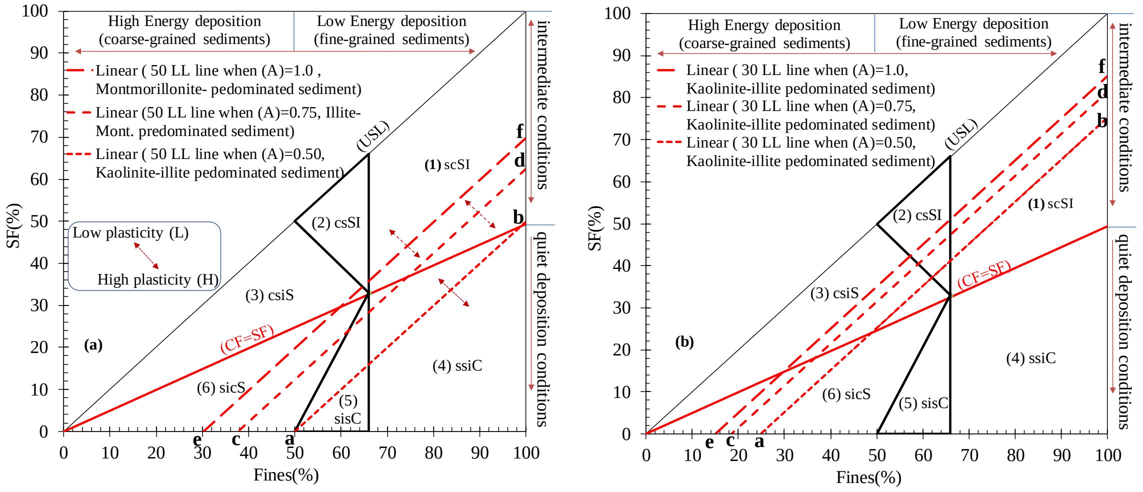

Figure 2-8 The combined grain size scheme, where (a) the 50 percent-LL zones of plasticity levels, and (b) the 30 percent-LL zones of plasticity levels.

2.7 VALIDATION WITH CLAY MINERALOGY

Validation of the proposed classification scheme to discern plasticity and subsequently infer mineralogy was done by evaluating the mineralogy and plasticity of some of the study soils. For mineralogy data, X-ray diffraction (XRD) tests were performed for six samples to identify clay minerals and determine their percentages. The tested samples were the four source soils and three mixed samples. Table 2-6 shows the results of the clay mineral analysis, including plasticity values. The XRD results show that the samples were composed mostly of kaolinite, mica group minerals (illite and vermiculite). None of the samples contained appreciable amounts of montmorillonite. The activity (A) of the samples was determined from Equation 2-5 and as seen in the table, the activity was around or mostly less than 0.5 for the samples.

Table 2-6 XRD results analysis and plasticity parameters of the source soils and other selected samples.

Sample No (S#)	K (%)	Mica Group (%)	M (%)	Qz (%)	F (%)	LL (%)	PI (%)
Henderson County (H)	38.4	53.9	0.0	3.7	2.0	25	8.5
Fayette County (F)	17.1	80.4	0.0	2.4	0.0	74.5	31
Lee County (L)	46.2	50.3	0.0	3.5	0.0	60.5	25
Kaolin (K)	85	9.6	0.0	5	0.0	48	13
#1	53.3	46.6	0.0	0.3	0.0	43	11
#30	40.6	56.8	0.0	0.2	2.4	55	28
#3	9.4	90	0.0	1.1	0.0	37.75	8

K = kaolinite; mica group = illite + vermiculite; M = montmorillonite; Qz = quartz; F = feldspar.

The tested samples mostly represented sediment predominated by kaolinite-illite, because A = 0.5; therefore, the 50 percent-LL line equation (Table 2-5) corresponding to this type of sediments is:

$$SF = 1.0879 Fines(\%) - 59.472 \Rightarrow \left(A = 0.5 \right) \tag{2-10}$$

Figure 2-9 shows the distribution of the tested data on the unified scheme. The figure shows the 50 percent-LL line and the 30 percent-LL-line was estimated at $A = 0.5$. These lines divided the scheme into three zones: low plasticity (LP) having LL <30 percent, intermediate plasticity (MP) having LL ≥30 and <50, and high plasticity (HP) having LL ≥50 percent.

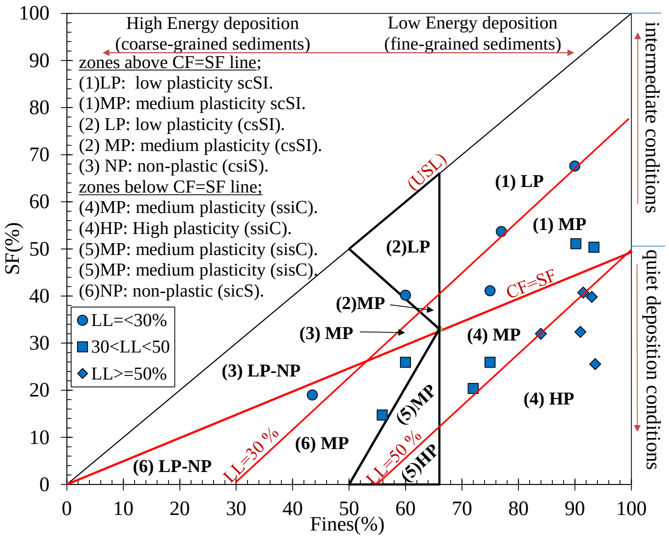

Figure 2-9 The scheme correlates grain size and plasticity parameters of tested samples, and represents sediment units having an activity of clays equal to or less than 0.5.

2.8 FINAL UNIFIED SF-FINES SCHEME

Figure 2-9 shows that the measured data were well matched and distributed through the three estimated plasticity zones. Most clay-predominant classes were classified as having high plasticity ($\geq$ 50 percent of LL), such as sandy silty Clay (ssiC). The unified FS-Fines scheme in Figure 2-9 shows that sediment units are classified into six units and each of those units is divided into various levels of plasticity. The plasticity level gradually decreases toward the upper and left sediment classes until LL $\leq$ 30 percent, as is the case for most silty clayey Sandy (sicS) and sandy clayey Silty (scSI) units. The LP and nonplastic (NP) zones correspond to fine sand and most predominant-silt class at which CF/SF is about 0.3 (toward the USL). Inorganic sediment properties and their behavior are significantly influenced by both the liquid limit and the clay fraction (Polidori 2009). In general, the lower the plasticity, the lower the CF/SF ratio (e.g., silt rich sediments). Polidori (2009) referred to a clay fraction of 25 percent as the interface between nonplastic and low-plastic fine-grained sediment, in which the sediment behaves as granular and semi-granular material. The csSI and scSI sediment classes behave similarly to the granular sediment (predominantly sand sediment) when CF/SF <0.3. This ratio corresponds with results reported by (Polidori 2009). Thus, fine-grained sediment with CF/SF $\leq$ 0.25 behaves as nonplastic sediment (similar to granular sediment), and sediment located below this line has very low plasticity.

2.9 FINAL UNIFIED SF-FINES SCHEME

Figure 2-10 is the final version of the SF-Fines scheme combining the grain size distribution and plasticity parameters to reflect most types of sediment units based on their predominant clay mineralogy. Based on the three ranges of *A* values differentiating three minerals groups (Table 2-5), several LL lines are developed using Equation 2-7. The three ranges of *A* values that define the three schemes ($A \leq 0.5$, $0.5 < A \leq 1.0$, and $A > 1.0$), are shown in Fig 2-13a, b, and c, and correspond to Kaolinite-, Illite-, and Montmorillonite-predominated sediment, respectively.

Figure 2-10 allows the six main sediment classes to be subdivided into different subclasses. For an example, two sediment units have the same grain-size distribution [e.g. $Fines(\%) = 80$ percent, SF = 50 percent]. According to the proposed scheme, this sediment unit is classified as sandy clayey Silt (scSI), but might have different compositions [defined by different activity of clay (*A*)], as presented in Figures 2-10. If $A = 0.5$, the predominant clay minerology is Kaolinite-Illite. The sediment unit scSI can be further divided into two zones of medium- and low-plasticity sandy clayey Silt (noted as 1b and 1c, respectively).

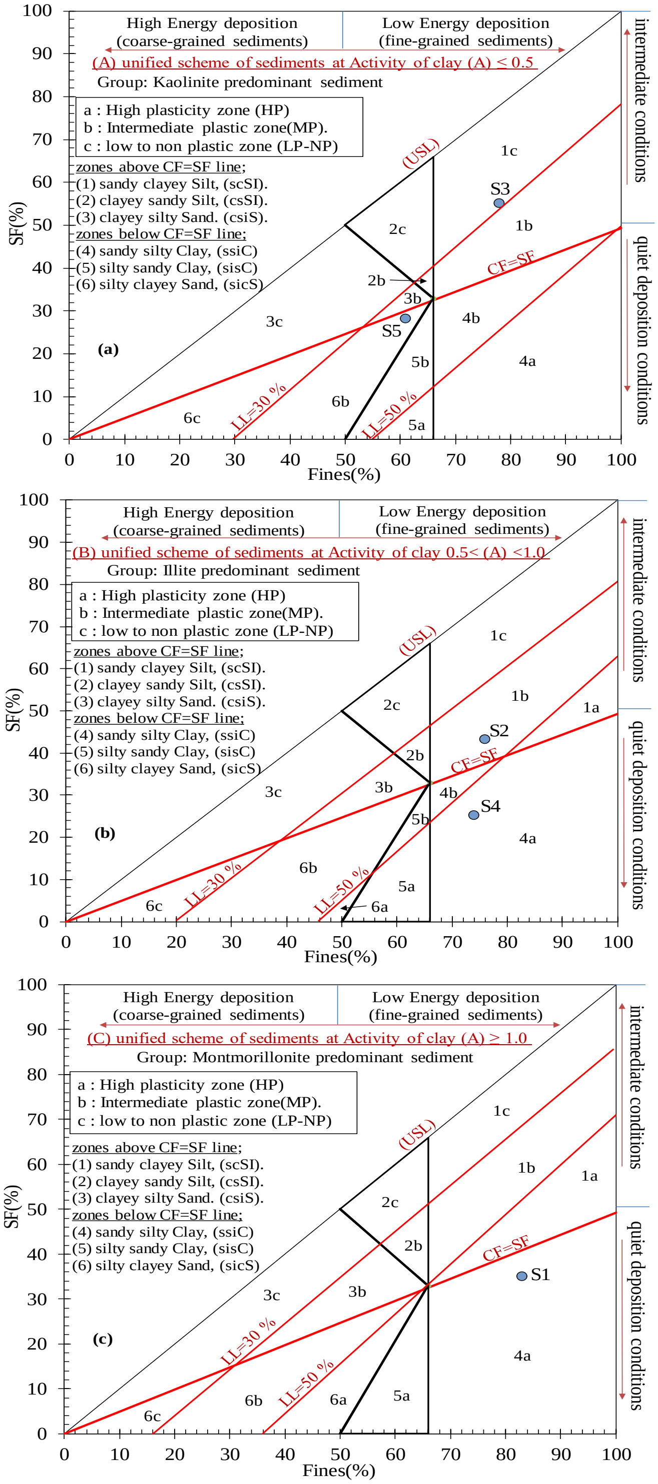

Figure 2-10 The final version of the SF-Fines scheme, presenting most types of sedimentary units based on their predominant clay mineralogy. (a) shows the kaolinite-illite sediment, in which the activity of clay (A) ≤0.5. (b) shows the illite-montmorillonite sediment, in which the activity of clay (A) ≥1.0.

2.10 VERIFICATION OF FS-FINES SCHEME

Verification of the proposed SF-Fines scheme was done by comparing the performance of the scheme with the classification system developed by (Blott and Pye 2012). Hypothetical sediment data were applied for this comparison. Table 2-7 gives the information for the five verifications sediments along with the results of the classification. For the current scheme, the data was plotted in Figure 2-10. The data was also plotted on the (Blott and Pye 2012) trigon, shown in Figure 2-11. In Table 2-7, it is worth noting that the symbols k, i, and m are used to indicate the smallest components of kaolinite, illite, and montmorillonite minerals, respectively. While, the uppercase characters of those symbols (K, I, and M) indicate the largest components.

Table 2-7 The proposed comprehensive scheme for sediment units that are characterized by grain size and plasticity parameters.

<table>
<tr><td colspan="10">(a) Classification of the fifth sediment samples showing in Figure 13.</td></tr>
<tr><th>S.#</th><th>Sand (%)</th><th>Silt (%)</th><th>Clay (%)</th><th>Fines (%)</th><th>sediment class</th><th><i>A</i></th><th>plasticity</th><th>Dominant minerals</th><th>Description of Sediment type</th></tr>
<tr><td>S1</td><td>17</td><td>35</td><td>48</td><td>83</td><td>4: sandy silty Clay (ssiC)</td><td>2.0</td><td>a: HP</td><td>kiM</td><td>4a: HP ssiC with kiM</td></tr>
<tr><td>S2</td><td>25</td><td>43</td><td>33</td><td>76</td><td>1: sandy clayey Silt (scSI)</td><td>0.75</td><td>b: MP</td><td>mkI</td><td>1b: MP scSI with mkI</td></tr>
<tr><td>S3</td><td>22</td><td>55</td><td>23</td><td>78</td><td>1: sandy clayey Silt (scSI)</td><td>0.45</td><td>c: LP-NP</td><td>iK</td><td>1c:LP-NP scSI with iK</td></tr>
<tr><td>S4</td><td>26</td><td>25</td><td>49</td><td>74</td><td>4: sandy silty Clay (ssiC)</td><td>0.6</td><td>a: HP</td><td>mkI</td><td>4a: HP ssiC with mkI</td></tr>
<tr><td>S5</td><td>39</td><td>28</td><td>33</td><td>61</td><td>6: silty clayey Sand (sicS)</td><td>0.35</td><td>b: MP</td><td>iK</td><td>6b: MP sicS with iK</td></tr>
<tr><td colspan="10">(a) Classification of the fourth sediment samples according to (Blott and Pye 2012) trigon.</td></tr>
<tr><td>S1</td><td>17</td><td>35</td><td>48</td><td>83</td><td>4: sandy silty Clay (ssiC)</td><td>N/P</td><td>N/P</td><td>N/P</td><td>4: ssiC</td></tr>
<tr><td>S2</td><td>25</td><td>43</td><td>33</td><td>76</td><td>1: sandy clayey Silt (scSI)</td><td>N/P</td><td>N/P</td><td>N/P</td><td>1: scSI</td></tr>
<tr><td>S3</td><td>22</td><td>55</td><td>23</td><td>78</td><td>1: sandy clayey Silt (scSI)</td><td>N/P</td><td>N/P</td><td>N/P</td><td>1: scSI</td></tr>
<tr><td>S4</td><td>26</td><td>25</td><td>49</td><td>74</td><td>4: sandy silty Clay (ssiC)</td><td>N/P</td><td>N/P</td><td>N/P</td><td>4: ssiC</td></tr>
<tr><td>S5</td><td>39</td><td>28</td><td>33</td><td>61</td><td>6: silty clayey Sand (sicS)</td><td>N/P</td><td>N/P</td><td>N/P</td><td>6: sicS</td></tr>
</table>

Capital letters K, I, and M are main component of a mineral group referring to Kaolinite, Illite, and Montmorillonite. The small letters k, i, and m are the minor (descriptive) components of the same three mineral groups.

The comparison data presented in Table 2-7 shows that although both classification schemes give the sediment class, the FS-Fines scheme further describes the plasticity, activity, and mineralogy of the samples. For example, the S1 sample, is located in sandy silty Clay (ssiC) sediment class, which is noted as number 4 in Figure 2-10. The activity is given as 2.0, which indicates Montmorillonite is the predominant clay mineral of the sediment, with a minor component of Kaolinite (noted as kiM). From Figure 2-10c, the sediment is in the region of high plasticity level (HP). The other verification sediments samples were compared in the same manner and are summarized in Table 2-7

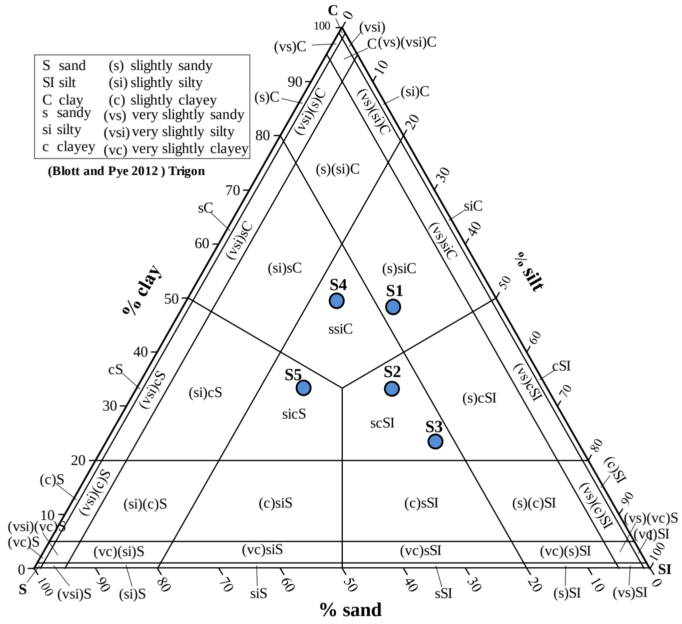

Figure 2-11 Classification of the same fifth samples according to (Blott and Pye 2012) trigon.

The comparison between the two criteria demonstrates the significance of the FS-Fines scheme for promoting description of the sediment classes and for its capability to account for mineralogy that other classification sediment systems unable to accomplish. Indication of the predominant minerals groups is of essential importance to evaluate the response of the sediments to the deposition processes, and potentially imparts a better inference of the physical properties of sediments. This can be exploited to predict sediment mechanical behavior of variety of sediments in different depositional environment, such as marine, estuarine, and riverine sediments.

2.11 GEOLOGICAL ENGINEERING APPLICATION OF THE SF-FINES CLASSIFICATION SCHEME

Several researchers (Chung and Finno 1992, Bartetzko and Kopf 2007, Oh et al., 2017) have shown that sediment mechanical behavior can be estimated from correlations between the consistency limits and undrained shear strength, friction angle, or compression indices. Data and discussions presented by Mitchell and Soga (2005) allow for general associations of mechanical behavior of sediments and plasticity to be made. Specifically, high plasticity is associated with high compressibility (HC) and low shear strength (LS), moderate or intermediate plasticity is associated with intermediate compressibility (IC) and intermediate strength (IS), and low plasticity is associated with low compressibility (LC) and high strength (HS). Table 2-8 demonstrates the further characterization that is produced and covers a variety of sediment units

Table 2-8 The proposed comprehensive scheme for sediment units that are characterized by grain size and plasticity parameters.

Dominant Depositional Conditions	Sediment Type	CF/SF	Symbol	Activity of Clay (*A*):	Subclasses of Sediment Unit	Potential Mechanical behavior of the sediment classes		
						HC/LS	IC/IS	LC/MS
Quiet (low) depositional processes, i.e., marshes, bay mud, tidal flat	Fine-grained (silt > sand or clay > sand)	R >1.0	(4) ssi**C**,	A ≤ 0.5	(4a) HP ssi**C** (4b) MP ssi**C**	4a	4b	-
				0.5<A<1.0	(4a) HP ssi**C** (4b) MP ssi**C**	4a	4b	-
				A ≥ 1.0	(4a) HP ssi**C**	4a	-	-
			(5) sis**C**	A ≤ 0.5	(5a) HP sis**C** (5b) MP sis**C**	5a	5b	-
				0.5<A<1.0	(5a) HP sis**C** (5b) MP sis**C**	5a	5b	-
				A ≥ 1.0	(5a) HP sis**C**	5a	-	-

Table 2.8 (continued)

Intermediate processes (mixed estuarine fluvial zone, i.e., floodplain, channel levee	Fine-grained sediments (silt > sand or clay > sand)	$R < 1.0$	(1) sc**SI**	$A \leq 0.5$	(1b) MP sc**SI** (1c) LP-NP sc**SI**	-	1b	1c
				$0.5<A<1.0$	(1a) HP sc**SI** (1b) MP sc**SI** (1c) LP-NP sc**SI**	1a	1b	1c
				$A \geq 1.0$	(1a) HP sc**SI** (1b) MP sc**SI** (1c) LP-NP sc**SI**	1a	1b	1c
			(2) cs**SI**	$A \leq 0.5$	(2b) MP cs**SI** (2c) LP-NP cs**SI**	-	2b	2c
				$0.5<A<1.0$	(2b) MP cs**SI** (2c) LP-NP cs**SI**	-	2b	2c
				$A \geq 1.0$	(2b) MP cs**SI** (2c) LP-NP cs**SI**	-	2b	2c

Table 2.8 (continued)

High depositional processes, fluvial processes, e.g., channel levee, sandy coastal deposits	Coarse-grained sediments (silt < sand > clay)	R <1.0	(3) csi**S**	A ≤ 0.5	(3b) MP csi**S** (3c) NP csi**S**	-	3b	3c
				0.5<A<1.0	(3b) MP csi**S** (3c) NP csi**S**	-	3b	3c
				A ≥ 1.0	(3b) MP csi**S** (3c) LP-NP csi**S**	-	3b	3c
		R > 1.0	(6) sic**S**	A ≤ 0.5	(6b) MP sic**S** (6c) NP sic**S**	-	6b	6c
				0.5<A<1.0	(6a) HP sic**S** (6b) MP sic**S** (6c) NP sic**S**	-	6b	6c
				A ≥ 1.0	(6a) HP sic**S** (6b) MP sic**S** (6c) NP sic**S**	6a	6b	6c

HC=High compressibility; IC= Intermediate Compressibility; LC=Low Compressibility; LS=Low Strength; IS=intermediate Strength; MS= Moderate strength; HS= High strength.

Applying these general associations to the proposed SF-Fines classification scheme extends the utility of the scheme beyond simply classifying the sediment class, but to infer the potential mechanical behavior of sediments having various GSD proportions mineralogies. Table 2-8 shows in detail the interpretation of the SF-Fines scheme (Figure 2-10) and characteristics of classified sediment units.

2.12 INFERENCES TO MECHANICAL BEHAVIOR

The full comprehensive version of the SF-Fines scheme as presented in Table 2-8 allows the predominant depositional conditions, as well as the compressive and shear behavior of the sedimentary layers to be readily inferred. For an instance, the potential mechanical behavior of samples, S1, S2, and S3 can be describe as follows (noted in shaded cells in Table 2-8):

- S1: 4a: High plasticity sandy silty Clay, with high compressibility to low shear strength (HC/LS). It reflects a quiet depositional conditions.
- S2: 1b: Intermediate plasticity sandy clayey Silt, intermediate compressibility to intermediate shear strength. It reflects an intermediate depositional conditions.
- S3: 1c: Low to no plasticity sandy clayey Silt, with low compressibility to moderate strength. It reflects an intermediate depositional conditions.

2.13 HIGHER RESOLUTION WITH FINE-GRAINED SEDIMENTS

The clay-silt interface in SF-Fines scheme offers higher resolution than can be achieved by the common Casagrande chart (plasticity chart), which lacks the resolution to discriminate clays from silts (Jang and Santamarina 2015, Polidori 2015, Moreno-Maroto and Alonso-Azcárate 2018). The discrepancies in conventional plasticity chart can occur when fine-grained sediments have high amounts of silt-sized particles (e.g. CF/SF <<1.0) with low plasticity. For example, the sample S3, which has LL = 30 percent and PI = 10.4 percent, is classified as "clay with low plasticity" according to the conventional plasticity chart. However, the sample S3 has 55 percent of silt-sized particles, which is much higher than clay-sized particles (23 percent). Figure 2-10 shows the sample is classified as sandy clayey Silt (scSI), as opposed to being classified as a clay in the conventional plasticity chart (CL according to the Unified Soil Classification System). This difference is because the conventional plasticity chart discriminates clays from silts based solely on the plasticity indices (i.e. LL and PI) of the sediment and does not consider particle size proportions. Conversely, the clay-silt interface of the proposed SF-Fines scheme properly separates the clays and silts classes due to the direct correspondence to silt and clay proportions.

2.14 SUMMARY POINTS OF IMPORTANCE USING SF-FINES SCHEME

Figure 2-12 shows a flowchart that explains the general steps and components used to develop SF-Fines scheme proposed in this study. The flowchart illustrates the three GSD sediment factors that created the main SF-Fines scheme using the linear relationship (Equation 2-1) so that the six sediment class are identified. Then, the composition (mineralogy) sediment factors (LL and PI) integrated into the scheme using (Equation 2-7), so that the high and low liquid limit lines are determined, which entails the six classes are elaborated in different subclasses (Figure 2-10).

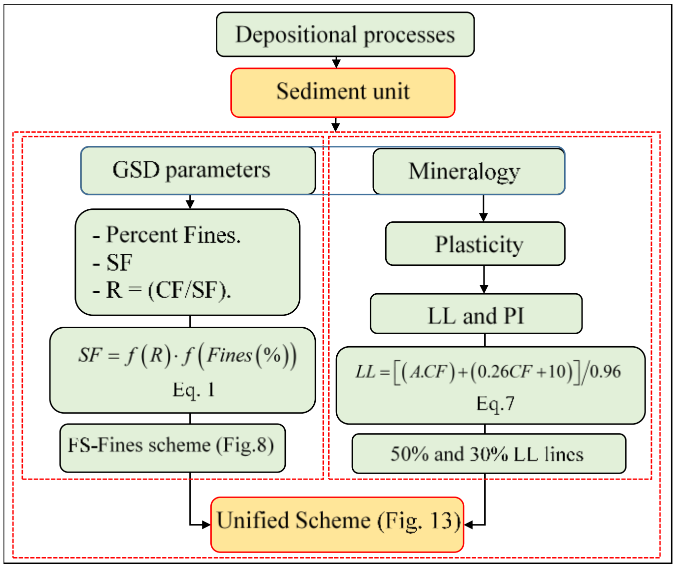

Figure 2-12 Flowchart concisely describing the process of characterizing sediment unit.

2.15 CONCLUSIONS

This study proposed a new classification scheme to describe unconsolidated inorganic sediment that covers a wide range of estuarine-riverine regions. The goal was to construct a plausible and practical scheme that identifies not only sediment texture but also its dominant mineralogy. This classification scheme is based on the linear relationship between percent silt (SF) and Fines, which was well identified. The behavior of this correlation was controlled by clay to silt ratio (CF/SF). To test this correlation, a mixing procedure was performed and produced synthetic samples, in which percent Fines, SF, and CF/SF ratios were controlled. Regarding the plasticity parameters (LL and PI), the study proposed using liquid limit and plasticity index as a proxy for the sediment mineralogy. To accomplish this, the activity of clay is used as the measurable factor related to each major clay-mineral group. The plasticity that was mathematically estimated had two interfaces and three zones of low, intermediate, and high plasticity in the classification scheme.

Because of combining plasticity and grain size characteristics, the scheme allows the sediment units to be divided into more subdivisions and provides subclasses sediment units, specifically in fine-grained sediment units. These sub-sediment units provide more resolution to distinguish the boundaries of the sedimentation units in estuarine-riverine regions. The SF-Fines scheme is of essential significance to allow further detailed characterization of sediment units and then provides better resolution in classes boundaries. The clay-silt discrimination in SF-Fines scheme is more plausible than that in common Casagrande plasticity chart.

CHAPTER 3.

Determining the Effects of Depositional Processes on Consolidation Behavior of Sediment Using Shear-Wave Velocity

3.1 INTRODUCTION

The complexity of depositional and post-depositional processes, which results in a variety of depositional environments, makes constructing a plausible model for the consolidation process of sediments difficult. The mutual influence between the temporal and spatial variation of depositional environments with their resultant physical and mechanical properties cause several compression issues, such as consolidation settlement and land subsidence, which mostly occur in estuarine-riverine regions throughout the world (Chai et al., 2004, Zhang et al., 2008, Sarti et al., 2012).

Several studies (Brain et al., 2011, Dipova 2011, Liu et al., 2013, Liu et al., 2013) have addressed the relationship between the change in compression properties and variability of sedimentary materials. Most of these studies used observational data to estimate consolidation parameters and model compressive behavior of different sedimentary units. However, the framework of these studies tend to be site-specific and only describe the site consolidation behavior in broad terms.

The consolidation process is traditionally evaluated on the basis of laboratory testing. For this evaluation, undisturbed field samples are collected at discrete locations and depths and taken back to the laboratory for testing. The testing results from these discrete locations and depths are assumed to represent the consolidation behavior for entire regions of the site, or for the entire site itself. For complex depositional environments, this approach can lead to a grossly inaccurate picture of the compressional behavior for the site in question. Field geophysical testing methods provide a means to obtain areal and volumetric data that can better reflect the depositional variation of sediments. In addition, geophysical methods provide data for areas that may not be accessible to sample extraction equipment. In particular, geophysical methods that provide measurements of shear wave velocity appear to be well suited for investigating the physical characteristics of sediments (Klein and Santamarina 2005, Chang et al., 2011).

Shear wave propagation through a sediment is highly dependent on material density, which can be described by the void ratio, e, and effective stress (Santamarina et al., 2001). The compression process is characterized by the change in the void ratio as a function of the change in mean effective stress, p', which is defined as $p' = \left(\sigma_1' + \sigma_2' + \sigma_3'\right)/3$ (where σ_1', σ_2', and σ_3' are the major, intermediate, and minor principal stresses, respectively. Thus, it is highly certain that shear wave velocity can be used to estimate the consolidation behavior of soft clay and sediments (Lee and Santamarina 2005, Chang et al., 2011)

Several studies (Santamarina and Cascante 1996, Fam and Santamarina 1997, Leong et al., 2009, Irfan et al., 2017, Oh et al., 2017) have used shear-wave velocity, V_s, to characterize the compression process of deposition. In particular, some researchers (Cha et al., 2014, Oh et al., 2017) have used V_s to develop predictive equations to estimate the consolidation behavior of soft marine clay. For example, the Oh et al., (2017) prediction model appeared to match their experimental consolidation data, but the model required a priori knowledge of compression indices such as the virgin compression index, C_c, and the recompression index, C_r. These compression indices are estimated from an $e - \log\left(p'\right)$ curve obtained from experimental tests. Thus, the results will reflect behavior only at discrete locations and depths. Also, the aforementioned prediction models typically define consolidation behavior using a non-continuous bi-linear model to describe the recompression and virgin compression portions of the consolidation curve separately. While there are a few examples of continuous functions used to define the $e - \log\left(p'\right)$ curve (Liu et al., 2013, Horpibulsuk et al., 2016) these approaches do not explicit include shear wave velocity in the formulation and still require a priori knowledge of compression indices.

This paper presents a continuous function that explicitly uses shear wave velocity V_s to predict the entire consolidation process of sediment ($e - \log p'$), without prior knowledge of compression indices. This approach also defines factors that describe the depositional environment, such as grain size and plasticity limits. These factors are shown to influence and control the $e - \log p'$ relationship. Thus, the resulting function is shown to be applicable for a variety of sedimentary materials.

3.2 THEORETICAL DEVELOPMENT

Herein, “compression process” and “consolidation process” are synonymous and refers to the change in void ratio, e with a change in mean effective stress, p'. This correlation is called a consolidation behavior, in which p' implies the isotopic application of stresses. Under saturation conditions, consolidation describes time-dependent volumetric deformation (i.e. reduction of volume) under a constant load increment (Terzaghi et al., 1996).

3.2.1 Expression for the Consolidation Process

Figure 1 is a typical consolidation curve [e-log (p')] taken from preliminary data associated with this study. From the initial investigation, it was observed that the best model fitting the preliminary data was an exponential decline model. Reaves (1955) used the negative exponential trend to describe the compression change as a function of the increased pressure. Equation 3-1 is a mathematical expression of the exponential relationship according to Reaves (1955):

$$y\left(x\right)=a\cdot\exp\left(-b\cdot x\right) \tag{3-1}$$

where x is the applied pressure and y is the amount of compression change, and a and b are fitting factors.

For describing the consolidation process, compression change is replaced with volumetric change where, the void ratio, e, exponentially experiences a reduction at a rate proportional to the increase in mean effective stress. Equation 3-2 is the expression of an exponential model in terms of e-log (p') space (Figure 1):

$$e=A_1\cdot\exp\left(-A_2\cdot x\right) \tag{3-2}$$

where A_1 and A_2 represent intercept and initial decline rate of the equation, respectively. The A_1 factor (the intercept) has an explicit physical meaning that indicates the initial void ratio of sediment, e_0, at the beginning of consolidation processes (Figure 3-1), and the A_2 factor is a rate-of-void ratio change with respect to the mean effective stress. The A_2 term reflects the volumetric compressibility of the material over the range of stresses. For this study, the rate-of-void ratio change with respect to change in mean effective stress is referred to as the coefficient of compressibility and is expressed as C_f. Substituting e_0 and C_f for A_1 and A_2, respectively and including the mean effective stress term yields Equation 3-3:

$$e = e_0 \cdot \exp\left(-C_f \cdot p'\right) \tag{3-3}$$

It is noted that the C_f term is similar to the coefficient of volumetric compressibility, m_v associated with Oedometer testing and is given by $m_v = -\partial\varepsilon_v / \partial\sigma'$ [where ε_v = volumetric strain = $\Delta e / \left(1+e\right)$]. However, the m_v term is an incremental value obtained from one dimensional consolidation, whereas the C_f term captures the compressibility of the sample over the entire range of stresses.

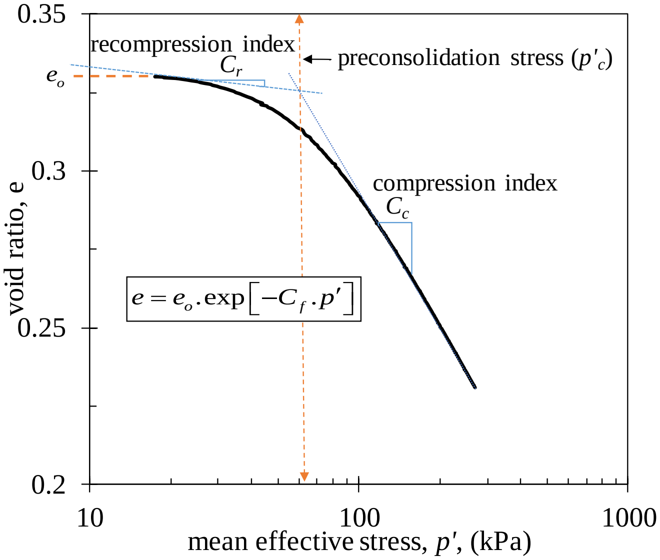

Figure 3-1 A typical *e*-log (*p*′) relation.

From the mathematical expression of Equation 3-3, it can be deduced that as the C_f term increases, the range of void ratio values (i.e. maxima to minima) increase over a given range of stress.

3.3 ELASTIC SHEAR-WAVE VELOCITY RESPONSE

The propagation of shear wave velocity through a geologic material reflects the stiffness of the material. Stiffness describes the microscale contact forces of the grains, which is a response at small strain levels (i.e. an elastic behavior). These contact forces varying as functions of the current stress state of the material. However, at various stress states, the measurements of shear wave velocities of a material changing from one stress state to another state corresponds to changes in the structure (fabric) of the material (Santamarina and Aloufi 1999). The implication is that shear wave velocity-mean effective stress relationships involving different stress states, captures both strain level; the contact grain response (i.e. the elastic strain level) and the permanent changes in the fabric during different stress states (i.e. the plastic strain level). For a particulate material (e.g. sediments), increasing the mean effective stress of results in an increase in the packing of particles. The denser particle packing causes an increase in wave velocity of materials. The power function is an expression that best determines the association between shear-wave velocity and mean effective stress, and captures both elastic and plastic strain levels (Santamarina and Aloufi 1999, Santamarina et al., 2001), as shown in Equation 3-4.

$$V_s = \alpha_s \left(\frac{p'}{p'_o} \right)^{\beta_s} \tag{3-4}$$

where α_s (m/s) is the experimental factor that represents shear-wave velocity at mean effective stress, p'_o = 1.0 kPa. The β_s exponent is the experimental factor that is a function of sediment type. Initial observations indicate that Equation 4 well represents isotropic loading conditions.

Solving Equation 3-4 in terms of mean effective stress and substituting into Equation 3-3 results in the general form that expresses the void ratio as a function of shear-wave velocity. Equation 3-5 shows this general expression:

$$e = e_o \cdot \exp\left[-C_f \cdot \left(\frac{V_s}{\alpha_s} \right)^{\frac{1}{\beta_s}} \right] \tag{3-5}$$

3.4 MEANS AND METHODS

Shear-wave velocity tests were performed during isotropic consolidation triaxial tests to investigate the factors influencing the parameters presented in Equation 3-5 (i.e. e_o, C_f, α_s, and β_s). Samples used for testing were prepared in the laboratory and designed to mimic common sediment types.

For this study, source soils were mixed in varying proportions to create different sediment with range of behaviors. The source soils were selected from Fayette, Lee, and Henderson Counties, Kentucky. Table 3-1 shows the properties of the three source soils used in this study. A synthetic kaolin soil was also used, and its properties are included in Table 3-1.

Particle size analysis was perform for the source soils according to (ASTM D422 2007) and classified using the Unified Soil Classification System (USCS) (ASTM D2487 2006). Atterberg limits testing was perform according to (ASTM D4318 1994). The soils were classified as lean clay (CL) for the kaolin and the Henderson County soils, and fat clay (CH) and elastic silt (MH) for the Fayette and Lee County soils, respectively. Grain-size distribution, plasticity index (PI), liquid limit (LL), and specific gravity (G_s) were obtained for the source samples and mixtures.

Table 3-1 Index properties for source soils used to mix and simulate sediment units.

Parameter	Kaolin	Henderson County	Fayette County	Lee County
Specific Gravity, G_s	2.63	2.69	2.86	2.7
Liquid Limit, LL (%)	48	28.2	64.3	55
Plasticity Index, PI (%)	13	8.5	30	23
Percent Fines (%)	100	99.4	86.8	82
Clay Fraction, CF (%)	45	20	74	45
USCS	CL	CL	CH	MH

Percent fines = % passing #200 sieve; clay fraction = % <0.002 mm.

3.5 CREATION OF SEDIMENT SAMPLES

The mixture procedure used for this study mixed various percentages from the individual source soils to generate new sediment samples that had different percent fines, percent silt, and percent clay. The new sediment samples represented a wide range of fine-grained sediments ranging from predominately silt samples to predominantly clay samples. This mixture procedure, described in detail in (Muttashar et al., 2018), facilitated accurate percentages of the entire grain-size distribution (GSD) curve. In short, the GSD curves of the source soils were divided in several different percentages. The percentages were combined to produce new GSD curves that had specific Fines percent and CF/SF ratios.

Figure 3-2 shows the GSD curves for the samples used in this study. In addition to GSD testing, consistency limits were measured as well. Table 3-2 presents the index properties of the sediment samples. The table includes the resultant percent fines, silt fraction, and clay-to-silt ratio (CF/SF). The CF/SF ranged from 0.2 to 2.45, covering fine-grained sediment types from predominant silt to predominant clay sediments, respectively.

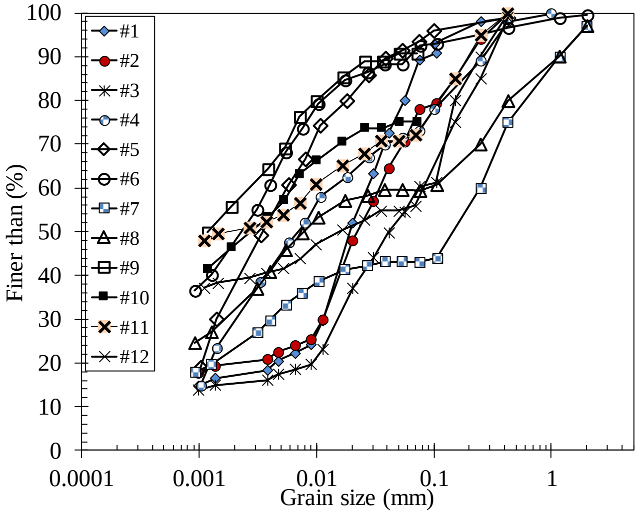

Figure 3-2. Grain-size distribution curves of the tested samples.

Table 3-2 shows four discrete groups of samples based on percent fines: 90–93 percent (four samples), 72–77 percent (four samples), 60 percent (three samples), and 43 percent (one sample). This categorization allows the presence of samples that have the same CF/SF, but different percent fines, and vice versa. For example, the samples have three different percent fines (91, 60, and 43 percent), yet the CF/SF ratios of those samples are approximately the same (1.0). This process of controlled percentages of the samples facilitated correlation of fines, silt, and clay percentages for the α_s, β_s, e_0, and C_f parameters. Previous studies (Kim et al., 2013, Cha et al., 2014, Li and Zeng 2014) have investigated the α_s and β_s parameters based on two general categories (coarse-grained and fine-grained sediments), but did not consider the particle-size percentages of fine-grained sediments. Considerations for the effects of the percentages of fines, silt, and clay is crucial for determining α_s and β_s factors specific to differing depositional environments.

Table 3-2. Index test data for the sediment samples used in this study.

Sample#	Fines (%)	Clay (%)	Silt (%)	CF/SF	LL (%)	PI (%)
1	90.0	17.0	73.0	0.23	25.0	6.0
2	77.0	19.0	58.0	0.32	23.7	4.8
3	60.0	16.6	43.4	0.38	20.0	4.0
4	75.0	29	44.4	0.65	30.0	9.0
5	93.4	39	54.4	0.71	43	11.0
6	91.5	47.5	44.0	1.00	60.5	25.0
7	43.5	23	20.5	1.10	38.0	12.0
8	60.0	32.0	28.0	1.14	41.0	15.1
9	91.0	56	35.0	1.60	53.4	10.2
10	75.0	47.0	28.0	1.67	44.6	8.0
11	72.0	50.0	22.0	2.27	49.0	14.5
12	55.9	40.0	15.9	2.50	35.0	10.0

Fines = % passing #200 sieve; clay = diameter less than 0.002 mm; silt = $0.002 \leq diameter \leq 0.075\ mm$; LL = liquid limit; PI=plasticity index.

3.5.1 Sample Preparation for Triaxial Testing

Shear wave velocity testing was performed on resedimented samples. To prepare a uniform sediment sample, first a slurry was made by mixing a dry sample with tap water. The amount of dry soil was based on the specific dry density of a sample that was 152.4 mm in height and 68.5 mm in diameter. The percentage of water used in the mixture was about two times the liquid limit of the soil. This was sufficient to make a stable slurry without the particles settling (Germaine and Germaine 2009). Next, the mixture was poured into the sample mold, and then a porous stone and filter paper were put inside the bottom of the cylinder. Afterwards, another porous stone and filter paper were placed on top of the mixture to close the cylinder (also called a mold cell). The next step was pre-compressing and creating the uniform sample (152.4 mm in height and 68.5 mm in diameter).

The traditional resedimentation technique applies static weights to the slurry to consolidate the sample (Germaine and Germaine 2009). Although this approach produces a uniform sample, the density of the sample is not controlled. For this study, the sample density was controlled by compressing the slurry to a targeted height, at a very low displacement rate. Displacement rates ranged between 0.025 to 0.019 mm/min, depending on samples being predominantly silt or predominantly clay, respectively. These rates were slow enough to allow excess porewater pressures to dissipate during the preparation process. Also during this process, the vertical load corresponding to the displacement was recorded. Low vertical load corresponded to low displacement rate and vice versa. The maximum vertical loads exerted on the samples during the pre-compression process ranged between 50 to 70 kPa. In this study, a low displacement rate, with a corresponding low vertical load, was assumed to simulate quiet (i.e. low energy) depositional conditions. Conversely, a high displacement rate can be used to simulate high energy depositional conditions.

Controlling the displacement rate is useful for simulating fine-grained sediments that develop convergent structures (grain size and mineralogy) with different rates of deposition. The rate of deposition reflects the loading conditions of settled sediments in situ. The deposition rate describe the differing amounts of time required to rearrange the particles of the sediment fabric, as well as the amount of time required for pore water pressure to dissipate and create the structure of a particular sediment unit. Thus, simulating a deposition rate provides a better understanding of the fine-grained sediments that are lithologically homogenous, but have different deposition loads. The displacement-controlled sedimentation method used in this study produced uniform samples with specific dimensions and physical properties to be acquired for the final step.

3.6 BENDER ELEMENT TESTS

Elastic shear-wave velocities of the samples were measured using piezoelectric elements called bender elements (BE) that were installed inside a standard triaxial cell. Figure 3-3 shows the steps involved in performing the BE testing. After the pre-compression sample preparation process, the initial physical properties such as dimensions, weight, and moisture content were measured and the sample was mounted in the triaxial cell and covered by a membrane. Top and pedestal caps hold the top and bottom BEs, respectively, and were inserted into the sample. As shown in Figure 3-3, the two cables connect the BEs to the signal processer that generates and processes the wave signal. The triaxial cell was then mounted in the load frame to start the triaxial test.

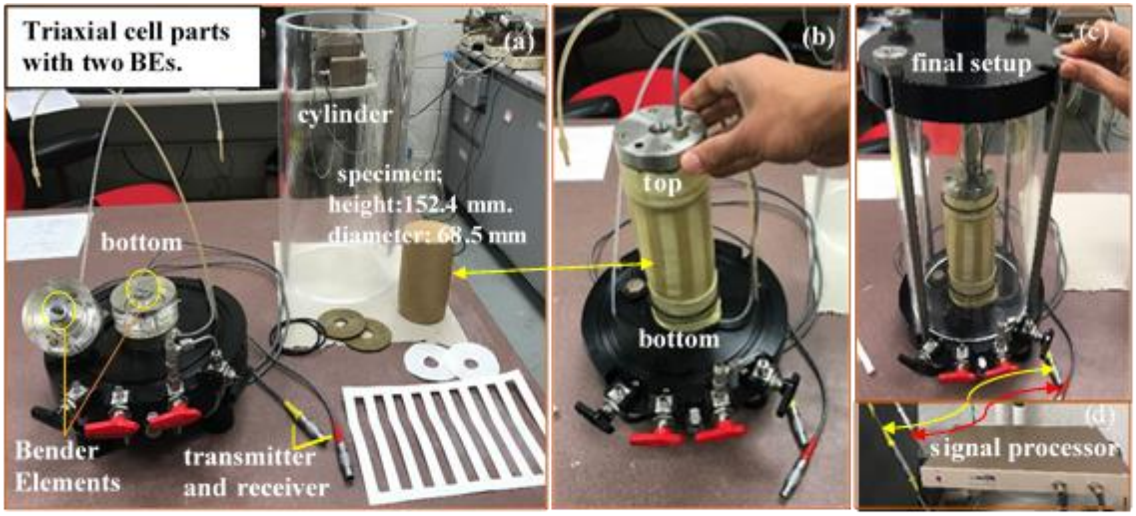

Figure 3-3. The materials and steps to set up bender elements in a triaxial cell. (a) The triaxial cell with two bender elements, a uniform specimen (152.4 mm x 68.5 mm), and pairs of pore stones and filter. (b) Assembling the materials and mounting the specimen in the triaxial cell. (c) Complete setup of the triaxial cell, which has two cables to connect the top and bottom BEs to the signal processor.

Table 3-3 lists the test conditions and methods that were applied during the testing. A single-pulse sinusoidal (i.e wave shape) input signal was used for the shear-wave propagation. The ratio 2L/H, a penetration length of BE at the sample ends (L) to the sample height (H), was 15.2 percent. This value (15.2) allowed the wavelength number to be high enough to reduce any near-field effect (NFE) that might influence the estimation of the shear-wave travel time and, as a result, the interpretation of the wave signal (Viggiani and Atkinson 1995, Kawaguchi et al., 2001). The NFE is expected to happen when the sample has a small height (H), such as occurs with a shear box or oedometer sample (H ~20 mm). NFE is also more likely with dry sample conditions (Yamashita et al., 2009). Fortunately, both of these conditions (small-height cell and dry conditions) were avoided in this research because high-height samples (152.4 mm) were used and testing was under saturation conditions.

Table 3-3. Test conditions for bender element testing.

Sample Size (mm)		BE Dimension (mm)		2L/H (%)	V (V)	ws	T (ms)	t (ms)	f_s (kHz)
H	D	Th	L						
152.4	68.6	1.8	11.6	15.2	10	Sin	0.1	2	100

Th = thickness; L = length of BE; H = height; D = diameter; V = exciting voltage; ws = wave shape; T = wave period; t = sampling time; f_s = sampling frequency.

The cross correlation method, as implemented in the automated Bender Elements Analysis Tool (BEAT) software, was used to detect the time interval of the shear wave. Cross-correlation is a measure of similarity of two time series as a function of the displacement of one relative to the other. In general, an automated tool is recommended for analyzing BE data (Lee and Santamarina 2005, Rees et al., 2013). Time differences between transmitted and received signals were detected at multiple intervals during loading for the consolidation phase.

3.6.1 Consolidation Results

The consolidation phase of the isotropically consolidated undrained triaxial (CIU) standard method (ASTM D4767 2004) was used to determine consolidation properties of the mixtures. Typical results were shown previously in Figure 3-1. In general, resultant consolidation curves reflect the capability of volumetric change of the samples in saturated conditions. The capacity of volumetric change was found to be related to the type of sediment and composition (Adu-Gyamfi et al., 2011, Bryson et al., 2017). This implies that the consolidation behavior [*e*-log (*p'*)] tends to be related to the grain-size percentages and plasticity limits, such as percent fines and liquid limit (Kwon et al., 2011, Jang and Santamarina 2015). Those parameters were prominent enough to characterize the consolidation behavior of the samples. Table 3-4 includes the resultant consolidation parameters estimated from the [*e*-log (*p'*)] curves. The C_f values were obtained by fitting an exponential trend line (i.e. Equation 3-3) through the [*e*-log (*p'*)] data. When compared to the data previously presented in Table 3-1, the data in Table 3-4 show that an increase in percent fines leads to an increase in the recompression index (C_r) and compression index (C_c). In order to understand the profound effect of fine particles, the mutual effect of the silt and clay percentages must be understood. Generally, lower the compression indices (C_r and C_c) tend to correspond to higher silt percentages, due to typical reduction in clay fraction (Adu-Gyamfi et al., 2011, Bryson et al., 2017).

Table 3-4. Consolidation parameters from isotropic consolidation testing.

Sample#	e_0	C_c	C_r	p'_c (kPa)	C_f (m^2/MN)	m_{vc} (m^2/MN)
1	0.41	0.08	0.009	42	1.25	0.185
2	0.47	0.07	0.005	120	0.18	0.037
3	0.7	0.05	0.006	40	1.00	0.144
4	0.33	0.15	0.014	68	1.50	0.234
5	0.74	0.24	0.021	48	1.30	0.220
6	0.94	0.28	0.031	61	1.20	0.270
7	0.32	0.08	0.009	47	1.25	0.164
8	0.56	0.11	0.013	80	0.50	0.099
9	0.76	0.22	0.019	145	0.40	0.077
10	0.67	0.16	0.012	59	1.20	0.228
11	0.54	0.21	0.017	40	1.90	0.235

Table 3-4 also includes values of the coefficients of volumetric compressibility, m_{vc} measured at the preconsolidation pressure, p'_c. As previously mentioned, C_f in Equation 3-5 is the rate-of-void ratio change over a range of mean effective stresses, whereas the coefficient of volumetric compressibility, m_v represents the change in volumetric strain, ε_v at increments of mean effective stress, p'. Thus, the m_v values change and increase through the progression of the consolidation process. The difficulty in comparing the two parameters is choosing a reference value of m_v that can be uniquely correlated with the C_f parameter. For this paper, the practical point used as a m_v-reference was the value at preconsolidation stress, p'_c. Figure 3-4 shows relation between the C_f parameter and the m_{vc} value at preconsolidation stress. In the figure, it is observed that the two parameters are well correlated at lower to medium values for both parameters, but diverge slightly for higher values. Given that m_{vc} tends to be positively correlated to plasticity, as evidenced by the corresponding compression indices shown in Table 4, this is equivalent to saying the two parameters are well correlated for lower to medium plasticity sediments, but diverge slightly for higher plasticity sediments. The data in the figure shows that the relationship between the C_f parameter and the m_{vc} value at preconsolidation stress can be best described by Equation 3-6 as:

$$C_f = 7.06 \cdot \left(m_{vc}\right)^{1.097} \tag{3-6}$$

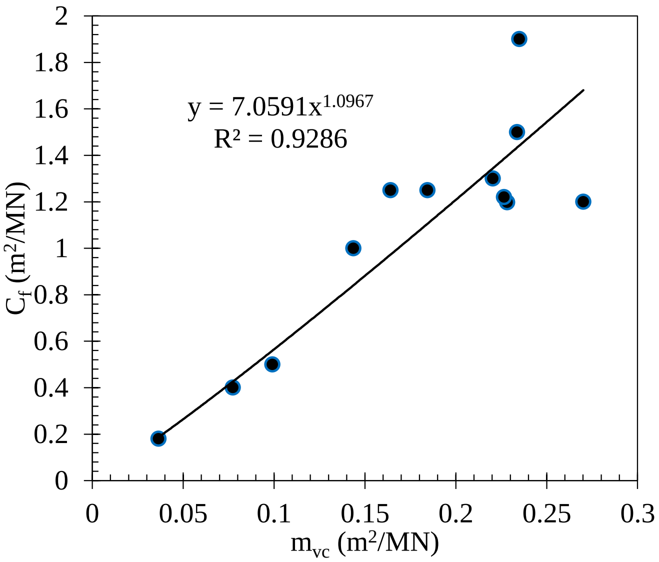

Figure 3-4. The relation between the C_f parameter and the m_{vc} value at preconsolidation stress.

3.7 BENDER ELEMENT RESULTS

Figure 3-5 shows a transmitted and received shear-wave signal at selected incremental mean effective stresses (p') during the loading steps of the consolidation process. Figure 5 also shows the calculated cross correlation signals (CC, indicated by the dashed signal line) and compares them with the received signal (indicated by the orange solid line). The time difference obtained by the CC method was identified using the BEAT software.

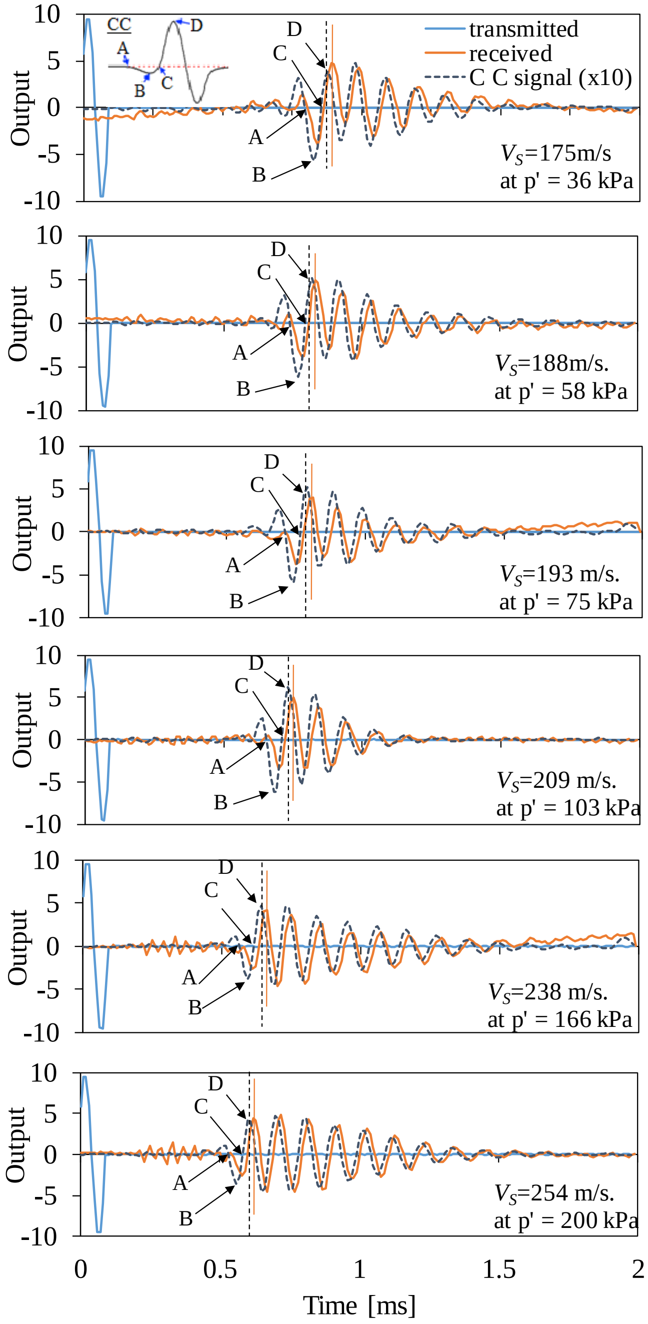

Figure 3-5 Signals of a shear wave during the first loading step of the consolidation test.

The actual range of the resultant signals (output) was between +1 and –1. With this small range, it was difficult to discern points of overlapped and thus difficult to compare the cross correlation signals with the received signal. Consequently, the output signals were multiplied by 10 to increase the resolution, as shown in the Figure 3-5. Four diagnostic points (A, B, C, and D) are shown in the figure. These points primarily define the received signal in the cross correlation process. The A point is the first deflection, B is the first bump maximum or first negative peak, C is the zero after a first negative bump, and D is the major (positive) first peak that is used to determine the travel time. There was a clear decrease of shear-wave travel time when mean effective stress increased, with increased loading corresponding to a reduction of the void ratio. This behavior translates to an increase to shear wave velocity during the consolidation phase. For the consolidation experimentation, the reduction of shear-wave travel times was between 0.90 ms and 0.55 ms, corresponding to initial and final mean effective stresses of 21 kPa and 209 kPa, respectively.

3.8 RELATION OF SHEAR-WAVE VELOCITY AND MEAN EFFECTIVE STRESS

Figure 3-6 shows the relationship of the shear-wave velocity (V_s) to the mean effective stress (p') of the experimental data during the consolidation process. The relation is described using Equation 3-4. Table 3-5 lists the experimental factors α_s and β_s resulting from the V_s - p' relations of the tested samples. The range of α_s was 22.8 to 85.7 m/s, with an average of 47.35 m/s, whereas the range of the β_s exponent was 0.18 to 0.418, with an average of 0.289. The parameter α_s is a stress-dependent state property that quantifies the variation of the shear-wave velocity as a function of the change in mean effective stress (Lee and Santamarina 2005, Cha et al., 2014). The lower the α_s factor, the higher the variation of the shear-wave velocity with change of the mean effective stress change. However, the α_s parameter is strongly influenced by structure, as indicated by coarse-grained materials (sandy sediments) have a high α_s and low β_s. Conversely, fine-grained sediments have a low α_s and high β_s.

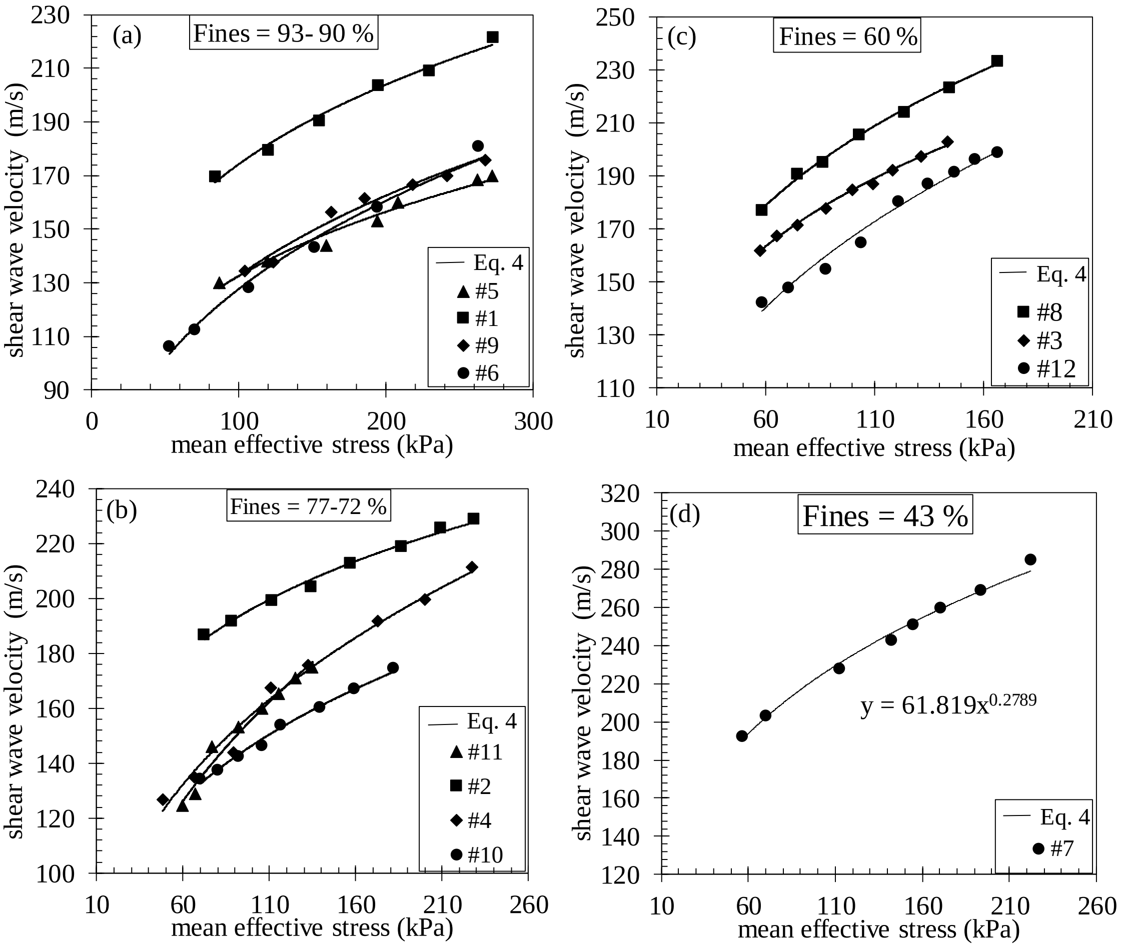

Figure 3-6. Relations between shear-wave velocity (Vs) and mean effective stress of the samples.

The α_s factor and β_s exponent are useful, practical indicators of the grain size and type parameters of sediments. This was evident when different percentages of grain size and type parameters of sediment were analyzed, and the changes in those parameters and the resultant β_s and α_s were observed. This study investigated α_s and β_s with the specific constituents of percent fines, silt fraction (SF), and clay fraction (CF), and LL.

Table 3-5. Resultant fitting parameters α_s and β_s .

Sample#	α_s	β_s
1	61.317	0.227
2	85.651	0.180
3	60.791	0.242
4	32.131	0.346
5	44.056	0.239
6	27.846	0.331
7	61.819	0.279
8	62.547	0.257
9	34.397	0.293
10	40.316	0.280
11	23.189	0.414
12	34.283	0.3441

3.9 CORRELATING α_s AND β_s TO GRAIN-SIZE PARAMETERS

Percent fines, silt fraction (SF), and LL are the material properties representing particle size and composition features of the sediment structure. Thus, percent fines, SF, and LL were correlated to α_s. Figure 3-7 shows that α_s is a power function of SF, percent fines, and LL, which characterize the grain size and composition component, respectively.

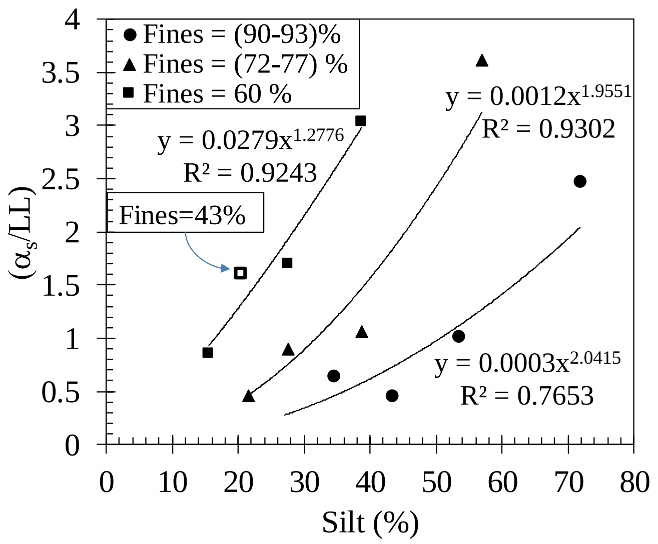

Figure 3-7. The relationship between α_s and silt percent and LL.

There are three relations shown in Figure 3-7 that describe three categories corresponding to the change in percent fines. The relations had a much better correlation coefficient when the effect of LL was included than when LL was not included. The data were assigned to one of the three groups, depending on percent fines, which was readily quantified. These categories were 90–93 percent, 72–77 percent, and 60 percent. Increasing the percentage of fines led to increasing the rate coefficient (i.e. slope of the relations) from 1.28 to 1.95 and 2.04, and decreasing the intercept from 0.0279 to 0.0012 and 0.0003. The open box in Figure 3-7 represents percent fines = 43, which was close enough to the group of 60 percent fines, and agreed with the general trend of the relation. Equation 3-7 is the general power function describing α_s versus silt percent. Table 3-6 presents the fitting factors (B_1 and B_2) of each group of percent fines shown in the figure.

$$\alpha_s = LL \cdot \left(B_1 \cdot SF^{B_2} \right) \tag{3-7}$$

Table 3-6 Fitting factors for the general α_s parameter equation.

No.	Percent Fines (%)	Fitting Factors		
		B_1	B_2	R^2
1.	90 -93	0.0003	2.0415	0.77
2.	72-77	0.0012	1.9551	0.93
3.	60	0.0279	1.2776	0.92

Cha et al. (2014) found that there was a strong correlation between the α_s and β_s parameters. For this current study, α_s was used to predict β_s. Figure 3-8 shows the inverse exponential relation between α_s and β_s, which has a good R^2 of 0.84. Equation 3-8 expresses the inverse exponential correlation between α_s and β_s, and agrees with results of previous studies (Cha et al., 2014, Oh et al., 2017).

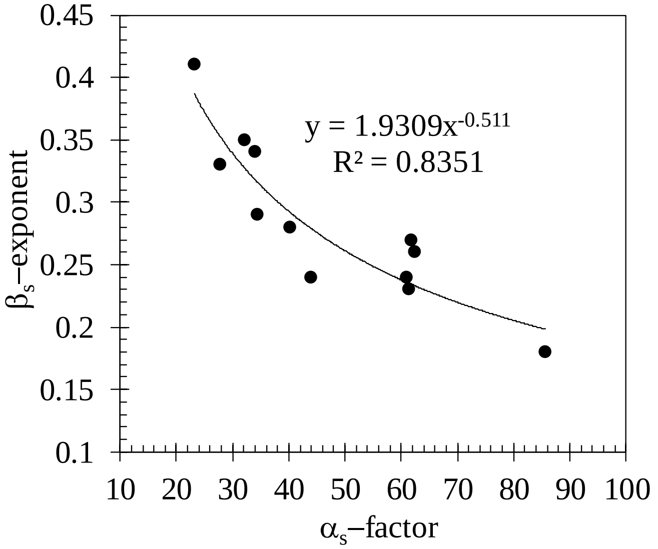

Figure 3-8. The inverse relationship between the experimental factors α_s and β_s.

$$\beta_s = 1.9309 \cdot \alpha_s^{-0.511} \tag{3-8}$$

3.9.1 Effects of Stress History and Structure on the C_f Parameter

The p'_c value has fundamental importance in describing the stress history of the sediment. The p'_c is the interface between the reversible (elastic or recompression) and irreversible (plastic or virgin) behavior of sediments when subjected to loading (Brain et al., 2011). The C_f was found to be a strong function of preconsolidation pressure, p'_c, as a state condition, and this function became stronger when sediment structure was considered, as reflected in the α_s parameter. The stress history and structure term is shown in Figure 3-9 as the product $\alpha_s \cdot p'_c$. The variation of C_f with stress history and structure is given by Equation 9. The data show that the relation is well correlated with R^2 equal to 0.93.

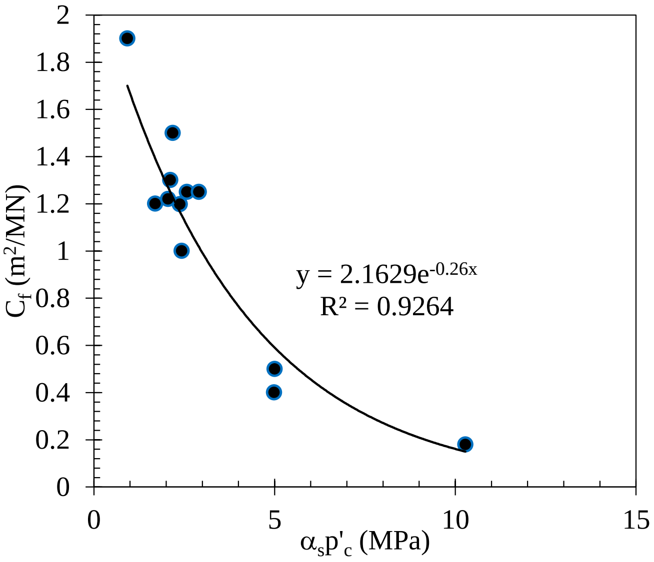

Figure 3-9 The variation C_f with stress history and structure.

$$C_f = 2.163 \cdot \exp\left(-0.26 \cdot \alpha_s p'_c\right) \tag{3-9}$$

3.10 PERFORMANCE OF THE PREDICTION EQUATION

Herein, the parameters C_f, β_s and α_s were investigated and approximated using percent fines, SF, and LL. Equations 7-3 to 9-3 were all substituted into Equation 3-5 to produce a prediction equation that estimates consolidation behavior $[e - \log(p')]$ as a function of shear waves velocity and various depositional properties. An additional benefit of using the approximations proposed in this study is that no a priori consolidation data is required to predict the full consolidation curve. The performance of the proposed prediction equation was compared with measured data for verification. Figure 3-10 shows predicted and measured results of the $[e-\log(p')]$ relations characterizing the consolidation behavior of the samples. The predicted curves show good agreement with the measured data. In general, the amount of volumetric change during the loading had affected by the percent of fines, SF, and LL, and this allowed the consolidation curves could be controlled and recognized. The general equation was reliable for quantifying the consolidation mechanism of sediment in response to the controlling depositional factors.

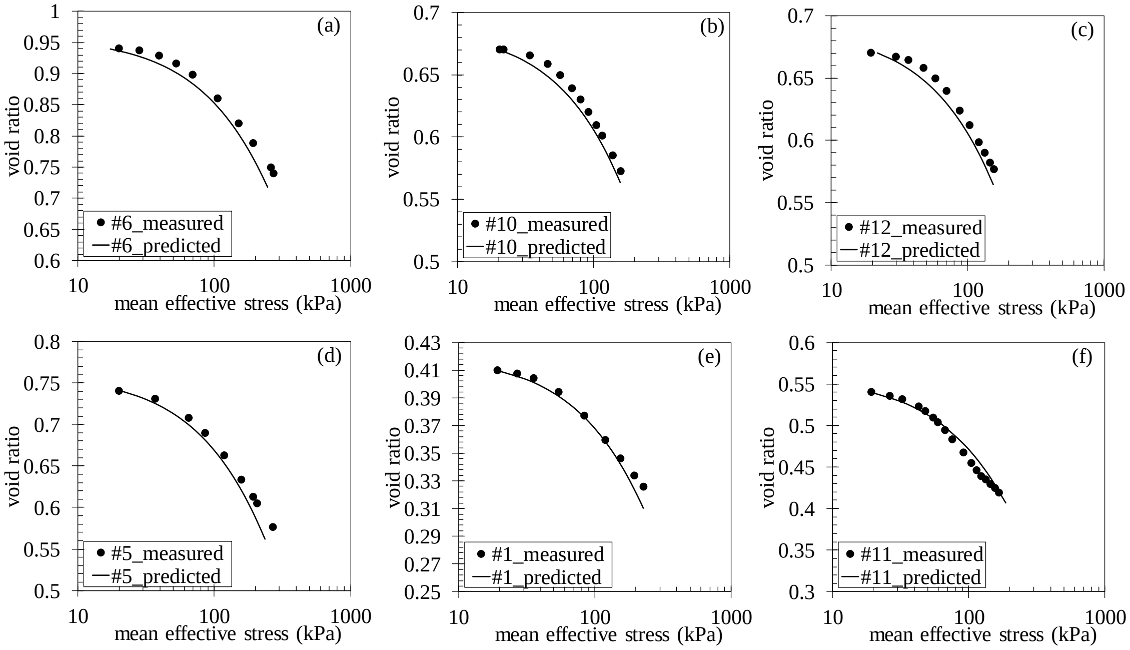

Figure 3-10. Results of consolidation curves of the measured data and the predicted data based on Equation 5.

3.11 VALIDATION OF THE CONTINUOUS FUNCTION

Figure 3-11 demonstrates the performance of the presented continuous function (Equation 5) in simulating experimental consolidation data from the literature (Fam and Santamarina 1997, Chang et al., 2011, Ahmed 2017, Oh et al., 2017). The figure also shows a comparison between Equation 3-5 and the prediction methodology presented by Oh et al. (2017), noted as dashed lines in the figure. The Oh et al., (2017) approach was chosen for comparison because both this approach and the proposed continuous function explicitly used shear wave velocity measurements for prediction of consolidation behavior. The other prediction methodologies in literature, such as Liu et al., (2013) and Horpibulsuk et al., (2016), were not addressed in this comparison since they do not explicitly used shear waves velocities in the $e-\log\left(p'\right)$ prediction.

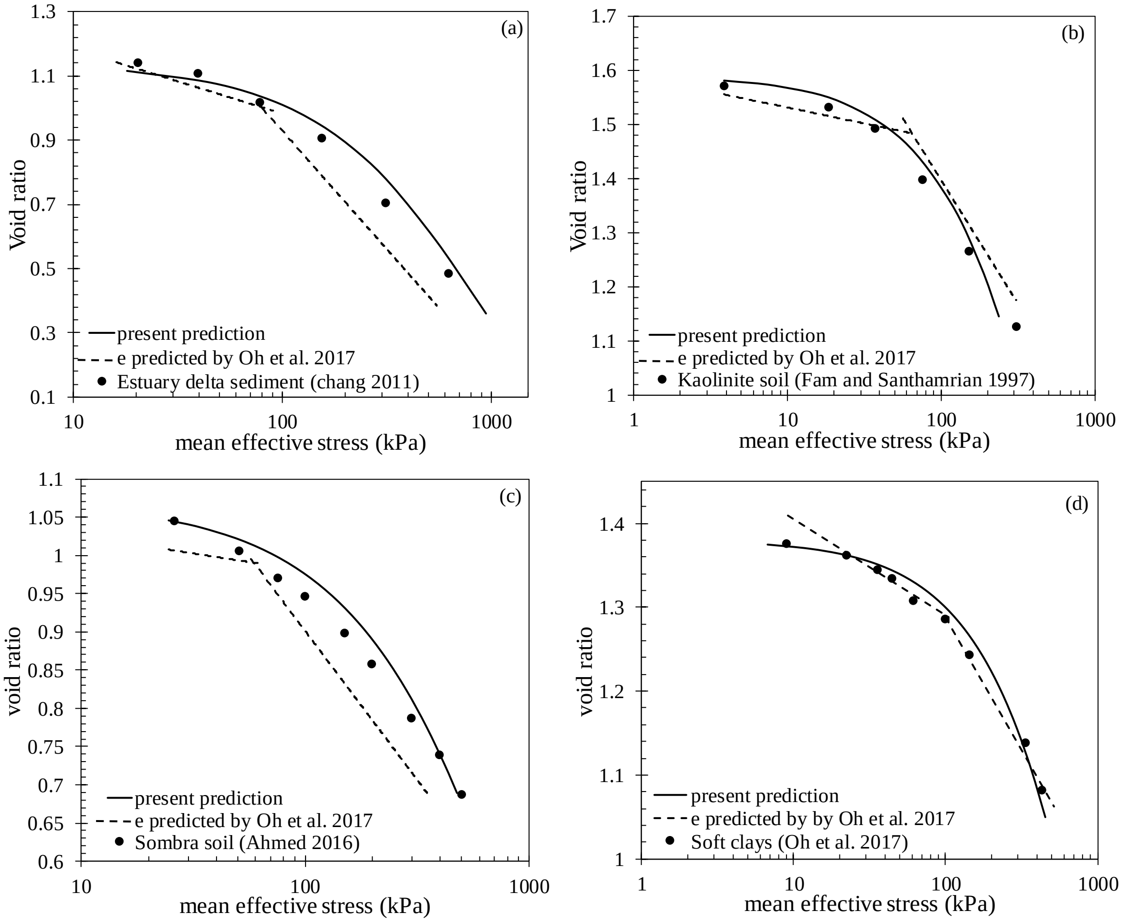

Figure 3-11. Comparison real consolidation data from the literature to validate performance of the present prediction in this study.

As seen in Figure 3-11, the proposed prediction methodology provides a continuous function that does well in capturing both the recompression and virgin compression portions of the consolidation curves. The proposed function also gives a good indication of the effective preconsolidation stress, p_c' even though the preconsolidation stress is very sensitive to the compressibility. The Oh et al., (2017) approach requires two bilinear equations to predict the entire $e-\log\left(p'\right)$ curve. Although The Oh et al., (2017) approach does well with predicting the effective preconsolidation stress p_c', it does not predict the overall consolidation behavior as well as the proposed method.

3.12 INFERRING UNDRAINED SHEAR STRENGTH (SU)

Void ratio has been identified as a crucial parameter that influences undrained shear strength under loading (Bartetzko and Kopf 2007, Oh et al., 2017, Zhang et al., 2017, Choo et al., 2018). Many of the cited studies have found a plausible linear relationship between the undrained shear strength and the void ratio, which was then supported by experimental results. In this study, analysis of the CIU triaxial tests showed an agreement with these previous studies. Figure 3-12 shows a negative linear correlation between the normalized undrained shear strength $\left(S_u / p_c'\right)$, and the void ratio, with a strong correlation coefficient (R^2 = 0.875). This relation is given in Equation 10 as:

$$\frac{S_u}{p_c'} = 1.4377 - 1.1245\left(e\right) \tag{3-10}$$

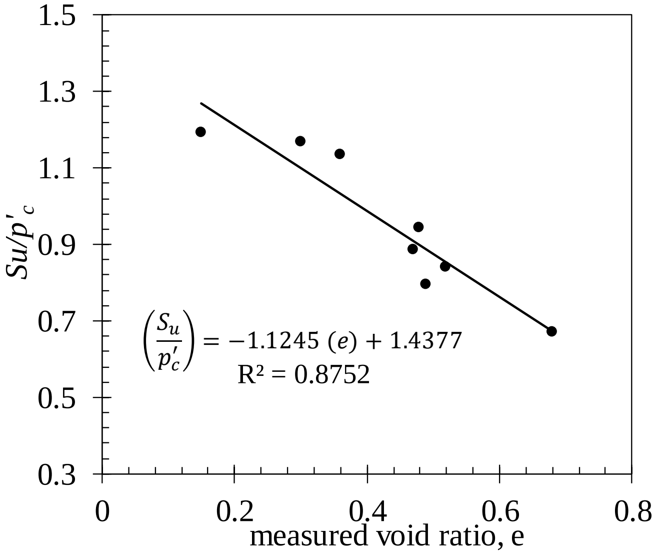

Figure 3-12. The relationship between undrained shear strength and void ratio.

Substituting the continuous equation for void ratio (Equation 3-5) into Equation 3-10 allows the undrained shear strength to be predicted in a manner that implicitly considers the depositional process, stress history, and sediment structure. Equation 11 is the final form of S_u as a function of e, p_c', and C_f:

$$\frac{S_u}{p_c'} = 1.4377 - 1.1245 \cdot e_0 \cdot \exp\left[-C_f \cdot \left(\frac{V_s}{\alpha_s} \right)^{\left(\frac{1}{\beta_s}\right)} \right] \tag{3-11}$$

This general form of Equation 3-11 concurs with the findings of Bartetzko and Kopf (2007), who noticed that the relationship between strength and void ratio is affected by composition, particle sizes of sediment, and increasing depth (stress history). Void ratio and preconsolidation pressure most likely have the most influence on the undrained shear strength of sediments.

Equation 3-11 was applied to field data reported by Tong et al., (2018). Figure 3-13 shows the estimated undrained shear strength profile of the upper part of fine-grained Quaternary sediment in Yangtze Delta deposits. The figure shows the two approaches used to infer undrained shear strength, S_u. The first approach used the field standard penetration test (SPT), N_{60}, to infer S_u, and the second approach used Equation 3-11 (the prediction equation in this study). The equation used the initial physical properties, initial void ratio, grain size percentages, and liquid limit that were provided in Tong et al., (2018). Figure 3-13 also shows an outlier appeared and was accounted for as a possible error might be in the original tested data that caused the overestimation of S_u .In general, the results agree well with the general trend of the profile and increasing shear strength with depth.

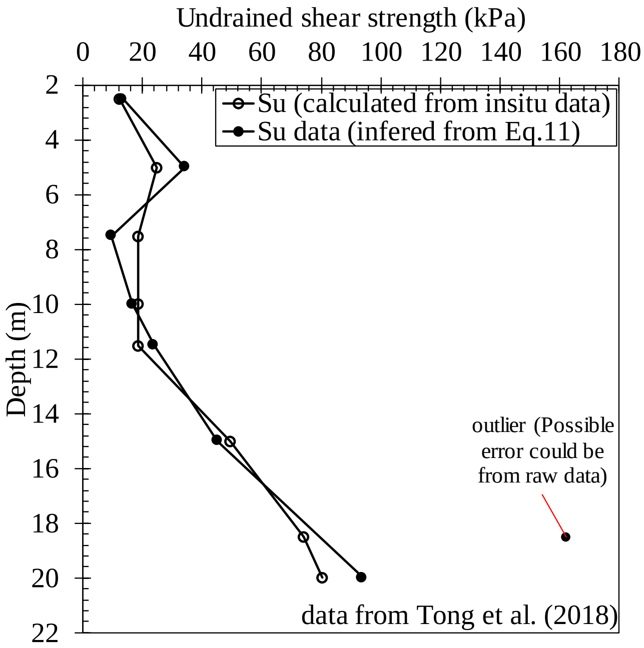

Figure 3-13. Undrained shear strength profile with depth.

CHAPTER 4

Constitutive Model for Predicting Stress Strain Behavior of Fine-Grained Sediments using Shear Wave Velocity

4.1 INTRODUCTION

The deposition process for fine-grained sediments produces inherent spatial variability within a soil deposit. Variations of material types, state conditions (e.g. density, degree of saturation), and stress states (e.g. in situ stresses, pre-consolidation stresses) dramatically affect the mechanical response of a sediment to an applied stress. In this context, mechanical behavior describes the shear and deformation responses of sediments. Thus, because of this spatial variability, the mechanical behavior of a soil deposit is a function of the location within the mass. It therefore becomes apparent that it is critical to measure the variability of soil properties within a soil mass and assess how that variability affects the three-dimensional mechanical behavior of the mass. However, such measurements are difficult to obtain and are not well understood. The traditional approach to characterizing a soil mass is to take samples at discrete locations within the mass and perform a variety of laboratory tests on each sample. The testing is often destructive in nature, highly invasive to the soil mass, time consuming, and economically inefficient. For many projects, economic considerations limit the number of samples that can be collected and precludes all but basic index testing. This problem is particularly exacerbated for a highly variable deposit. For this case, it typically takes an unreasonable number of samples, subjected to a multitude of loading conditions to adequately predict behavior representative of the deposit. Because of these limitations, the average or bulk values of soil parameters are typically used to characterize a soil mass and to predict the potential mechanical behavior. This approach often leads to unexplained deviations between actual and predicted behavior. Geophysical methods, specifically those methods that utilize seismic wave velocities, allow for the determination of material properties and behavior over a large spatial domain.

Low-strain mechanical wave (i.e. seismic wave) velocity is a function of the state conditions and material properties of the medium through which the wave propagates (Santamarina and Cascante 1996; Santamarina et al. 2001; Patel and Singh 2009). As a result, information about the mechanical behavior of a medium at a given stress state can be directly obtained from the measured wave velocity through the medium. In addition, the material properties of the medium do not change in response to propagation of the seismic waves. The information obtained by the interaction between the wave front and the medium can be used to non-destructively evaluate material properties.

In particular, several researchers (Santamarina and Aloufi 1999; Aris et al. 2012; Oh et al. 2017) have used shear wave velocity (V_S) to determine the mechanical behavior of sediments. It is generally assumed that effective stress governs the shear stiffness of uncemented sediments when capillary effects are negligible. In this case, the shear wave velocity is related to the effective stresses acting in the direction of wave propagation and in the direction of particle motion. Thus, it can be concluded that variations in V_S reflect changes in effective stress and in state properties that affect particle motion, such as void ratio and water content (Aris et al. 2012; Choo et al. 2017; Oh et al. 2017). These state properties and conditions can be utilized to infer input parameters for advanced constitutive soil models.

Critical state soil mechanics (CSSM) is particularly well suited for interpreting soil behavior. CSSM theory is a unified mathematical framework that describes the mechanical response of soils at constant effective stress or at constant volume. CSSM is very applicable for saturated, fine-grained sediment under normally consolidation conditions (Jia 2018). CSSM-based models are able to estimate the consolidation behavior and to provide a plausible estimation of the shear and stress path behavior of the soil (Bryson and Salehian 2011). Fundamental input parameters for CSSM-based models that describe the consolidation and shear behaviour are well correlated to basic material properties, such as grain-size characteristics and consistency limits. These material properties can be subsequently evaluated using shear wave velocity (Hussien and Karray 2016). In addition, effective stresses and state properties, such as void ratio can also be readily inferred from shear wave velocities (Cunning et al. 1995; Oh et al. 2017). However, under the CSSM framework, utilizing shear wave velocities to predict stress-strain constitutive behavior has not been insightfully addressed. This paper presents a methodology for using elastic shear-wave velocity under a critical state framework to predict the shear behavior and critical stress paths of a wide range of fine-grained sediments. The paper also investigates the efficacy of the link between CSSM-based model input parameters and basic index properties for a variety of these sediments. This study establishes the fundamental theory that will serve as the basis for considering the effects of spatial variability on the behavior of a soil deposit. This study is crucial to developing efficient and reliable analytical and design methodologies for infrastructure constructed in various fine-grained depositional environments.

4.2 THEORETICAL DEVELOPMENT

4.2.1 Critical State Definition

The fundamental concept a critical state soil model is that a unique failure surface exists that defines failure of a soil irrespective of stress history or stress path followed. In general, the critical state is a constant stress state characterized by continuous shear deformations at constant volume or at constant effective stress. CSSM theory shows that the stress-strain response of a sediment is a function of the material properties of the sediment, the initial state conditions, and the initial stress state.

The original cam clay (OCC) and modified cam clay (MCC) soil models are used as a basis for the critical state framework used in this study. Figure 4-1 presents the relations and parameters used for the critical state formulation of the consolidation and shear behavior. Figure 1a shows that the consolidation process in CSSM is characterized by the relationship between mean effective stress (p'), which is defined as $p' = (\sigma_1' + \sigma_2' + \sigma_3')/3$ (where σ_1', σ_2', and σ_3' are the major, intermediate, and minor principal stresses, respectively), and the void ratio (e) plotted in $e - \ln(p')$ space. Mean effective stress p' implies that the stress responses are obtained from the contact forces created between the grains (Verruijt 2018).

In Figure 1a, the critical state compression indices are given in terms of the slope of the normal consolidation line (NCL) (i.e. λ) and the slope of the unloading/reloading line (κ). Figure 1b presents the yield surfaces of both models in $q - p'$ space, where q is the deviatoric stress; given as $q = \sigma_1' - \sigma_3'$.

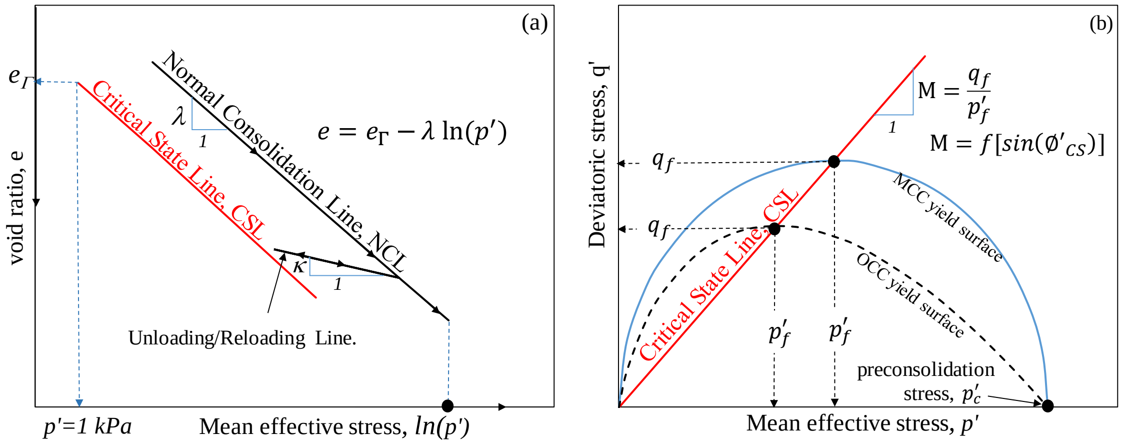

Figure 4-1. Typical relationships of critical state concept and its important parameters used to predict: (a) the consolidation behavior and (b) the shear behavior of soils.

The yield surface for the MCC model is described by an ellipse and is given as

$$q = \pm Mp'\sqrt{\left(\frac{p'_c}{p'} - 1\right)} \qquad \text{for MCC yield surface} \qquad (4\text{-}1)$$

whereas, the OCC model is described by a logarithmic spiral given as

$$q = \pm Mp' \ln\left(\frac{p'}{p'_c}\right) \qquad \text{for OCC yield surface} \qquad (4\text{-}2)$$

The mean effective preconsolidation pressure (p'_c) controls the size of the yield surface. The parameter M is the slope of the CSL in $q - p'$ space and is often defined under triaxial compression as a function of ϕ'_{cs} given as

$$M = \frac{6\sin\phi'_{cs}}{3 - \sin\phi'_{cs}} \qquad (4\text{-}3)$$

Both models assume an associated flow rule where it is assumed the plastic potential function coincides with the yield function.

It is worth noting that it was not the intent of the current study to demonstrate the efficacy of the OCC and MCC soil models for predicting soil behavior. Although there are many advanced critical state soil models reported in the literature, most CSSM-based models are hierarchical extensions of the OCC and MCC models models (Yu 1998; Wheeler et al. 2003; Yao et al. 2008; Sivasithamparam and Castro 2016). Thus, the OCC and MCC models are sufficient to show the viability of using elastic shear wave velocities and describe aspects of mechanical behavior within the critical state concept.

4.2.2 Variation of Shear Wave Velocity with Mean Effective Stress

For a particulate material undergoing isotropic consolidation, increasing the mean effective stress results in an increase in the particle packing density and a subsequent increase in the particle-to-particle contact stresses. This increase in particle packing density and contact stresses will cause an increase in the measured elastic-wave velocities of materials (Santamarina et al. 2001; Choo et al. 2018). The relation between shear-wave velocity and mean effective stress is well correlated and is often described by a power function (Santamarina et al. 2001; Oh et al. 2017).

For drained shear conditions, there is a volume change associated with the shearing process and therefore the power function relating the mean effective stress, p' with the shear-wave velocity, V_S is observed, similar to the relation observed during the consolidation phase (Santamarina et al. 2001). For undrained loading conditions, increasing the total mean stress (p) results in an increase in the porewater pressure (*u*). Consequently, a reduction in mean effective stress is observed based on effective stress theory, $p' = p - u$. In addition, there is no volume change associated with undrained shear. The power function observed during the undrained shear phase is no longer a functional change of particle packing density (i.e. volume change). Some researchers (Tanizawa 1994; Teachavorasinskun and Akkarakun 2004; Baxter and Sharma 2012) have reported that there is no clear change in shear wave velocity under undrained conditions, given that there is no change in volume (or void ratio). However, Teachavorasinskun and Amornwithayalax (2002) found that there is sufficient association between p' and V_S for small ranges of strain under undrained conditions. The relation between $V_S - p'$ under undrained loading conditions cannot be ascribed to the stress-induced changes in void ratio. This relation is attributed to an increase in stiffness of the initial microstructure of sediments and an increase in the inter-grain contacts that occur under small strain conditions (Aris et al. 2012). This conclusion is supported by experimental observations that variations of V_S do not only depend on changes in void ratio, but appear to depend also on stress history, stress state, cementation, sediment type, and water content (Moon and Ku 2018). The intent of the current study was to investigate the variation in the shear wave velocity under undrained conditions of a wide range of fine-grained sediments and to establish a functional relation between the two measures.

4.3 MEANS AND METHODS

4.3.1 Test Soils

As was previously mentioned, the intent was to develop a basic constitutive model framework using a wide range of sediment types. The samples used in this study were created by mixing several selected natural soils. These natural (or source) soils were sampled from different sites in the state of Kentucky. Source soils were mixed with pre-determined percentages of fines (diameter < 0.075 mm), silt (0.075 mm < diameters < 0.002 mm), and clay (diameters < 0.002 mm) to generate targeted grain-size distribution curves (i.e. synthetic samples). Further details of the source soils and the mixing procedure are found in Muttashar et al. (2018b). The basic index properties of the samples required for this study included grain-size distribution characteristics such as percent Fines, clay fraction (CF), and silt fraction (SF); and consistency limits (Atterberg limits) such as liquid limit (*LL*) and plasticity index (*PI*). The particle size analysis was performed for the source soils according to (ASTM D422 2007) and Atterberg limits testing was performed according to (ASTM D4318 1994).

The samples were categorized into several groups based on percent Fines and the ratio of the clay fraction-to-silt fraction (CF/SF). The four discrete groups of samples based on percent Fines included: 100–85 percent (Group #1), 85–70 percent (Group #2), 70-55 percent (Group #3), and 55-40 percent (Group #4). The Group #1 samples represented soils that are traditionally referred to as silty clay to clay. The Group #3 samples represented soils that are traditionally referred to as clayey silt to silt. The Group #2 sample represented a transitional sample from Group #3 to Group #1 and the Group #4 sample represented a transitional sample from coarse grain sediments to fine-grained sediments. The additional grouping based on CF/SF allowed for a distinction of samples that had the same percent Fines, but different percentages of clay and silt. The CF/SF ranged from 0.2 to 2.4, which covered fine-grained sediment types ranging from silt-predominant to clay-predominant sediments, respectively (Muttashar et al. 2018a). Table 1 shows the index properties of the samples used in this study.

Table 4-1. Index properties of the tested samples.

Groups (Range of %Fines)	Sample #	Fines (%)	CF/SF	*LL* (%)	*PI* (%)	*Gs*
Group #1 (100-85)	1	93.6	2.4	74.5	31.0	2.69
	2	91.5	1.1	60.5	15.4	2.70
	3	90.2	0.6	37.8	8.0	2.68
Group #2 (85-70)	4	82.0	1.2	55.0	23.0	2.70
Group #3 (70-55)	5	60.0	1.1	37.0	15.1	2.67
	6	60.0	0.3	20.0	4.0	2.66
	7	55.9	2.5	35.0	10.0	3.57
Group #4 (55-40)	8	43.5	1.1	38.0	12.0	2.66

Fines = % passing #200 sieve; CF = clay fraction = dia < 0.002 mm; SF = silt fraction = 0.002 ≤ dia ≤ 0.075 mm; LL = liquid limit; PI=plasticity index; Gs = specific gravity.

4.3.2 Triaxial Test Sample Preparation

Remolded samples were prepared for triaxial testing using a strain-controlled sedimentation method developed for this study. Samples were prepared by first making a slurry from mixing air-dried samples with tap water. The water content of the slurry mixture was approximately two times the liquid limit. This water content produced a stable mixture without the particles settling out of solution (Germaine and Germaine 2009). The mixture was then poured into a sample split mold and precompressed at a controlled displacement rate (0.025 mm/min for silt-predominant samples; 0.019 mm/min for clay-predominant samples) to create uniform samples having dimensions of 152.4 mm in height and 68.5 mm in diameter. The targeted unit weight of the samples was approximately 15.09 kN/m^3. The resedimentation technique is described with further details in Muttashar et al. (2018a). The split mold was next dismantled and the sample was placed in a triaxial cell. The cell was then mounted in the load frame to start the triaxial test.

4.3.3 Triaxial Tests and Shear Wave Velocity Measurements

Several isotropically consolidated, undrained triaxial compression tests (CIU TXC) were performed for this study, according to (ASTM D4767 2004). Testing was performed using an automated triaxial system manufactured by Geocomp Inc., Acton, MA. During the saturation phase, the samples were saturated at B-value greater than or equal to 0.95 before proceeding to the consolidation stage.

To capture consolidation characteristics pertinent to OCC and MCC models, the specimens were normally consolidated in three different loading steps: loading to 206.7 kPa, unloading to 69 kPa, and reloading to the final preconsolidation pressure of 344.5 kPa. Upon achieving the final preconsolidation pressure, the samples were loaded until failure under undrained conditions and at a constant strain rate of 0.2 percent strain/min. The maximum axial strain used for testing ranged between 20 and 25 percent, which was sufficient to determine yield stress and critical state stress.

Shear-wave velocity was measured throughout the consolidation and shear stages, along the axis of samples using two bender elements (BE). These elements are electro-mechanical transducers (transmitter and receiver elements) used to generate and receive elastic waves. These BEs were inserted in the top and base caps of the triaxial cell. A single-pulse sinusoidal input signal was used for the shear-wave propagation. The cross correlation method, as implemented in the automated Bender Elements Analysis Tool (BEAT) software (GDS Instruments, Hampshire, United Kingdom), was used to detect the time interval of the shear wave. The wave arrival times were recorded at multiple intervals during the shear phase. Further details on the bender elements and the measurement techniques used for this study are given in Muttashar et al. (2018a).

4.4 SHEAR DATA AND TRENDS

Figure 4-2 shows the shear-strain behavior observed during the triaxial testing. The figure shows the deviatoric stress, q, versus axial strain, ε, for the four groups of the samples. Figure 2 shows that the four sample groups had different shear stress-strain responses under the same stress history conditions (i.e., normally consolidated state with preconsolidation pressure of 344 kPa). These differences are ascribed to the complex interactions between three components: percent Fines, CF/SF, and consistency limits (*LL* and *PI*). Although not definitive, a general observation was that the silt-predominant sediment samples (0.2 ≤ CF/SF ≤ 1.0) produced higher strengths than the clay-predominant sediments samples (1.0 < CF/SF ≤ 2.4). Also, a strain hardening response was observed in some silt-predominant samples. In general, samples with a high percentage of silt-sized particles behave transitionally between clay and granular soil and thus can exhibit semi-clay or semi-granular behavior (Polidori 2015). These materials tend to have lower plasticities and higher internal friction angles, which would explain the higher initial stiffness of the silt-predominant samples under similar confining pressures (Bryson et al. 2017). In comparison, samples with high percentages of clay-sized particles tended to exhibit strain softening beyond the peak stress. These samples also had a loose trend of increased porewater pressure response with increased clay content.

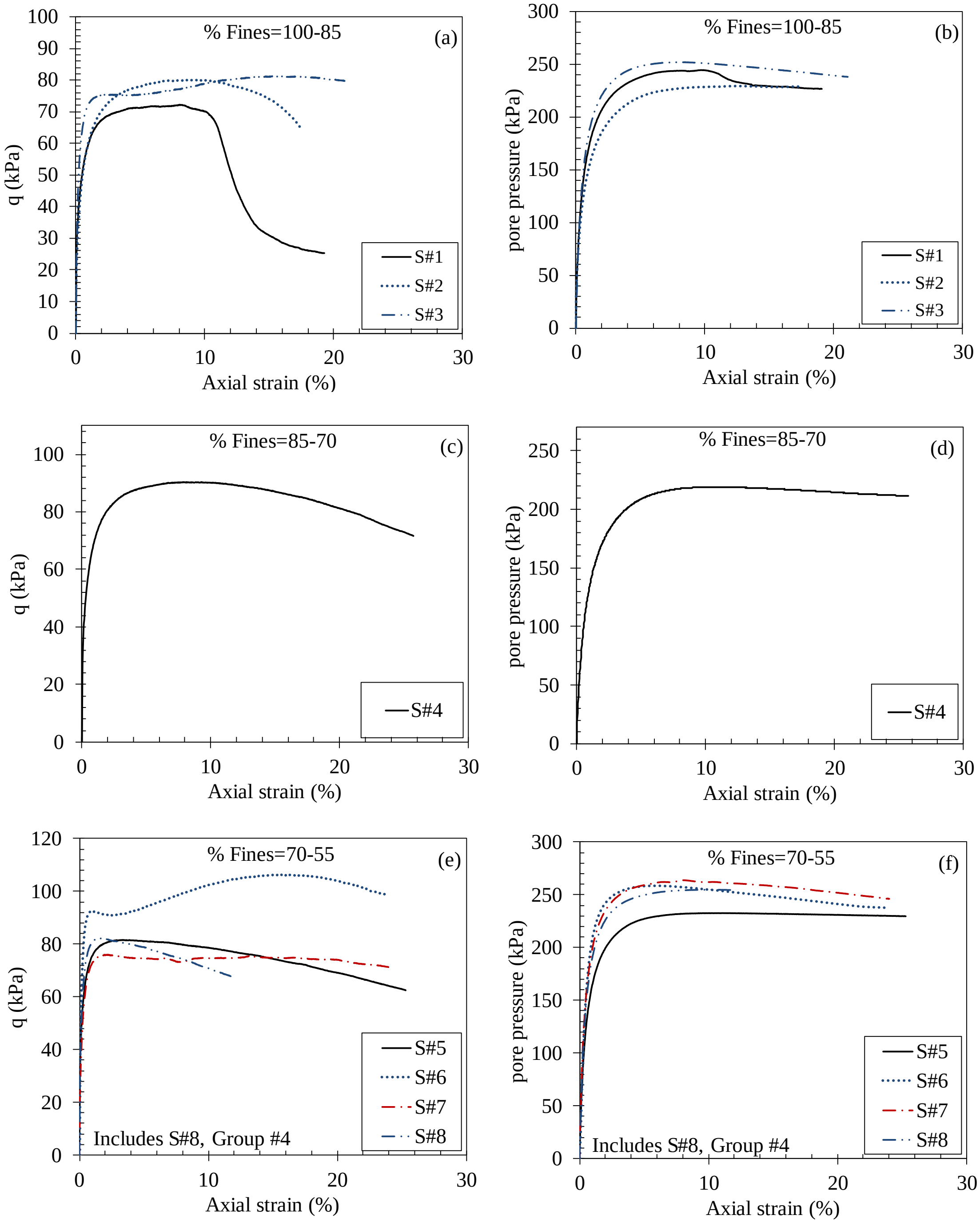

Figure 4-2. The shear stress-strain behavior of the sediment samples: (a) deviatoric stress versus axial strain for Group #1; (b) pore water pressure versus axial strain for Group #1; (c) deviatoric stress versus axial strain for Group #2; (d) pore water pressure versus axial strain for Group #2; (e) deviatoric stress versus axial strain for Group #3 and #4; (f) pore water pressure versus axial strain for Group #3 and #4.

The trends observed for the stress-strain and porewater pressure responses of the samples were generally persistent for the stress paths. Figure 4-3 presents the effective stress paths of the sample groups. Again, although the behavior was not definitive, it was observed that the silt-predominant sediment samples tended to produce higher initial stiffness responses than the clay-predominant sediments samples. Here, initial stiffness is characterized as the initial increase in deviator stress with a change in the mean effective stress. Higher stiffness corresponds to higher increases in deviator stress over smaller changes in mean effective stresses.

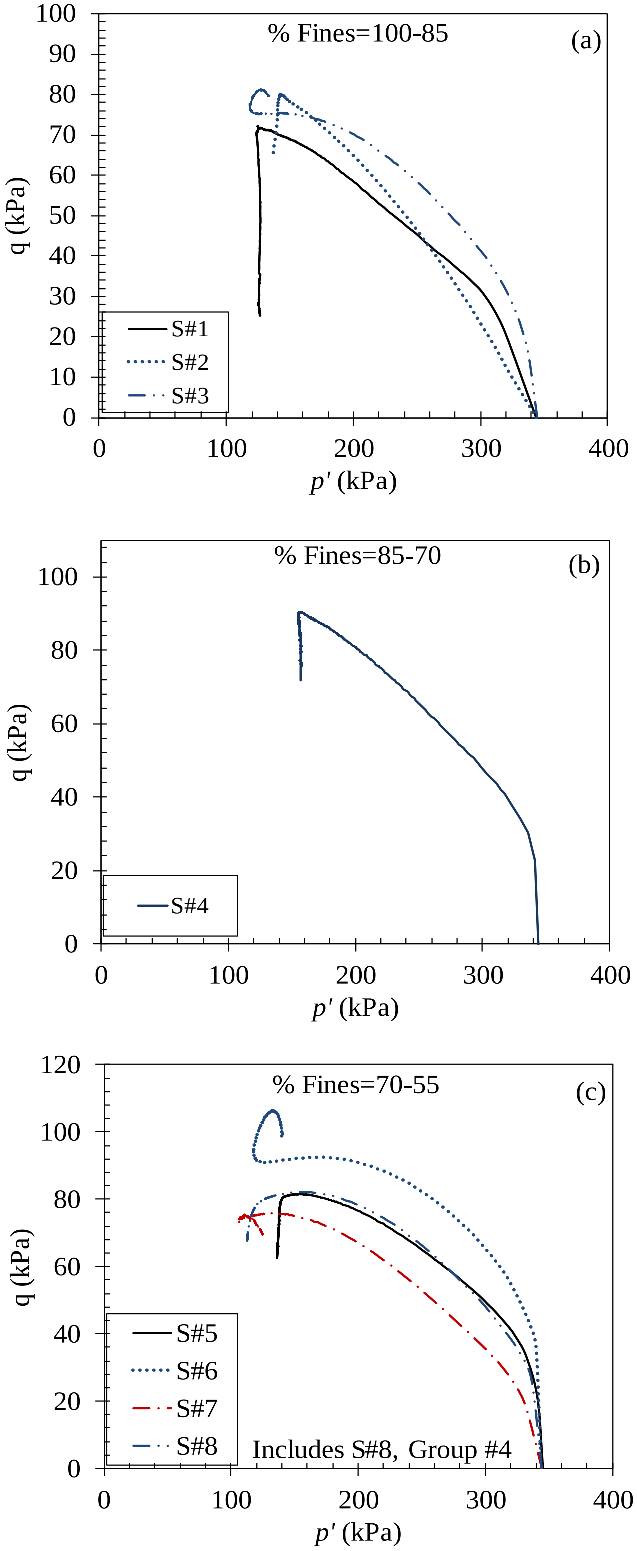

Figure 4-3. Effective stress paths of the four sample groups: (a) Effective stress paths for Group #1; (b) Effective stress path for Group #2; (c) Effective stress paths for Groups #3 and #4.

4.5 VARIATIONS OF SHEAR WAVE VELOCITIES WITH MEAN EFFECTIVE STRESS DURING UNDRAINED SHEAR

The observations reported by researchers that variations of V_S do not depend solely on changes in void ratio, but also depend on sediment type, stress conditions, and initial state conditions was the basis for this study. The significance of these observations is that measures of V_S can be used to evaluate undrained shear behavior, which has be shown to be heavily influenced by initial state and stress conditions for a given soil type (Casey and Germaine 2013). Traditionally, change in shear wave velocity is evaluated with respect to changes in effective stress (Santamarina et al. 2001). For this study, the variation in mean effective stress under undrained conditions was evaluated with respect to change in V_S. Figure 4 shows the $p' - V_S$ relations for three typical Samples (#1, #2, and #5). In the figure, mean effective stress and shear wave velocity were normalized to the initial state values (where p'_o = mean effective stress at the beginning of shear; V_{So} = shear wave velocity at the beginning of shear). The purpose of the normalization was to produce a dimensionless scale that connected the measured data to the current state. Given that the measured shear wave velocity for a particular sediment sample will vary as a function of the initial stress state, the normalization allowed for sediments prepared at similar densities to be compared directly.

4.6 USING A POWER FUNCTION TO DESCRIBE THE RELATION BETWEEN MEAN EFFECTIVE STRESS AND SHEAR WAVE VELOCITY

At the beginning of shear, the normalized parameters were both at unity. During shear, the normalized mean effective stress (p'/p'_o) decreased to the values at peak stress as a positive function of the normalized shear wave velocity (V_S/V_{So}). The average peak mean effective stress for the samples shown in Figure 4 is approximately $0.44p'_o$. The decrease of both parameters was indicative of normally consolidated behavior where increasing porewater pressures during shear resulted in a decrease in effective stresses. The decreasing effective stress also implies a decrease in particle-to-particle contact stress, which most likely explains the decreasing shear wave velocity with shear. Beyond peak stress conditions, the shear wave velocities became higher than the initial velocities and the function shown in Figure 4-4 was no longer valid.

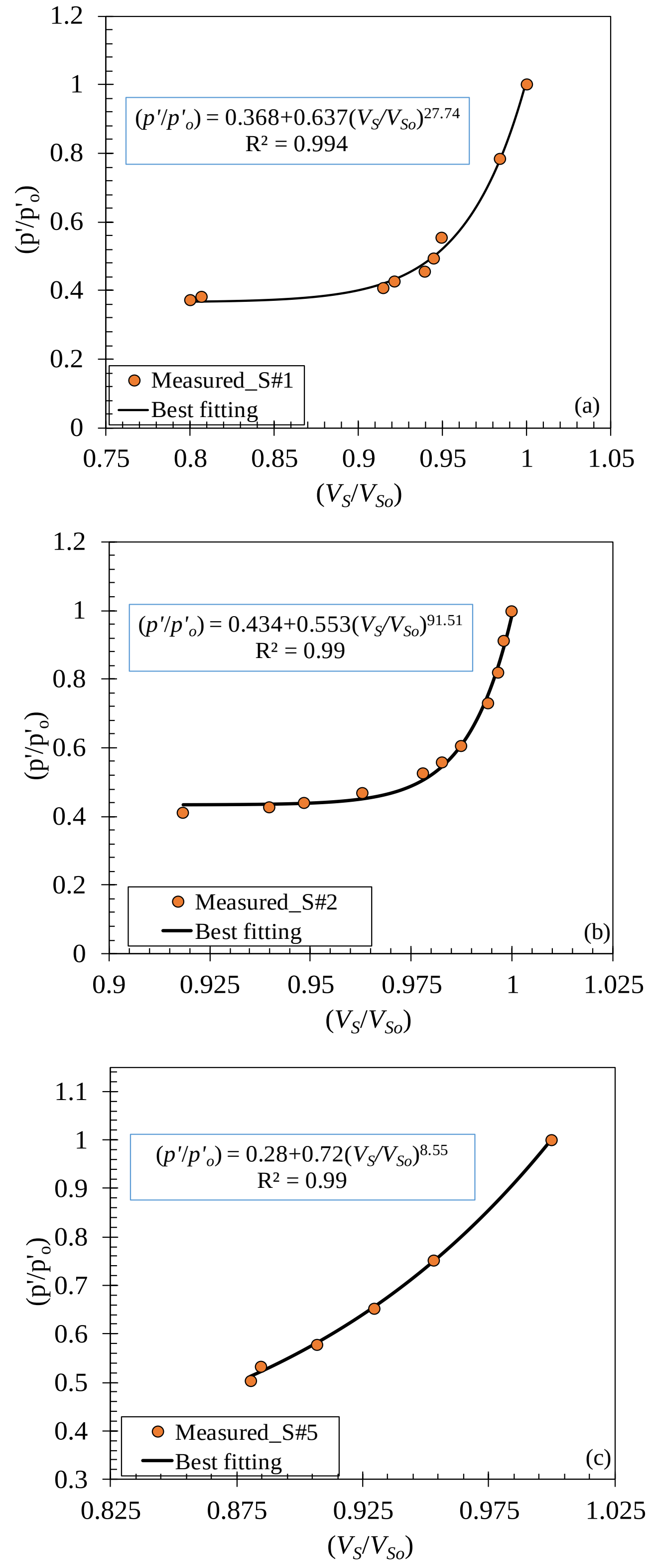

Figure 4-4 The $V_S - p'$ correlation during undrained shear process: (a) the $V_S - p'$ correlation for Sample#1; (b) the $V_S - p'$ correlation for Sample#2, (b) the $V_S - p'$ correlation for Sample#5.

Figure 4-4 shows that the relation between the normalized mean effective stress and the normalized shear wave velocity can be best described by a two-term power function. The general form of the function is given by

$$\frac{p'}{p'_O} = a + b\left(\frac{V_S}{V_{S_O}}\right)^C \tag{4-4}$$

where, *a*, *b*, and c are parameters describing sediment material properties and initial conditions. Specifically, the a-factor is the intercept and reflects the initial state conditions of the V_S - p' relationship. The b-factor is a scaling factor and serves to shorten or expand the function in response to changes in the normalized shear wave velocity. This function gives an indication of the range of shear wave velocities during the shear process. The c-factor reflects the rate of increase for the shear wave velocity in responses to shear, for a given sediment. To some degree, a material dependency is implied for both the b-factor and c-factor. However, as will be detailed in later sections herein, the influence of the initial state conditions on these two factors is significantly greater than the influence of sediment type. Thus, the material dependency of these factors is uncertain. Table 4-2 lists the three fitting factors (a, b, and c) for all eight samples used in the study. The factors were obtained by performing regression analyses of the measured data recorded during the loading process (i.e. from the beginning of shear to the peak stress conditions).

Table 4-2 fitting factors, a, b, and c for the eighth Samples.

Sample #	a	b	c
#1	0.368	0.637	27.74
#2	0.434	0.553	91.51
#3	0.330	0.650	71.50
#4	0.364	0.631	21.05
#5	0.28	0.72	8.55
#6	0.053	0.950	5.28
#7	0.287	0.676	16.33
#8	0.033	0.964	5.82

4.7 DEVELOPMENT OF A SHEAR WAVE-BASED CONSTITUTIVE MODEL

The proposed two-term power function was used to develop the shear wave-base constitutive model under the CSSM framework. For normally consolidated conditions, the mean effective preconsolidation pressure is equal to the current or initial mean effective stress (i.e. $p'_c = p'_o$). Thus, Equation 4 was directly substituted into Equation 4-1 and Equation 2, presenting the yield surfaces of Modified Cam Clay (MCC) and Original Cam Clay (OCC), respectively. These substitutions produced equations for the yield surface expressed in terms of shear wave velocity and scaled to the current stress state. The resulting equations for MCC and OCC are given as

$$q = \mathrm{M} \cdot p'_o \cdot \left(a + b\left(\frac{V_S}{V_{So}}\right)^c \right) \cdot \left(\left(\frac{1}{\left(a + b\left(\frac{V_S}{V_{So}}\right)^c \right)} \right)^{0.5} - 1 \right) \qquad \text{for MCC} \qquad (4\text{-}5)$$

$$q = \mathrm{M} \cdot p'_o \cdot \left(a + b\left(\frac{V_S}{V_{So}}\right)^c \right) \cdot \ln\left(a + b\left(\frac{V_S}{V_{So}}\right)^c \right) \qquad \text{for OCC} \qquad (4\text{-}6)$$

4.7.1 Volumetric and Shear Strain Components

Further derivation of the shear wave-based constitutive model include formulations for volumetric and shear strains. The strain response of the sediments beyond yield is highly nonlinear. Thus, the components of volumetric and shear strain must be evaluated incrementally. The incremental elastic volumetric strain ($\Delta\varepsilon_p^e$) is given by

$$\Delta\varepsilon_p^e = \frac{k}{1+e_o}\ln\left(\frac{p'_{prev}}{p'}\right) \qquad (4\text{-}7)$$

where p'_{prev} is the previous value of mean effective stress. Under undrained conditions, the elastic and plastic volumetric strains both change equally and the total volumetric change equals zero (i.e. $\Delta\varepsilon_p = \Delta\varepsilon_p^e + \Delta\varepsilon_p^p = 0$) . Accordingly, $\Delta\varepsilon_p^e = -\Delta\varepsilon_p^p$. After substituting

Equation 4-4 into Equation 4-7, $\Delta\varepsilon_p^e$ can be expressed in terms of V_S as, demonstrated in Equation 4-8,

$$\Delta\varepsilon_p^e = -\Delta\varepsilon_p^p = \frac{k}{1+e_o}\ln\left(\frac{\left(a+b\left(\frac{V_S}{V_{So}}\right)^c\right)_{prev}}{\left(a+b\left(\frac{V_S}{V_{So}}\right)^c\right)}\right) \tag{4-8}$$

Incremental the elastic and plastic deviatoric (i.e. shear) strain components were derived in a similar manner, as were the volumetric strain components. Given the elastic shear modulus is given as $G = \rho \cdot V_S{}^2$, where ρ is the mass density of the material, the increment of the elastic shear component, $\Delta\varepsilon_q^e$, is calculated directly from the measured shear wave velocity shown in Equation 4-9

$$\Delta\varepsilon_q^e = \frac{\Delta q}{3G} = \frac{\Delta q}{3\left(\rho \cdot V_{So}^2\right)} \tag{4-9}$$

Note that the shear wave velocity used in Equation 4-9 assumes the *G* remains constant. This assumption is an idealization that the variation of the elastic shear strain is linear throughout the shearing process. Although this idealization is not strictly correct, it was adequate for the development of this framework.

For the plastic shear strain, Equation 4-10 is utilized to determine the incremental component ($\Delta\varepsilon_q^p$),

$$\Delta\varepsilon_q^p = \Delta\varepsilon_p^p \cdot \frac{q}{\mathrm{M}^2\left(p' - p_c'/2\right)} \tag{4-10}$$

Consequently, incremental plastic shear strain is written in terms of shear wave velocity by substituting Equation 4-4 into Equation 4-10. This equation is expressed as

$$\Delta\varepsilon_q^p = \Delta\varepsilon_p^p \cdot \frac{q}{\mathrm{M}^2 p_o' \left[\left(a + b\left(\frac{V_S}{V_{So}}\right)^c \right) - \left(\frac{1}{2}\right) \right]} \tag{4-11}$$

4.7.2 The Measured and Predicted Shear Behavior

Equations 4-5 through 4-11 form the framework of a shear wave-based constitutive model. To validate the efficacy of the framework, arbitrary values of V_S/V_{So} were input into the aforementioned equations to obtain predictions of p'/p_o'. Estimations of p' were obtained by multiplying the predicted values by the preconsolidation stress (i.e. $p_c' = p_o' =$ 344.5 kPa). For Equations 4-5 through 4-11, direct measures of the a-factor, b-factor, c-factor, and of the CSSM parameters (i.e. e_o, e_Γ, κ, λ, ϕ_{cs}') were utilized. Table 4-3 presents a summary of the CSSM parameters for all the sediment samples. In addition to the CSSM parameters, Table 4-3 also includes experimental measures of the α_s parameter. This parameter was presented by Muttashar et al., (2018) and is used to describe the relation between shear wave velocity and sediment behavior during isotropic consolidation. The α_s is an experimental parameter that represents shear-wave velocity of a deposit at mean effective stress, p_o' = 1.0 kPa. This parameter was a found to be related to material structure and fabric for fine grain sediments. This parameter is used later in the current study to relate shear behavior to consolidation behavior. The reader is referred to Muttashar et al., (2018) for a detailed discussion of the parameter and the corresponding isotropic consolidation relation.

Table 4-3. Measured CSSM parameters for the sediment samples.

Sample #	e_o	e_Γ	κ	λ	ϕ'_{cs} (deg)	α_S
#1	0.81	1.20	0.0110	0.146	15.4	20.4
#2	0.94	1.41	0.0124	0.114	14.9	27.8
#3	0.55	0.82	0.0059	0.080	17.34	31.7
#4	0.70	1.10	0.0096	0.094	15.38	34.0
#5	0.56	0.79	0.0051	0.050	15.19	62.5
#6	0.22	0.32	0.0025	0.028	21.48	60.8
#7	0.67	1.01	0.0051	0.078	18.22	34.3
#8	0.32	0.48	0.0038	0.044	17.18	61.8

Figures 4-5 presents the measured and predicted shear behavior of selected sediment samples in $q - p'$ space and in terms of V_S / V_{So}. The OCC model was used for the selected samples. It was observed that the clay-predominant sediment samples were better matched with the OCC model, while the silt-predominant sediment samples were better matched with the MCC model. In general, the logarithmic spiral yield surface of the OCC model produces a lower initial stiffness response for normally consolidated remolded samples than the ellipse yield surface of the MCC model. Consequently, the OCC predicted stress path tended to agree with the lower initial stiffness response observed for high plasticity clay sediments ($LL > 50$ and CF/SF ≥ 1.0). Conversely, the stress path predicted by MCC agreed with the higher initial stiffness response for the remolded samples with less plasticity (or having CF/SF < 1.0).

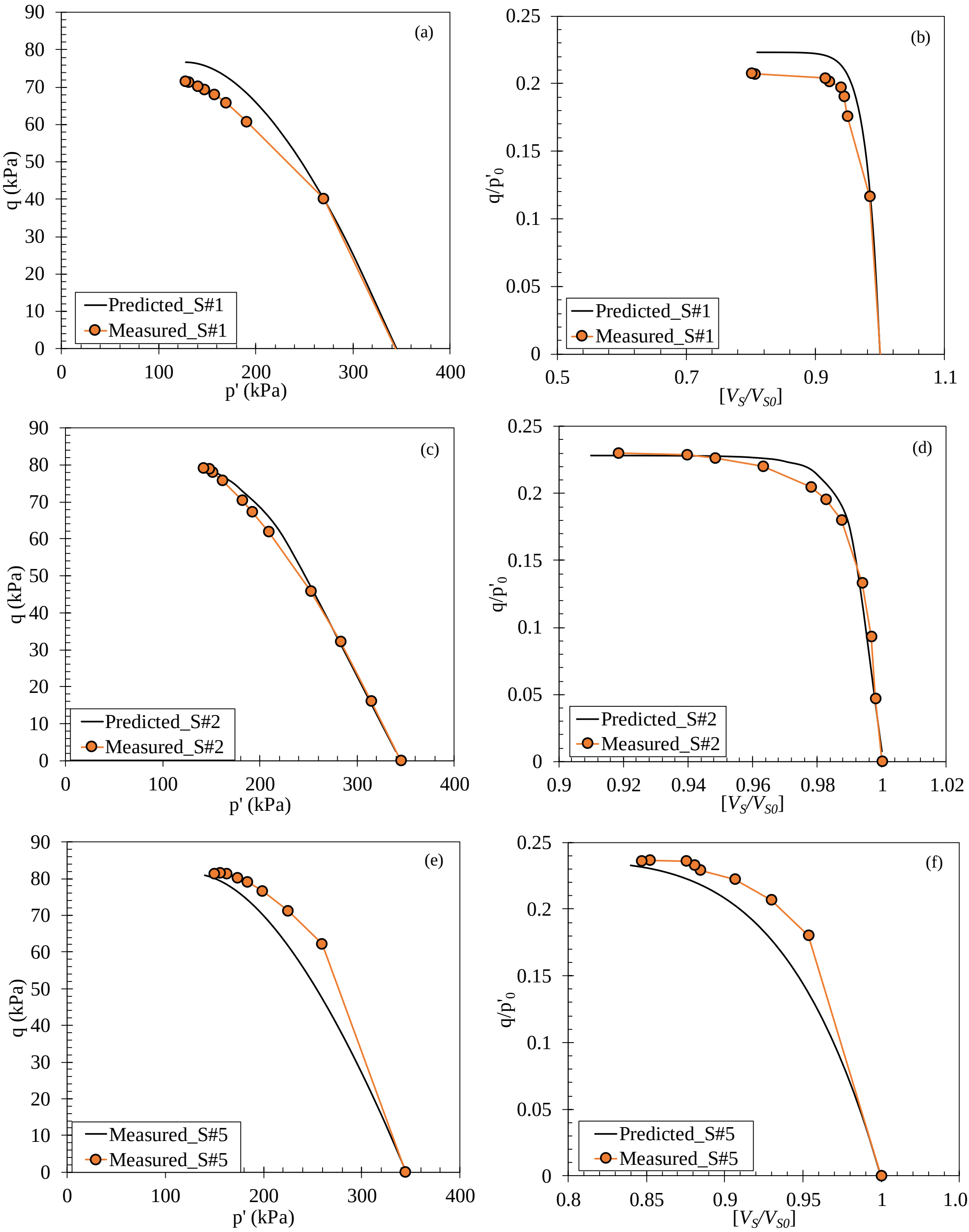

Figure 4-5. Typical measured and computed data of shear behavior and deformation of three samples (#1, #2, and #11).

Figure 4-5 shows there was a good match between the measured and predicted stress path data. The variations between the predicted and measured data are related to the inherent limitations of the base CSSM constitutive models per se and not related to the proposed two-term power function. It is anticipated that formulating a more advanced CSSM-based model using the proposed two-term power function would produce a better match between the measured and predicted data. However, the intent of this study was to show the viability of using elastic shear wave velocities to predict undrained shear behavior. Figure 4-5 also shows plotting the shear stress data as a function of V_S / V_{So} in essence scales the data and allows for hardening and peak behavior to be better discerned. In particular, the average predicted deviator stress at peak for the sediment samples was approximately $0.23 p_o'$.

For compression loading of normally consolidated sediments, the normalized shear wave velocities decrease from unity to the value corresponding to the peak stress. This decrease was found to be inversely proportional to the change in axial strain. Thus, the variable ($1 - V_s / V_{So}$) was found to be a reasonable proxy of the axial strain (ε). Figure 4-6 shows the deviator stress and the porewater pressure response plotted as functions of ($1 - V_s / V_{So}$). The predicted porewater pressure response was calculated assuming isotropic compression of a saturated elastic-perfectly plastic material in $q - p'$ space such that $u = p - p' = \left(p_o' + q/3 \right) - p'$, where p' is estimated from Equation 4-4 and q is obtained from the either Equation 4-5 or Equation 4-6. Figure 4-6 shows the predicted equivalent of the shear stress-strain curve matches the directly measured data well, at least within the performance limitations of the OCC and MCC models. The predicted porewater response matched the measured porewater pressure response up to peak conditions exceedingly well.

Again, the performance of the proposed two-term power function (i.e. Equation 4-4) appears to be solely limited to ability of the CSSM-based model to predict soil behavior. However, the caveat is that in its current form the proposed two-term power function assumes the shear wave velocity is highest at the end of consolidation and will decrease until peak stress conditions. The implication is that Equation 4-4 is only valid for normally consolidated, undrained loading conditions. Although this is a recognized limitation, the established framework of utilizing shear wave velocities to predict undrained loading behavior is valid.

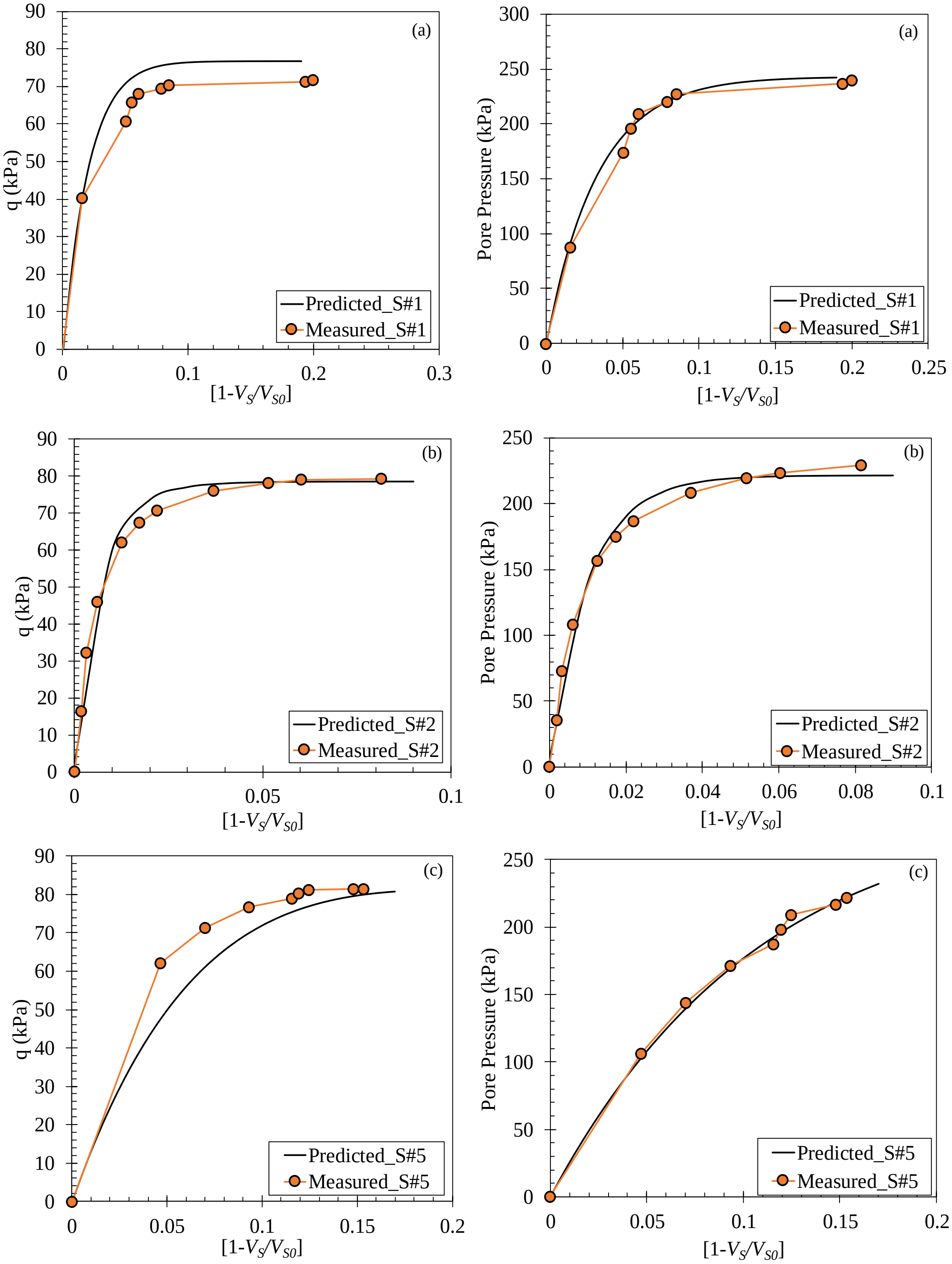

Figure 4-6 Typical measured and computed data for shear and porewater pressure behavior of three samples (#1, #2, and #5) during triaxial testing under undrained conditions.

4.8 RELIABLE CORRELATIONS OF MODEL INPUT PARAMETERS

Further efforts were undertaken to make the methodology presented in this study more accessible to the practitioner. The emphasis was to develop reliable empirical correlations for the model input parameters that require only basic index tests.

4.8.1 Critical State Friction Angle Parameter

The critical state friction angle, ϕ'_{CS} for the sediments samples ranged between 14.4 deg and 21 deg, with an average of 17.7 deg. Figure 4-7 shows the influence of CF/SF values on ϕ'_{CS} for the sample groups, categorized based on percent Fines. In the figure, ϕ'_{CS} decreases as the CF/SF ratio increases, irrespective of the percent Fines group.

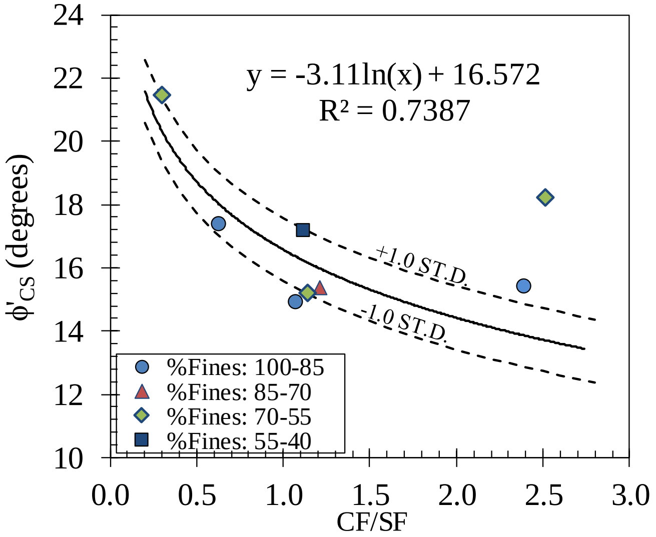

Figure 4-7. Influence of CF/SF ratio on critical-state friction angle, ϕ_{CS} .

Figure 4-7 shows there was some scatter in the data with the amount of scatter increasing with increasing CF/SF ratio. This increasing scatter was due to the materials transitioning from silt-predominant to clay-predominant. For silt-predominant samples, the materials behaved as semi-granular soils. The shear behavior was primarily governed by the particle-to-particle contact and was influenced by particle size, packing density, and confinement. The particle size was no longer the primary influence on ϕ'_{CS} for clay-predominant samples. As the samples transitioned to more clay-like, the influence of plasticity of the clay minerals increased. The shear behavior was then primarily governed by the cohesion forces between the particles (Bryson et al. 2017). Equation 4-12 expresses the relation between ϕ'_{CS} and CF/SF as a logarithmic function.

$$\phi'_{CS} = 16.572 - 3.11 \ln\left(\frac{CF}{SF}\right) \tag{4-12}$$

Because of the inherent scatter in the data used to develop Equation 4-12, the overall correlation is moderate (R^2= 0.74). However, the data appear to fit generally within ± 1.0 standard deviations of the trend. Consequently, Equation 4-12 is adequate for estimating the ϕ'_{CS} in the absence of laboratory data.

4.8.2 Consolidation Indices Input Model Parameters

The required consolidation indices for the OCC and the MCC models are λ and κ. Table 3 presented the consolidation parameters measured during the isotropic consolidation stage of the triaxial testing and Table 4-1 presented the index properties for the sediment samples. In comparing the measured parameters with the index properties, it was observed that the percent Fines, CF/SF ratio and the LL significantly trended with the consolidation indices. Samples with high percentages of fines and clay fraction tended to have high λ and κ values. Also, the α_s parameter is a stress-dependent state property that quantifies the variation of the shear-wave velocity as a function of the change in mean effective stress. A low value of the α_s parameter corresponds to a high variation of the shear-wave velocity with change in the mean effective stress change. The parameter was found to strongly reflect material type (as characterized by the consistency limits) and grain size of fine-grained sediments (as characterized by the percent Fines). Figure 8 shows λ and κ plotted as a function of α_s normalized by LL. Although the data were grouped according to the percent Fines, λ and κ are inherently material properties and thus primarily vary according to negative exponential functions of $\left(\alpha_s / LL\right)$, with R^2 = 0.92 and 0.89, respectively. Equations 4-13 and 4-14 express the empirical correlations used to determine the compression indices, λ and κ, respectively.

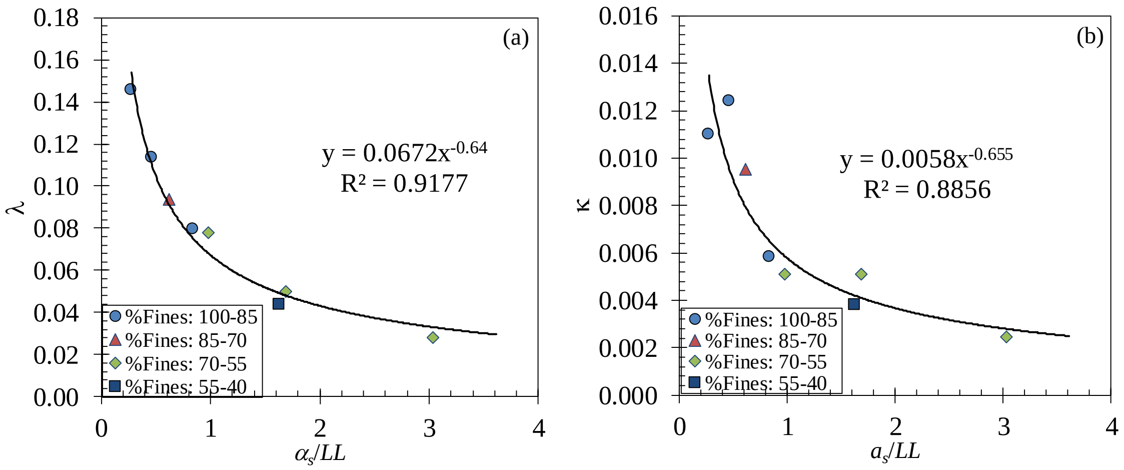

Figure 4-8. Consolidation indices as fuctions of material properties; (a) λ parameter and (b) κ parameter.

$$\lambda = 0.0672\left(\frac{\alpha_s}{LL}\right)^{-0.646} \tag{4-13}$$

$$\kappa = 0.0058\left(\frac{\alpha_s}{LL}\right)^{-0.665} \tag{4-14}$$

Traditionally, the λ and κ parameters are observed to be proportional to one another. This is evident for the sediment samples in that Equations 4-13 and 4-14 have similar exponent values (i.e. -0.646 compared to -0.66) and is offset by approximately 10 percent. Thus, the scaling factor of Equation 4-14 (noted as A_κ) can be given as 10 percent of the scaling factor of Equation 4-13 (noted as A_λ) so that $A_\kappa = 0.1A_\lambda$. The exponents for both equations can be given by an average value noted as $B_{\lambda\kappa}$ = 0.652. The relations can then be rewritten as

$$\lambda = A_\lambda\left(\frac{\alpha_s}{LL}\right)^{-B_{\lambda\kappa}} \tag{4-15}$$

$$\kappa = 0.1A_\lambda\left(\frac{\alpha_s}{LL}\right)^{-B_{\lambda\kappa}} \tag{4-16}$$

4.8.3 The Empirical Correlations for the a, b, and c Fitting Factors

The a-factor and the b-factor appears to describe different aspects of the initial state condition. Consequently, these factors were determined to be strongly correlated to the initial void ratio, as shown in Figure 4-9. An increase in the initial void ratio leads to an increase in the a-factor while leading to an inversely proportional decrease in the b-factor. These factors are most likely linked to the particle packing and the nature of contact stress under initial conditions.

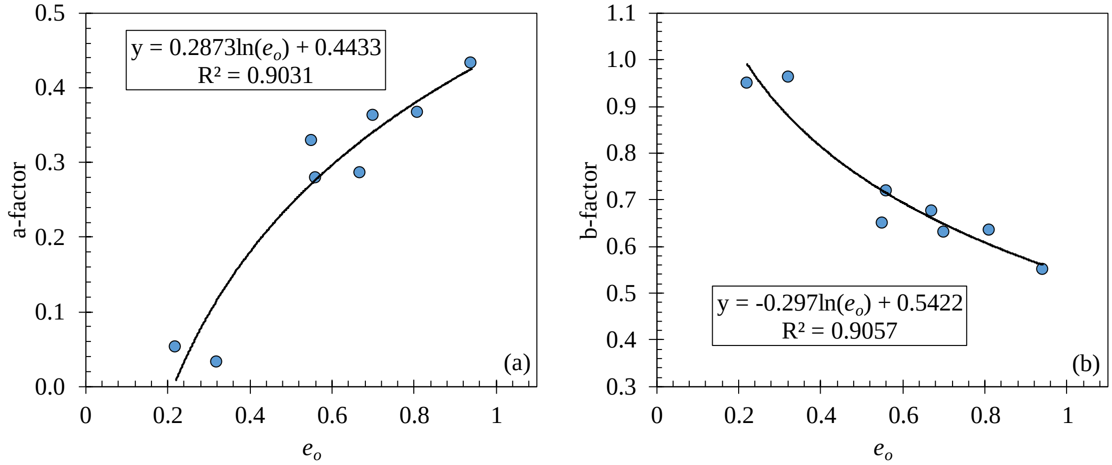

Figure 4-9. Variation of the a-factor and b-factor with void ratio: (a) a-factor variations and (b) b-factor variations.

Figure 4-9 shows the two fitting factors as functions of e_o. The figure shows a natural logarithmic function best describes the relation. The general form of the function is given as

$$a, b = I_{a,b} \pm M_{a,b} \ln\left(e_o\right) \tag{4-17}$$

Where $I_a = 0.4433$, $I_b = 0.5422$, $M_a = 0.2873$, $M_a = 0.297$. Using a similar simplification techniques as was used for the consolidation indices, the similar slopes values allows the average to be used in lieu of slopes for a and b. This slope average, noted as M_{av}, is estimated as 0.2922. The intercepts of the a-factor and b-factor equations were adjusted for the average slope value using a least squares optimization process of the measured and predicted data. It was observed that the optimized intercept of b-factor (noted as I_b) approximately equaled one minus the optimized intercept of the a-factor (noted as I_a), e.g., $I_b = 1 - I_a$. Thus, the new forms of the a-factor and b-factor relations can be written as shown in Equations 17 and 18.

$$a = I_a + M_{av} \ln\left(e_o\right) \tag{4-18}$$

$$b = \left(1 - I_a\right) - M_{av} \ln\left(e_o\right) \tag{4-19}$$

The c-factor is an exponent controlling the degree of curvature of the two-term power function. This factor characterizes the rate of the change in shear wave velocity with respect to the change in mean effective stress. Thus, this factor was assumed to reflect some aspect related to the fabric changes (or particle rearrangement) during loading. The c-factor generally trends with the percent Fines (i.e. an increasing c-factor somewhat correlates to an increasing percent Fines). However, correlations to material properties were inconclusive given the strong dependence of the stress-strain behavior on initial conditions for undrained loading. As a result of the dependence on initial conditions, the c-factor was also observed to be correlated to the initial void ratio. Figure 4-10 shows the relation between the c-factor and the void ratio. The relation is given by an exponential function as

$$c = 1.723 \cdot \exp\left(3.657 \cdot e_o\right) \tag{4-20}$$

Figure 4-10 shows that one data point did not fit the exponential trend. Given the inherent uncertainty associated with the regression analysis to obtain the a-, b-, and c-factors, and the behavior of the remaining data, this data point was assumed to be a possible outlier. This data point was not included in the development of Equation 4-20.

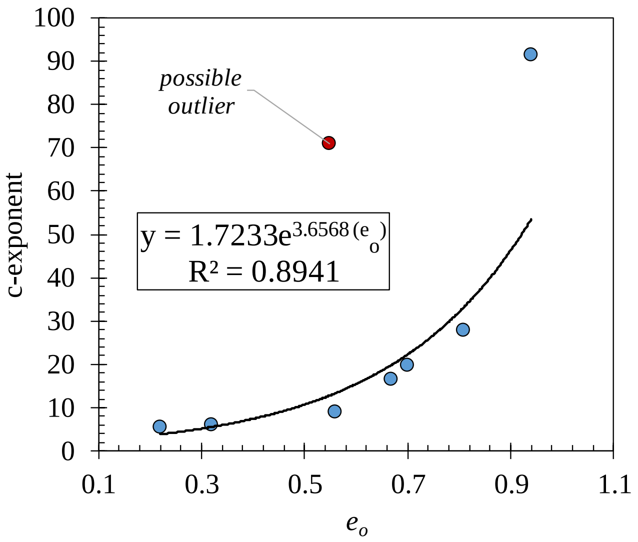

Figure 4-10. Variation of the c- factor with the void ratio.

A reliable empirical approximation of the normalized mean effective stress was obtained by substituting the Equations 4-18, 4-19, and 4-20 into Equation 4-4, the two-term power function is written as

$$\frac{p'}{p'_o}=\left[I_a+M_{av}\ln\left(e_o\right)\right]+\left[\left(1-I_a\right)-M_{av}\ln\left(e_o\right)\left(\frac{V_S}{V_{So}}\right)^{1.72\exp\left(3.657\cdot e_o\right)}\right] \tag{4-21}$$

Rearranging the terms and simplifying produces

$$\frac{p'}{p'_o}=1+0.292\cdot\ln\left(e_o\right)\left[1-\left(\frac{V_S}{V_{So}}\right)^{1.72\cdot\exp\left(3.657\cdot e_o\right)}\right] \tag{4-22}$$

It is evident from Equation 4-22 that changes in normalized mean effective stress with respect to changes in normalized shear wave velocity are dependent on the initial state condition. This behavior is consistent with undrained loading conditions. Thus, Equations 4-12, 4-15, 4-16, 4-18, and 4-22 combined with a CSSM framework provide reasonable approximations of undrained loading behavior from the beginning to the peak of the shearing process. More importantly, these approximations are made from basic index properties, knowledge of the initial state (i.e. void ratio), and measurements of shear wave velocities.

4.8.4 *Performance of Empirical Approximation Used for Prediction*

The correlations presented by Equations 4-12, 4-15, 4-16, and 4-22 were derived using index properties describing particle size distribution (CF/SF), texture and structure (LL and α_s), initial state (e_o), and measurements of shear wave velocity. Integrating these correlations into the CSSM framework presented herein yields an empirical approximation of the prediction methodology that is very easy to implement. Figure 4-11 evaluates the performance of the empirical approximation for predicting shear behavior of Sample #2.

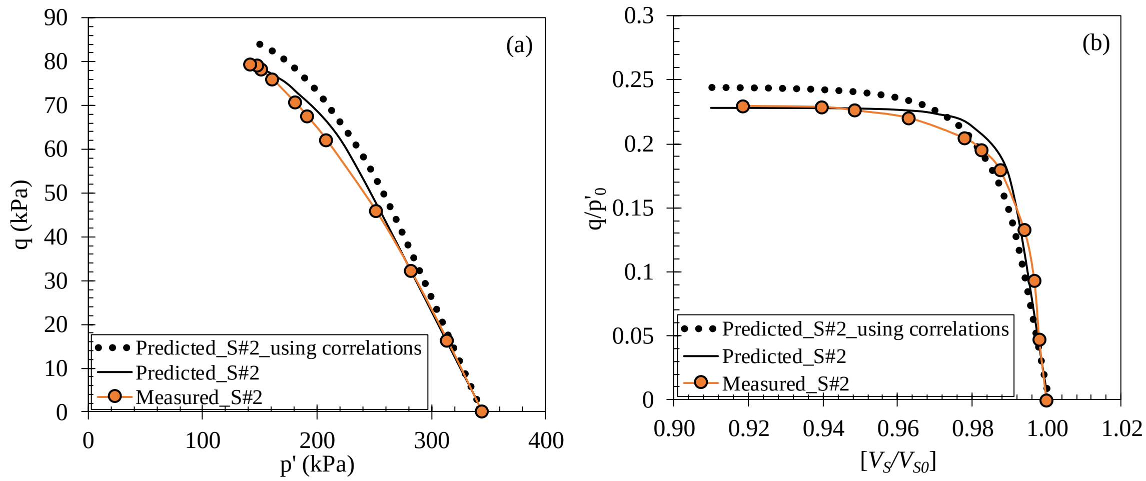

Figure 4-11 Predicted and measured shear behavior curves compared with the predicted curves with considerate the developed empirical correlations in this research.

As seen in the Figure 4-11, the proposed correlations provided a resonable prediction of the shear behavior by capturing both the effective stress path and the normalized shear data as functions of shear wave velocity. The descrepencies between the "predicted" data and the data "predicted using correlations" is due to the accuracy of the ϕ'_{CS} expression. The match between the predicted data was within 1 percent error when Equation 4-12 was used with -1.0 standard deviation.

4.9 APPLICATION OF CSSM FRAMEWORK TO FIELD DATA

The developed CSSM framework was applied to field data to evaluate the utility of the methodology for field applications. For the evaluation, field data were obtained from a site located near Isais Creek, south of San Francisco, California. The data were taken from a study investing the effects of pile installation on the static and dynamic properties of the

San Francisco Young Bay Mud (Hunt *et al*. 2000). The data included shear waves velocity measurements, material properties, and seismic cone penetrometer measurement with pore pressure (SCPT-U). The study evaluated site conditions prior to pile installation (noted as pre-pile) and at several intervals after installation (noted as post-pile). The study also included constant rate of strain (CRS) consolidation tests and consolidated undrained (CU) triaxial compression tests performed on undisturbed samples obtained pre-pile and post-pile installation. The reported laboratory test results were used to evaluate the methodology proposed herein.

The site profile consisted of a 4.3 m sandy fill layer overlying an approximately 11 m-layer of soft Young Bay Mud (YBM). The YBM was interfaced by 1.5 m stiff clayey sand layer at a depth of 15.3 m. The clayey sand layer was followed by a stiffer layer of YBM that extended to the bottom of the SCPT-U sounding. Groundwater was found at a depth of approximately 2 m.

Undisturbed samples were obtained from separate soil borings at depth of 8.5 m, 12.8 m, and 23.8 m. Laboratory index tests indicated that the YBM soils at the site were highly plastic clay (PI = 44 to 59) and were lightly overconsolidated (OCR approximately 1.2 to 1.4). The at-rest earth pressure coefficient (K_0) was estimated to be 0.62. For the in-situ shear wave velocity, measurements were obtained using the cross-hole seismic technique, specifically using OYO suspension logging method (Nighbor and Imai 1994).

For brevity, this study only considered data corresponding to the samples collected at the depth of 23.8 m. The consolidation input parameters required for the CSSM model (i.e. e_o , λ , κ) were obtained directly from the pre-pile and post-pile CRS data. In effort to have the predictions be somewhat objective, the critical state friction angle ϕ'_{CS} was estimated from the measured SCPT-U tip resistance (q_c). The q_c at a depth of 23.8 m was reported as 773 kPa. The ϕ'_{CS} was subsequently estimated using the relation suggested by Kulhawy and Mayne (1990), which is given as

$$\phi'_{CS} = \tan^{-1}\left(0.38 + 0.27 \cdot \log\left(\frac{q_c}{\sigma'_{v0}}\right)\right) \tag{4-23}$$

The vertical effective stress (σ'_{v0}) at 23.8 m was reported as 141.86 kPa. The a-, b-, and c-factors were estimated using the e_o values obtained from the CRS tests and Equations 4-18, 4-19, and 4-20. Table 4-4 shows the required initial and material parameters that were used for prediction. In the table, the intial mean effective stress was calculated as $p'_0 = \sigma'_{v0}\left(1+2K_0\right)/3$ and the preconsolidation stress was assumed to be $p'_c = 1.2p'_0$. The table also gives the initial pre-pile and post-pile shear wave velocities at the depth of interest.

The stress-strain behaviour was predicted using the MCC formulation of the CSSM-based approach (Equation 4-5). The MCC model is generally assumed to be more applicable to undisturbed field samples. Figure 4-12 shows the performance of the CSSM-based approach for the pre-pile and post-pile conditions, as compared to the triaxial data. The figure indicates that the estimated results well match the laboratory data. Variations between the predicted and measured data were attributed to the limitations of the MCC model and not the shear wave-based framework. Thus, the results presented in Figure 4-12 show that the full stress-strain curve for a lightly overconsolidated sample, under undrained loading can be reliably predicted using the shear wave velocity, data from basic consolidation tests, and a field-derived friction angle.

Table 4-4 Input parameters used for prediction in both conditions (pre-and post-pile installation).

Input parameters	Pre-Pile	Post-Pile
λ	0.280	0.280
κ	0.013	0.013
ϕ'_{cs} (deg)	30.1	33.4
e_o	1.71	1.53
p'_o (kPa)	141.9	141.9
p'_c (kPa)	170.2	170.2
a	0.600	0.568
b	0.400	0.432
c	895.49	463.66
V_{s0} (m/s)	140	145

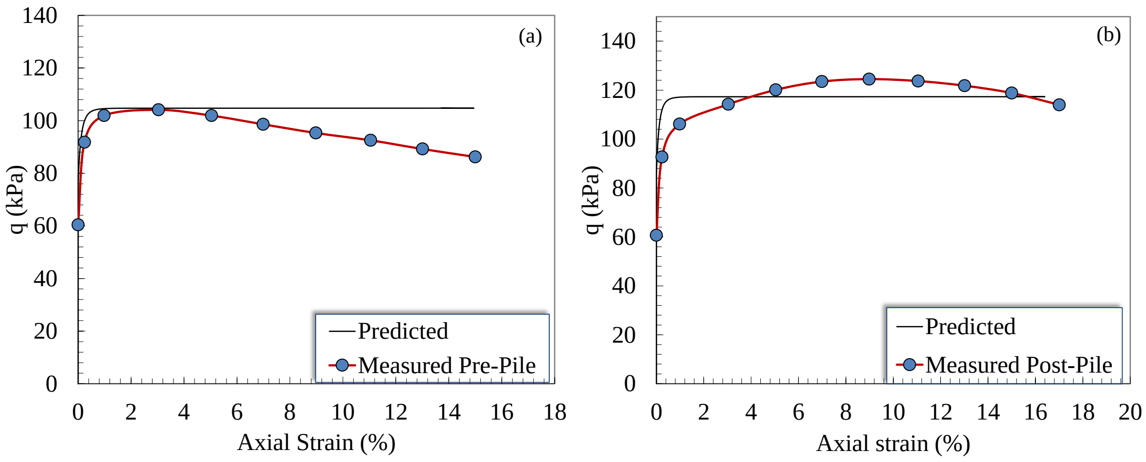

Figure 4-12 Performance of the proposed method in predicting deviatoric stress versus axial strain for samples taken at a depth of 23.8 m: (a) Pre-Pile predictions and (b) Post-Pile predictions.

4.10 CONCLUSION

The research predicted shear strain soil behavior and distribution of the critical stress paths in terms of shear-wave velocity. Accordingly, the study uses the critical state constitutive models to predict shear and pore pressure behavior as functions of shear wave velocity.

The elastic shear-wave velocity was measured using the bender elements techniques during a series of isotropically consolidated undrained triaxial (CIU) tests were conducted on a variety of fine-grained sediment samples. The finding was a new power-type form that determines normalized mean effective stress as a function of normalized shear wave velocity under undrained shear conditions. The three fitting factors of this power function were significantly related to the initial state properties of sediments, specifically the initial void ratio. By virtue of this new power-type relation, the critical state models, in specific original cam clay OCC and modified cam clay MCC were modified to estimate the shear strain behavior and stress paths in undrained conditions.

The reliability of the link between grain-size distribution characteristics and consistency limits were tested with the mechanical behavior of the sediment under the critical stress-state framework. Subsequently, correlations were developed using these initial basic properties, such as percent Fines, clay-to-silt fraction, initial void ratio, and liquid limit to

predict the input model parameters. The developed correlations can be broadly applied in different sediment types in which clay and silt sediments are the dominant deposits.

CHAPTER 5

Summary and Conclusions

This study proposed a new classification scheme to describe unconsolidated inorganic sediment that covers a wide range of unconsolidated fine-grained sediments, specifically in estuarine-riverine regions. The goal was to construct a plausible and practical scheme that identifies not only sediment texture but also its dominant mineralogy. This classification scheme is based on the linear relationship between percent silt (SF) and Fines, which was well identified. Regarding the sediment mineralogy, the activity of clay is used as the measurable factor related to the major clay-mineral groups. The plasticity that was mathematically estimated had two interfaces and three zones of low, intermediate, and high plasticity in the classification scheme. Because of combining plasticity and grain size characteristics, the scheme allows the sediment to be divided into more subdivisions and provides subclasses sediment units, specifically in fine-grained sediment units. The FS-Fines scheme is of essential significance to allow further detailed characterization of sediment units and then provides better resolution in classes boundaries.

Also, the study proposed a new_prediction (continuous function) simulates compression behavior $[e-\log(p')]$ of normally consolidated sediments. The prediction equation depends on the association between shear-wave velocity, mean effective stress, and void ratio. From this association, the experimental constants α_s and β_s were found to correlate well with the depositional factors, specifically percent Fines, silt percent, and LL. The α_s factor and β_s exponent are prominent enough to measure capacity of volumetric change of sediment and characterize the variety of the depositional environment. Complexity of depositional processes could be defined by grain-size distribution, liquid limits, and the stress history of sedimentary units. As a result, a better understanding of these depositional parameters can be attained by using α_s and β_s, which are practical factors, to quantify the change in consolidation behavior during the compression process.

In this dissertation, a shear wave-based constitutive model was presented that is able to predict the stress-strain behavior of a normally consolidated sediments, under undrained loading. Elastic shear-wave velocity under critical state framework was utilized to establish

a new power-type function that predict the shear strength behavior and critical stress paths of fine-grained sediments under undrained conditions. Also, the reliability of input model parameters and state and material properties of a variety of fine-grained sediments were developed, linked and correlated.

APPENDIX A

Selected Material Properties for Testing

A-1 Steps of Mixture Procedure

The three source soils selected for this research were obtained from Henderson County (H), Fayette County (F), and Lee County (L). A commercially available kaolin clay sample was included with the three natural soil (source) soils. The mixture procedure serves as a way to create fine-grained samples where Fines percent and CF/SF ratio are being governed. the procedure entails precalculation on the Grain Size distribution (GSD) curves of the source soils, as following:

1. Find GSD curve for each soil (source) that was selected.
2. Divide all percentages of the finer passing (%) that form the GSD source soil curve into 10, 20, 25, 30, 40, 50, 60, 70, 75, 80, and 90 percent in an Excel spreadsheet.
3. Design a specific GSD curve (new sample) by combing specific percentages of those divided percentages in the previous step.
4. Take the determined percentages, and then start experimentally to mix them. This mixture represents a new designed sample that has predicted GSD curve with the required particle sizes percentages.
5. Conduct the grain-size test for the designed sample (the mixture) to obtain measured GSD curve having the required grain size percentages.
6. Repeat steps 2- 5 for the other designed samples to generate the other new GSD curves.

In this study, five CF/SF ratios were generated at the same Fines percent. Then, this Fines percent was reduced by replacing with an addition of fine sand (<425μm). Adding the fine sand will change Fines percent yet the CF/SF will remain constant. In this way, the mixture procedure allows the CF/SF at a particular Fines percent to be controlled.

In addition, by adding the fine sand, the procedure allows the Fines percent at a particular CF/SF to be controlled.

A-2 Designed Grain Size Distribution Curves

The design sediment unit experimentally is simulation process developed in this study that mimic the entire GSD curve of the real sediment, specfically fine-grained sediment units, such as marsh and bay mud. this study simulated three types of GSD curves of sediment types from the literature, including the clayey silt of the marsh sediment unit (Muttashar 2005), the Rancho Solano silty clay of the bay mud sediment unit (Meehan 2006), and the fine sand of the natural levee unit (Kuecher 1994).

These particular environments were chosen to demonstrate the technique for various GSD curves. Table A-1 shows the different percentages of source soils used in each design.

Table A-1 Mixture percentages used to simulate different sediment units

Sediment Unit	Mixture
Clayey silt of marsh deposits	(50% K) + (25% H) + (25% L).
Silty clay bay mud deposits	(25 % of #1) + (75% #2), where 1# (60% F) + (40% K). 2# (60% H) + (40% F).
Fine sand of channel levee deposits	(0.55% of 0.25mm) + (0.85% of 0. 2mm) + (55.4% of 0.15mm) + (39.8% of 0.1) + (3.3% of 0.075mm).

K = kaolinite, H = Henderson County soil, L = Lee County soil, F = Fayette County soil.

This procedure for simulating sediment type provides a reliable means to control percent Fines (CF/SF ratio). In general, the procedure serves as a way to create soil samples with specific required material properties and create a sediment type that may be difficult to sample. Figure A-1 presents the three sediment units that were chosen from the literature with the source grain-size curves that were used for simulation. Figure A-2 shows the simulated curves of the three sediments units.

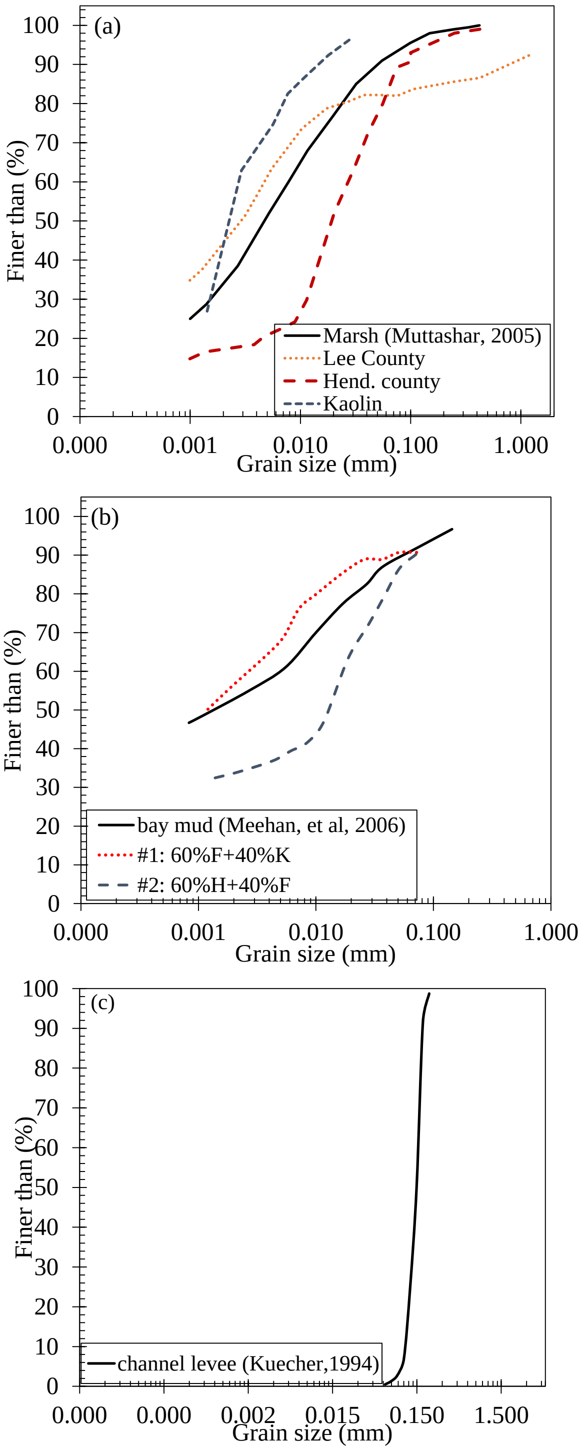

Figure A-1 Grain-size distribution curves for three types of sediment units and the associated source soils: (a) marsh deposits (clayey silt), (b) bay mud deposits (Rancho Solano silty clay), (c) channel levee deposits (fine sand).

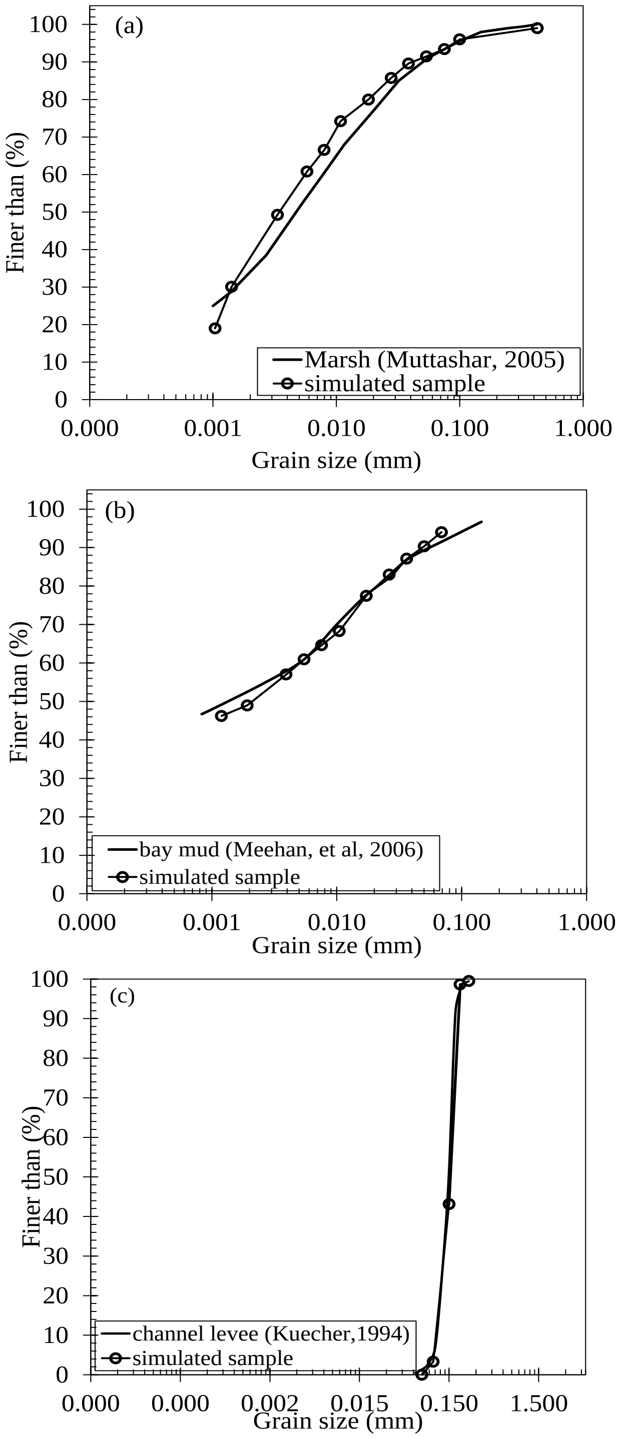

Figure A-2 Simulated curves for three types of sediment units and the associated source sediments: (a) marsh deposits (clayey silt), (b) bay mud deposits (Rancho Solano silty clay), and (c) channel levee deposits (fine sand).

Marsh sediment unit – The actual grain-size distribution curve of marsh sediments (Muttashar 2005) was simulated by mixing different percentages of the source samples.

The closest matching percentages were used to represent the designed curve. In this example, the optimal mix consisted of 25 percent of Lee County soil, 25 percent of Henderson County soil, and 50 percent of kaolin soil, as shown in Figures A-1a and A-2a.

Bay mud sediment unit – The simulated match for the bay mud sediments (Rancho Solano clay) (Meehan 2006) was more complicated to achieve than for the marsh sediments. In this case, blends were required to achieve the new GSD curves. This is shown in Figure S1b, where curves 1 and 2 are the new GSD blended curves, which in turn were mixed to simulate the bay mud sediment. The two new curves were blended as follows:

Curve 1: 60 percent Fayette County sample and 40 percent kaolin.

Curve 2: 60 percent Henderson County sample and 40 percent Fayette County sample.

The optimal design for the actual curve was determined by 25 percent of curve 1 and 75 percent of curve 2. The final designed curve is shown in Figures A-1b and A-2b.

Channel levee sediment unit – The GSD curve for the channel levee sediment (Figure A-1c) was easier to simulate than for fine-grained sediment. The simulated GSD was directly mixed using different grain-size percentages (Table S1) from the source samples (Figure A-2c).

The experimental mixing procedure facilitates the simulation of grain-size distribution curves. The procedure is useful for characterizing sediment types in areas that are remote or difficult to sample. However, the simulation procedure characterizes the particle-size distribution of sediment, and is not concerned with mineralogical composition. It might be this potential limitation does not matter much for coarse-grained sediments, but for simulation of fine-grained sediment units, such as marsh or bay mud, mineralogical components are very important. Designing of the entire GSD curve is the primary step that was achieved in this study that needs further studies to present the mineralogical composition of the designed GSD curve as well. The current study recommends using plasticity parameter as a useful proxy of the minerology of sediment.

Maybe the mineralogical components of bay mud differ in different places because of different depositional conditions throughout the world. This means that two samples having the same GSD characterization might have different mineralogical components (or different liquid limit values). The LL of bay mud of simulated Rancho Solano sediments (LL = 55 percent) is significantly less than the LL of bay mud in the Mississippi sediments, in which LL reaches more than 100 percent. As previously stated, the mineralogy of the sediment in the classification scheme (Figure 13) and LL limits (lines) were delineated based on the dominant clay minerals, even though this sediment unit has the same as the grain-size distribution curve. If this case, sediment unit having the same grain size distribution curve with different LL requires a mixture with a different type of materials. For example, simulation of a marsh sediment unit that has low to medium plasticity required a certain addition of kaolinite to the mixture, whereas simulating the same marsh sediments from a different place having very high LL might require adding montmorillonite (very high plasticity) instead. This results in two samples having the same GSD curve, but different LL values for each location. This simulation process is a simple, practical procedure that researchers could further refine in the future to be more precise and better simulate a certain sedimentary environment.

Table A-3 Data taken from Hathaway (1971) for verification the classification scheme.

Locations and descriptions of the grain-size data taken from (Hathaway 1971).

No.	Location			Fines (%)	CF/SF Ratio	SF (%)	Description According to Figure 9
	Latitude	Longitude	Name				
1	33.081	-76.4188	Slope	62.9	1.34	25.4	silty clayey Sand
2	26.25233	-86.2816	Gulf of Mexico	58.2	2.14	17.5	silty clayey Sand
3	29.02283	-90.376	Louisiana	61.0	0.11	51.6	clayey sandy Silt
4	29.01067	-90.4507	Louisiana	65.0	0.02	59.7	clayey sandy Silt
5	29.25267	-89.888	Louisiana	55.5	0.07	49.1	clayey sandy Silt
6	29.221	-89.5698	Louisiana	55.2	0.08	48.1	clayey sandy Silt
7	28.8785	-90.5677	Louisiana	60.0	0.17	48.5	clayey sandy Silt
8	28.861	-90.5417	Louisiana	65.1	0.19	51.6	clayey sandy Silt
9	43.195	-70.1417	Jeffrey's Basin	60.2	2.06	18.5	silty sandy Clay
10	43	-68.9833	Central Gulf of Maine	65.5	1.89	21.4	silty sandy Clay
11	19.384	-168.885	Pacific	66.1	1.07	30.0	silty sandy Clay

Table A-3 (continued)

12	29.05733	-90.3373	Louisiana	45.3	0.03	41.2	clay silty Sand
13	29.02334	-90.5655	Louisiana	50.6	0.06	44.7	clay silty Sand
14	29.04567	-90.465	Louisiana	15.1	0.07	13.3	clay silty Sand
15	29.23133	-89.542	Louisiana	20.2	0.10	17.2	clay silty Sand
16	28.9725	-90.8202	Louisiana	30.0	0.13	24.9	clay silty Sand
17	29.0445	-90.7462	Louisiana	30.3	0.14	25.1	clay silty Sand
18	29.2985	-89.8408	Louisiana	35.5	0.14	29.3	clay silty Sand
19	28.93867	-90.8755	Louisiana	35.1	0.18	28.0	clay silty Sand
20	29.06333	-90.5185	Louisiana	15.1	0.18	11.9	clay silty Sand
21	28.935	-90.9897	Louisiana	40.1	0.21	31.3	clay silty Sand
22	29.0405	-90.5678	Louisiana	50.4	0.26	37.7	clay silty Sand
23	29.1315	-90.003	Louisiana	44.9	0.28	33.1	clay silty Sand
24	28.90783	-90.5473	Louisiana	40.2	0.28	29.6	clay silty Sand
25	29.00983	-90.8587	Louisiana	25.9	0.35	18.1	clay silty Sand
26	29.19117	-89.5908	Louisiana	20.2	0.37	13.8	clay silty Sand
27	29.04267	-90.9353	Louisiana	25.4	0.44	16.6	clay silty Sand
28	42.51783	-70.475	Southeast of Cape Ann	63.0	0.80	32.9	clay silty Sand
29	29.0445	-90.7462	Louisiana	10.1	0.11	8.6	clayey silty Sand
30	29.0445	-90.7462	Louisiana	9.9	0.21	7.7	clayey silty Sand
31	29.03733	-90.3967	Louisiana	5.1	0.27	3.8	clayey silty Sand
32	29.0545	-90.3715	Louisiana	5.0	0.32	3.6	clayey silty Sand
33	29.04167	-90.75	Louisiana	1.0	0.50	0.6	clayey silty Sand
34	29.04167	-90.6733	Louisiana	1.0	0.47	0.6	Sand
35	18.46367	-65.7582	Puerto Rico	68.6	0.72	37.4	sandy clayey Silt
36	29.27883	-89.7047	Louisiana	70.6	0.09	61.2	sandy clayey Silt
37	29.19317	-89.5582	Louisiana	90.2	0.05	80.7	sandy clayey Silt
38	29.033	-90.5375	Louisiana	75.0	0.07	66.3	sandy clayey Silt
39	29.02433	-90.5345	Louisiana	95.1	0.09	82.0	sandy clayey Silt
40	29.098	-90.1072	Louisiana	80.5	0.10	69.2	sandy clayey Silt
41	28.97283	-90.3523	Louisiana	95.2	0.11	80.4	sandy clayey Silt

Table A-3 (continued)

42	28.97033	-90.9232	Louisiana	75.2	0.15	61.3	sandy clayey Silt
43	29.04533	-90.3358	Louisiana	90.2	0.17	72.7	sandy clayey Silt
44	28.98233	-90.813	Louisiana	80.1	0.18	63.8	sandy clayey Silt
45	40.658	-67.775	Lydonia Canyon	80.9	0.23	61.9	sandy clayey Silt
46	40.322	-68.12	Oceanographer Canyon	77.9	0.25	58.7	sandy clayey Silt
47	40.275	-67.6498	Lydonia Canyon	78.5	0.31	56.5	sandy clayey Silt
48	28.97017	-90.4353	Louisiana	85.0	0.54	52.0	sandy clayey Silt
49	29.20167	-89.517	Louisiana	85.2	0.56	51.3	sandy clayey Silt
50	29.031	-90.261	Louisiana	99.8	0.70	46.8	sandy clayey Silt
51	40.525	-67.714	Lydonia Canyon	75.0	0.74	40.7	sandy clayey Silt
52	43.33333	-70	Western Gulf of Maine	100.4	0.77	53.5	sandy clayey Silt
53	24.3	-80.65	Off Florida Keys	78.5	0.80	41.1	sandy clayey Silt
54	38.98667	-70.4883	SW Of Atlantis Canyon.	100.4	0.94	48.8	sandy clayey Silt
55	26.481	-85.084	Gulf of Mexico	73.9	2.94	17.6	sandy silty Clay
56	28.66	-89.821	Gulf of Mexico	68.6	1.22	29.1	sandy silty Clay
57	40.46	-67.667	Lydonia Canyon	82.4	1.03	38.2	sandy silty Clay
58	43.5	-69.25	Central Gulf of Maine	100.0	1.37	39.9	sandy silty Clay
59	42	-69.6833	South Gulf of Maine	100.4	1.55	37.0	sandy silty Clay
60	44.40133	-68.9447	N.Penobscot Bay Mud	100.1	1.60	36.3	sandy silty Clay
61	43.15	-70.2817	Jeffrey's Basin	76.9	1.79	25.9	sandy silty Clay
62	43.5	-69.75	Central Gulf of Maine	100.0	1.82	33.4	sandy silty Clay
63	19.353	-168.926	Other	75.4	1.85	24.9	sandy silty Clay
64	43.35	-69.7667	Central Gulf of Maine	100.0	1.93	32.3	sandy silty Clay
65	32.78167	-79.96	Ashley River,S.C.	77.0	2.10	23.3	sandy silty Clay
66	43.1	-70.25	Jeffrey's Basin	73.3	2.11	22.3	sandy silty Clay
67	42.475	-69.0417	Cashes Ledge	100.9	2.15	30.2	sandy silty Clay
68	42.33667	-69.0167	Gulf of Maine	100.1	2.43	27.5	sandy silty Clay
69	25.29633	-84.6735	Gulf of Mexico	77.0	2.68	19.7	sandy silty Clay
70	25.34383	-84.712	Gulf of Mexico	82.4	2.89	20.0	sandy silty Clay
71	42.33333	-69.75	North of Provincetown	100.0	3.40	21.6	sandy silty Clay

Table A-3 (continued)

72	42.57667	-69.5433	Wilkinson Basin	100.9	4.17	18.4	sandy silty Clay
73	25.29633	-84.6735	Gulf of Mexico	79.6	4.45	13.7	sandy silty Clay
74	25.29633	-84.6735	Gulf of Mexico	72.1	5.50	10.5	sandy silty Clay

Hathaway, J. C. (1971). Data file, Continental Margin Program, Atlantic Coast of the United States: vol. 2 sample collection and analytical data, Woods Hole Oceanographic Institution.

APPENDIX B

XRD Analysis of Selected Samples

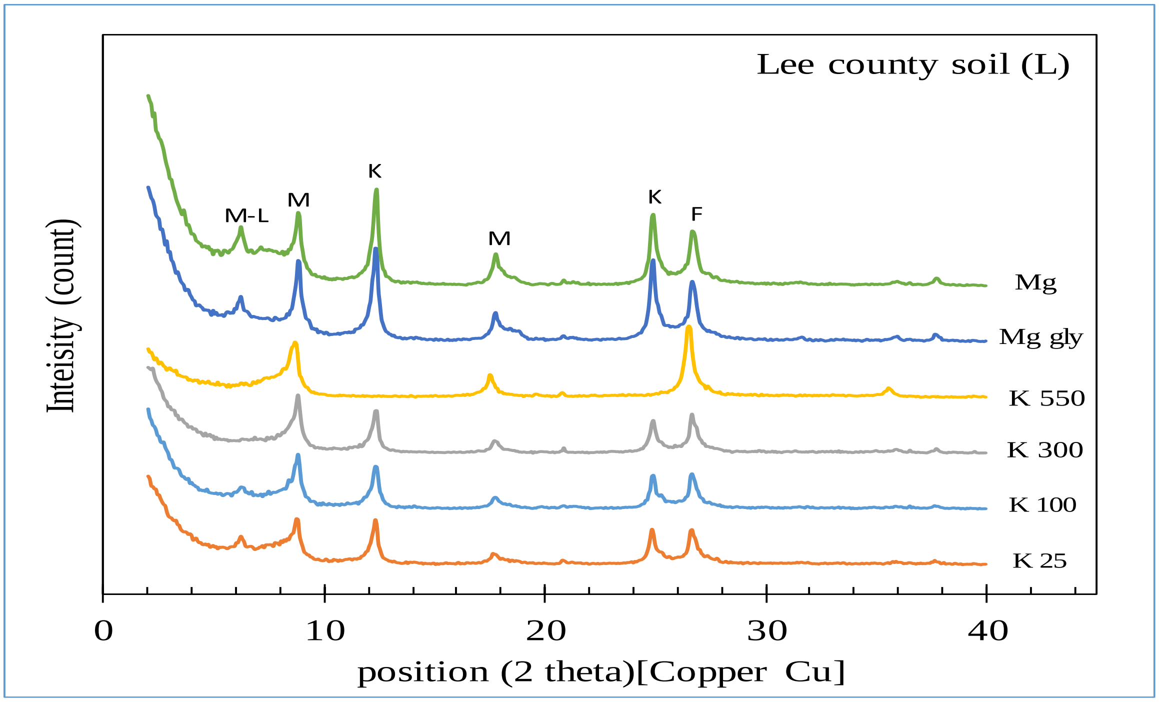
Lee county soil (L)
Inteisity (count)
M-L
M
K
M
K
F
Mg
Mg gly
K 550
K 300
K 100
K 25
0
10
20
30
40
position (2 theta)[Copper Cu]

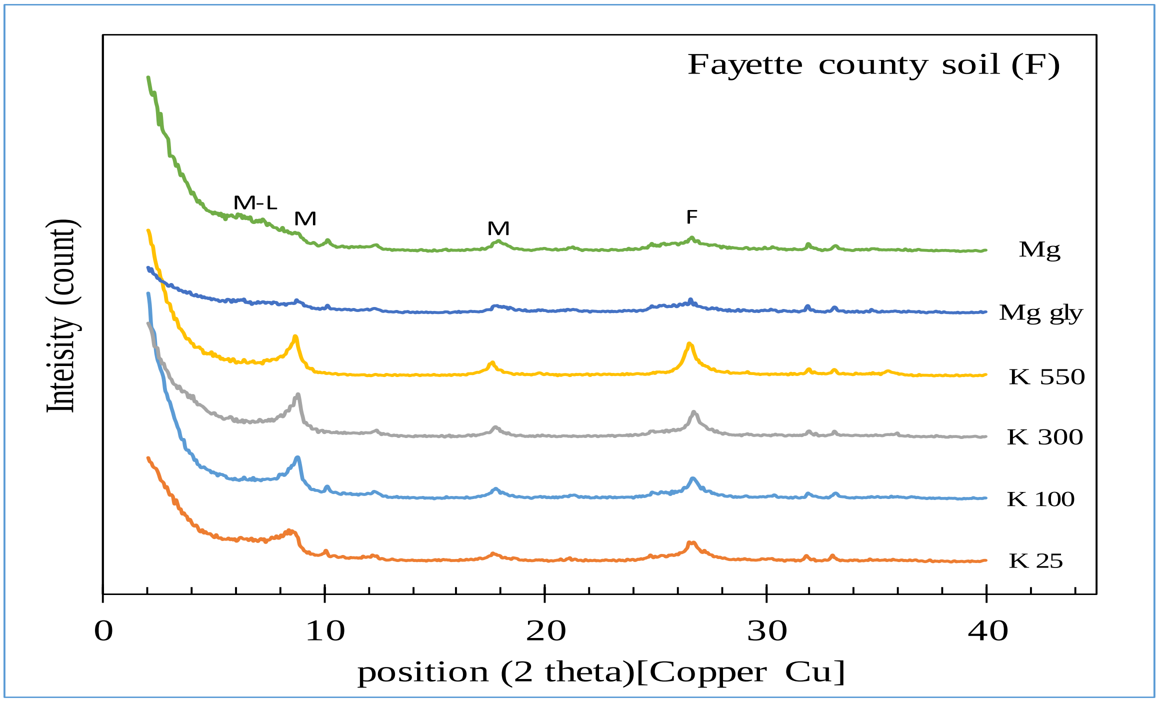
Fayette county soil (F)
Inteisity (count)
M-L
M
M
F
Mg
Mg gly
K 550
K 300
K 100
K 25
0
10
20
30
40
position (2 theta)[Copper Cu]

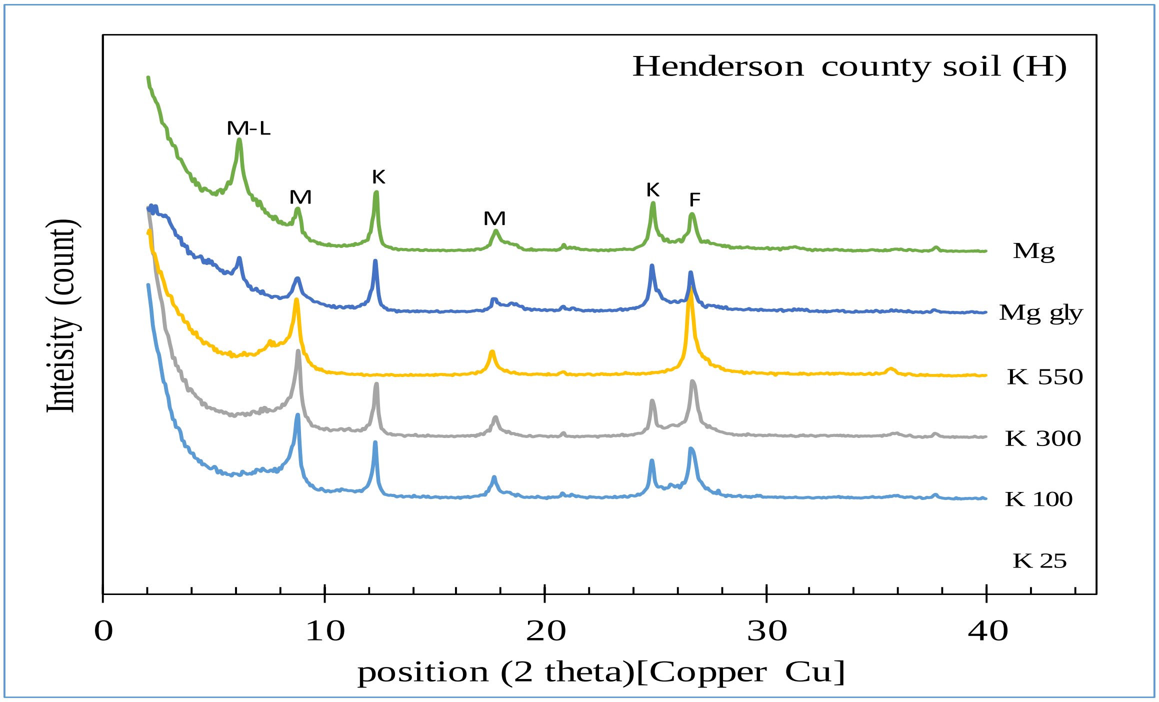
Henderson county soil (H)
M-L
M
K
M
K
F
Mg
Mg gly
K 550
K 300
K 100
K 25
Inteisity (count)
0
10
20
30
40
position (2 theta)[Copper Cu]

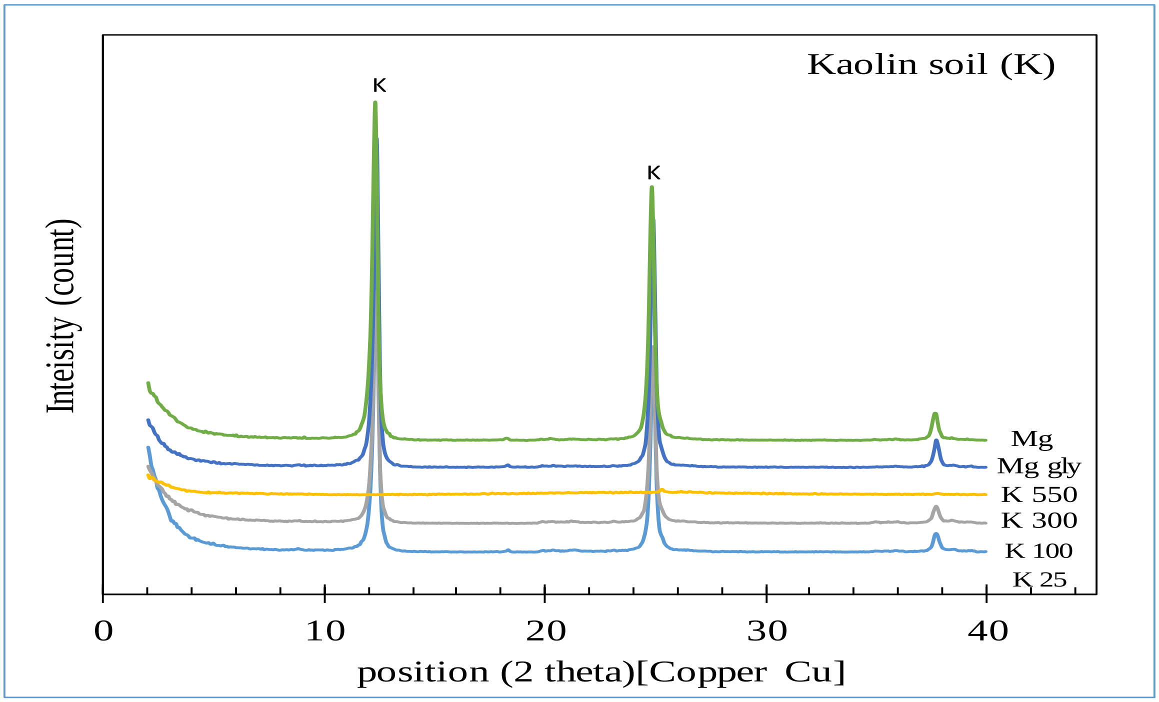
Kaolin soil (K)
K
K
Mg
Mg gly
K 550
K 300
K 100
K 25
Inteisity (count)
0
10
20
30
40
position (2 theta)[Copper Cu]

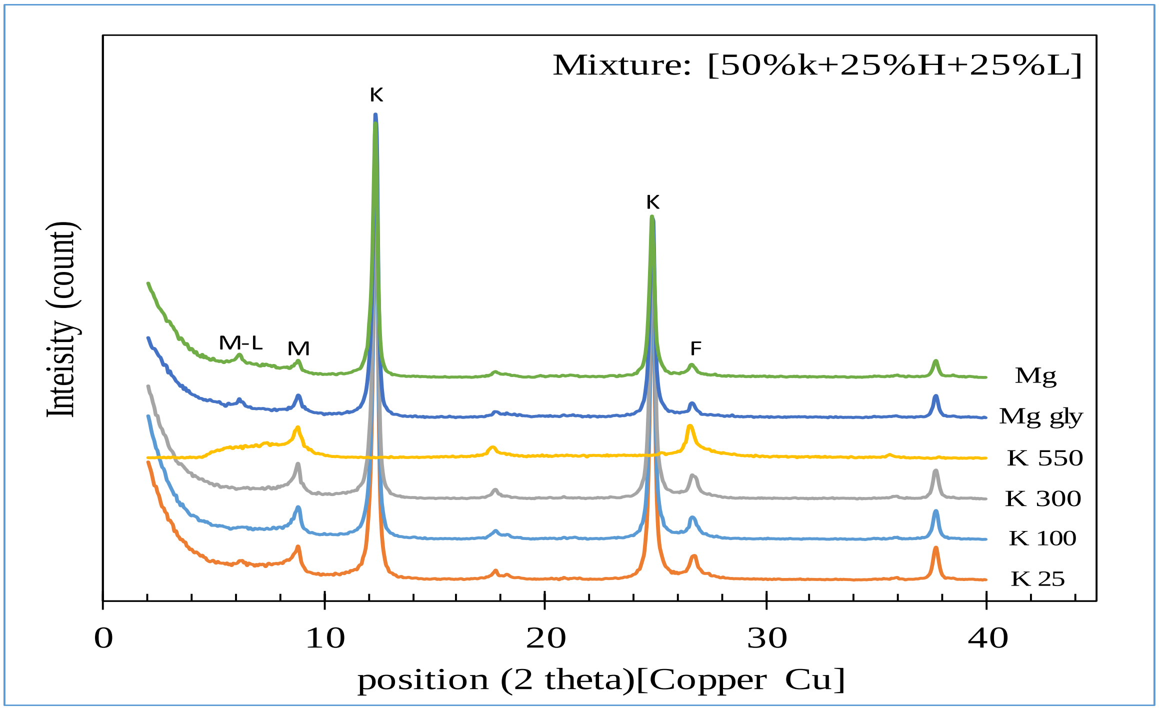
Mixture: [50%k+25%H+25%L]
K
K
M-L
M
F
Inteisity (count)
Mg
Mg gly
K 550
K 300
K 100
K 25
0
10
20
30
40
position (2 theta)[Copper Cu]

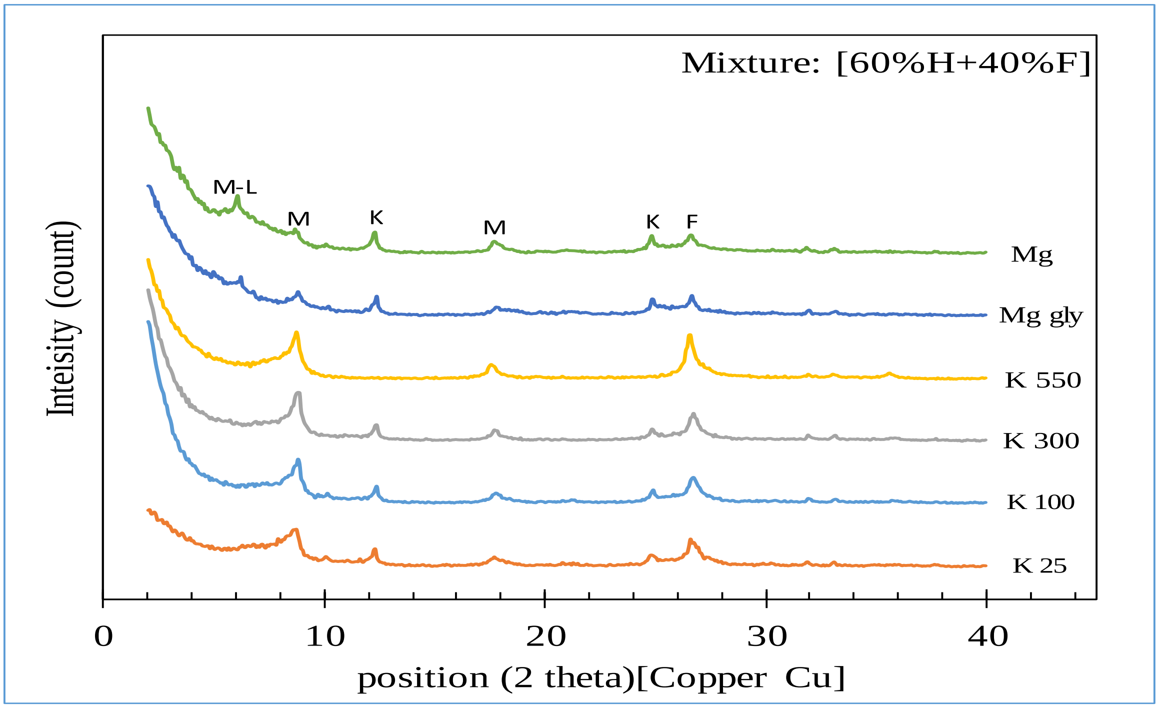
Mixture: [60%H+40%F]
M-L
M
K
M
K
F
Inteisity (count)
Mg
Mg gly
K 550
K 300
K 100
K 25
0
10
20
30
40
position (2 theta)[Copper Cu]

APPENDIX C

Rate of Displacement Method

C-1 Under-Controlled Resedimentation Method

Several procedures have been used to comprise the slurry and constitute a sample. As shown in Figure C-1a, the traditional process called a resedimentation technique has been more likely used to reconstitute the sample in certain conditions similar to those in situ, and it is useful to study the geotechnical behavior of soils (Germaine and Germaine 2009). This procedure uses weights added incrementally on the top of the sample. These weights are loaded manually. Recent research were used the same resedimentation process but with controlling loading automatically. Loads were added incrementally by using load frame machine and by controlling displacement rate in. The load frame equipment, as exhibited in Figure C-1b, is a multi-functions powerful unit that consists of a stepper motor and displacement sensor (GeoComp 2015). Once the mold is mounted on the load platen, setup the rate of displacement in control window. The load platen that carries the mold moves up, pushing the mold up toward touching with the fixed bar that has a vertical load sensor. This sensor records continuous exerted loads, which are corresponded at the same time to records of the displacement sensor. In this research, low and rapid rates of displacement were tested on the same sample. This means that the sample that has the same preparation conditions were subjected to two different rates of compaction (or displacement); Low and high displacement conditions. The low displacement rate (0.5 in/day) entails slow-incremented vertical loads, while the high displacement rate (1.75 in/ day) entails rapid-incremented vertical loads. Thus, the controlled vertical loads could simulate certain loading conditions of settled sediments in situ. For example, the low vertical loads on the sediment most likely simulates quiet depositional processes that indicate low hydrodynamic energy of sedimentation, such as marshes and tidal flat sediment units.

Controlling the rate of displacement, therefore, could be very useful for the fine-grained sediments that have convergent structure (grain size and mineralogy) with a different rate of depositional conditions. The different rate of the deposition (compaction) means different time periods that a fabric of the sediment unit needs to rearrange its particles as well as different amount of time is needed for liquids of sediment structure to dissipate. Simulation of the deposition rate experimentally provides a better understanding of the fine-grained sediments that are lithologically homogenous. It provides a better understanding of alterations in physical and mechanical properties of sedimentary environments during post-deposition processes. This research tested the sample with two different displacement rate conditions. High and low rate conditions were conducted on samples that had the same preparation conditions.

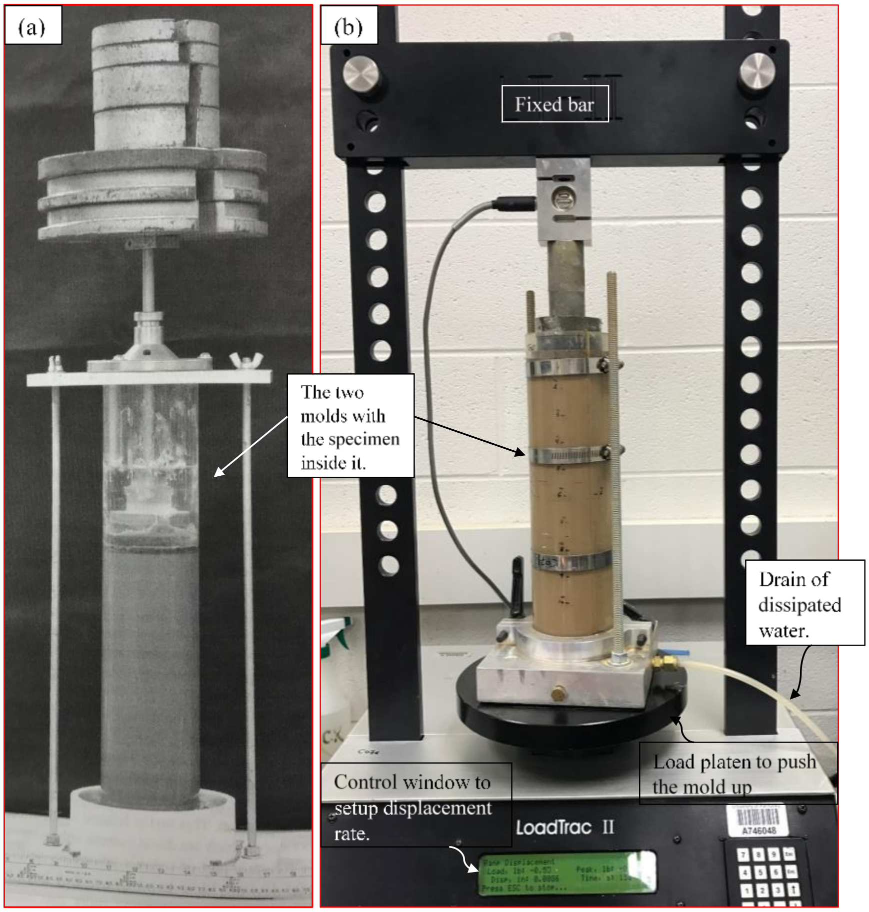

Figure C-1. The two methods of resedimentation, where (a) shows traditional method with using dead weight (Germaine and Germaine 2009) and (b) shows load frame with under-controlled displacement rate method that is utilized in this research.

The auto-controlled technique records final constant weight (effective stress) that the sample is subjected to at the required height. This procedure provides advantages that could serve studies of post-depositional conditions of sediments experimentally,

Maintaining the same density and water content which is evenly distributed in the sample.

Recording a constant load at the end of the loading process could characterize a maximum effective stress. This maximum overburden pressure is necessary to compare it with an actual stress that soil might be prone to in-situ.

Subjecting a particular sediment unit to different rates of displacement (deposition) provides a better understanding to study effects of the depositional loading rate on the structure of the sediment unit.

Further, studying pore pressures which are generated and trapped into pores of sediments when subject to rapid rate of deposition are improved. This water pressure issue could cause undrained conditions in the case of rapid deposition, which is a crucial geotechnical issue and should be taken into consideration when strength and compressibility parameters are evaluated.

The prepared sample was subjected to the both displacement rates (low and high rates) and was left under the loading till reaching a required height (6 in). Then, the sample was dismantled and measured its initial properties such as water content, density, and void ratio.

APPENDIX D

Triaxial Testing

Saturated triaxial testing was conducted for this research program. The triaxial cells were equipped with piezoelectric transducers to measure elastic shear wave velocities during testing. More details of the apparatus and testing procedures are presented in the following sections of this chapter.

D.1 Apparatus for Triaxial Testing

For this research, triaxial tests investigated the shearing and stiffness responses of the sediments under various states. The compressibility response of the sediments also investigated using the triaxial device, but supplemented using the constant rate of strain testing apparatus.

Figure D-1 shows the triaxial system for testing samples. This system was manufactured by GeoComp Corporation, headquartered in Acton, Massachusetts. It consists of three units connected and computerized by a controlling unit (computer). Loads are applied to the sample by the LoadTrac-II (loading unit). Confining and pore pressures are applied to the sample via the FlowTrac-II system, made by Trautwein Soil Testing Equipment, headquartered in Houston, Texas. Both of the Flow pumps have a pressure capacity of 1,400 kPa (200 psi). For the flow pump control pore pressure inside the specimens, the volume capacity was 750 ml, while Flow pump controlling cell pressure, the capacity was 250 ml.

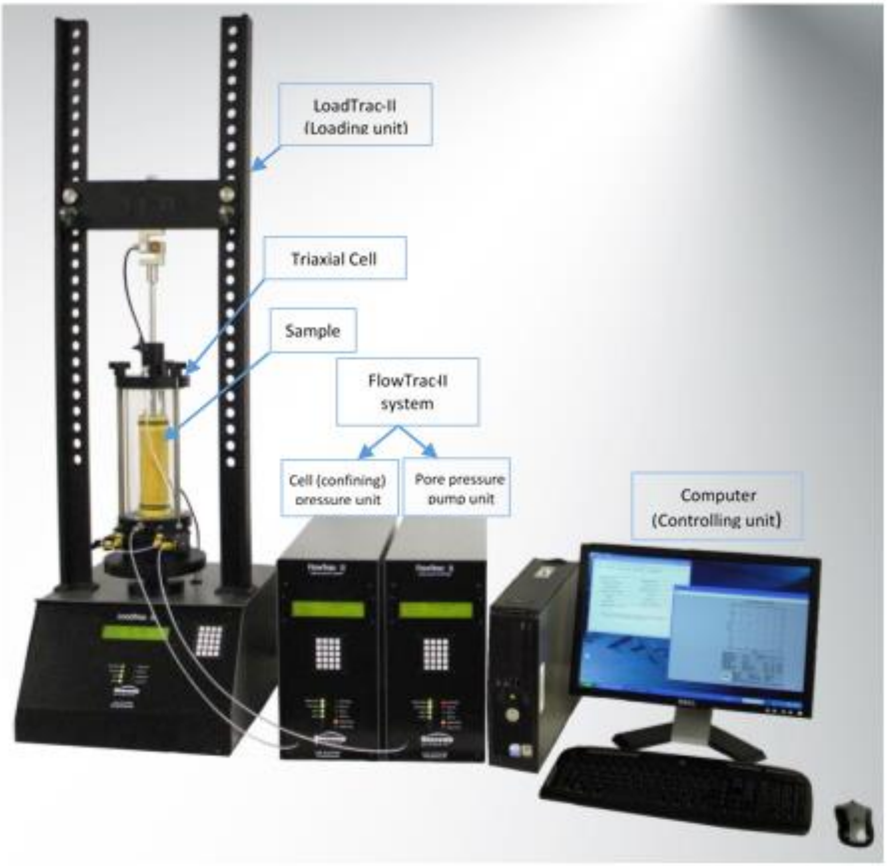

Figure D-1 LoadTrac-II/FlowTrac-II system of triaxial machine, after Geocomp Corp (2014).

Triaxial cell, the 101.6 mm (4 inches) diameter is designed for use with 71 mm (2.8 inches) diameter specimens, with an axial loading rod that extends through the top end cap. The triaxial cell's base and top platens were fitted with Bender elements that transmit and receive shear and compressional waves through the specimen. This technique uses two electro-mechanical transducers (transmitter and receiver elements), called Bender elements to generate and receive elastic waves. These two elements, Figure (17), are inserted in the top and base of the triaxial cell.

For full automation, test control and data acquisition, the triaxial system was networked with a computer that ran the Geocomp Triaxial software.

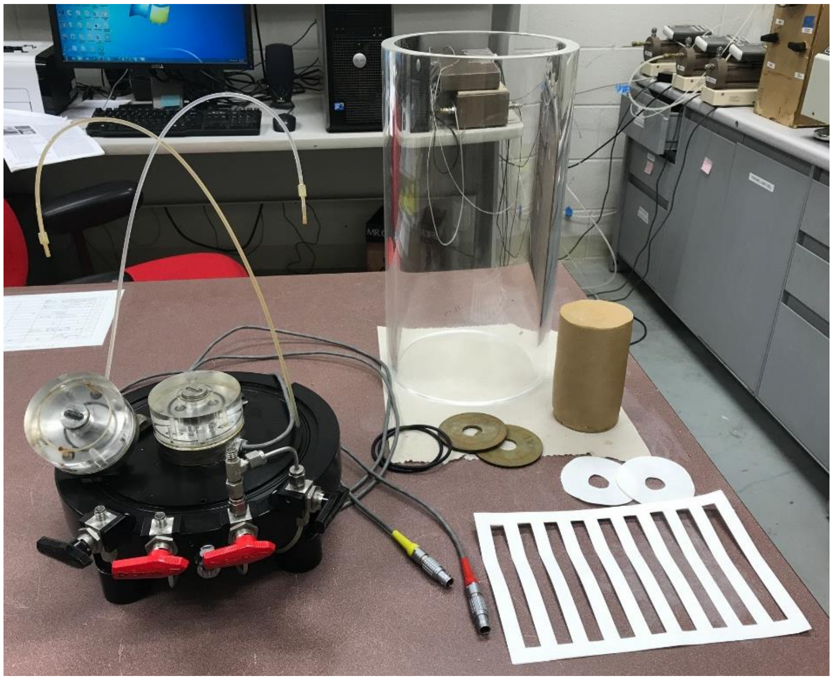

Figure D-2 triaxial cell parts and materials used to mounted the spciemen in the cell.

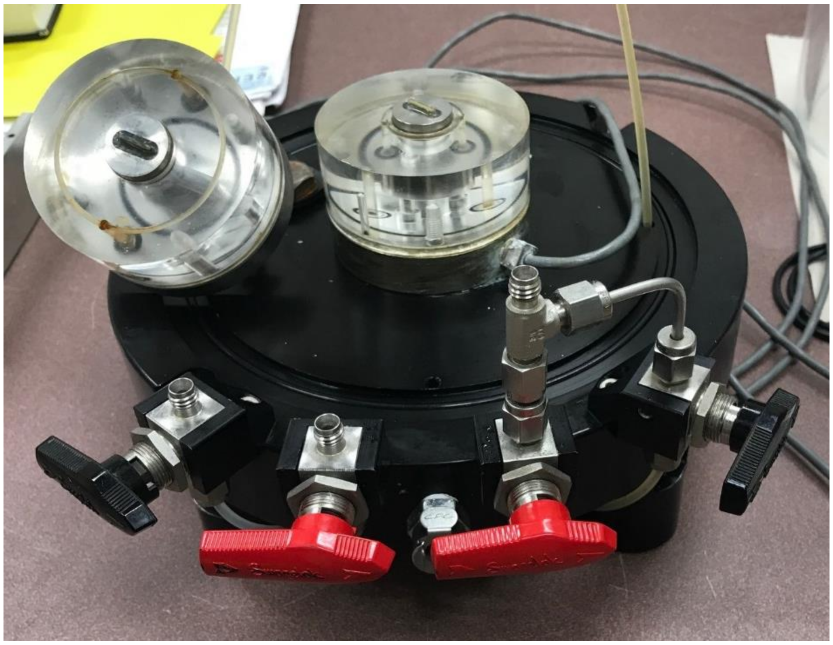

Figure D-3 the two bender elements mounted in the top and bottom caps of the triaxial cell.

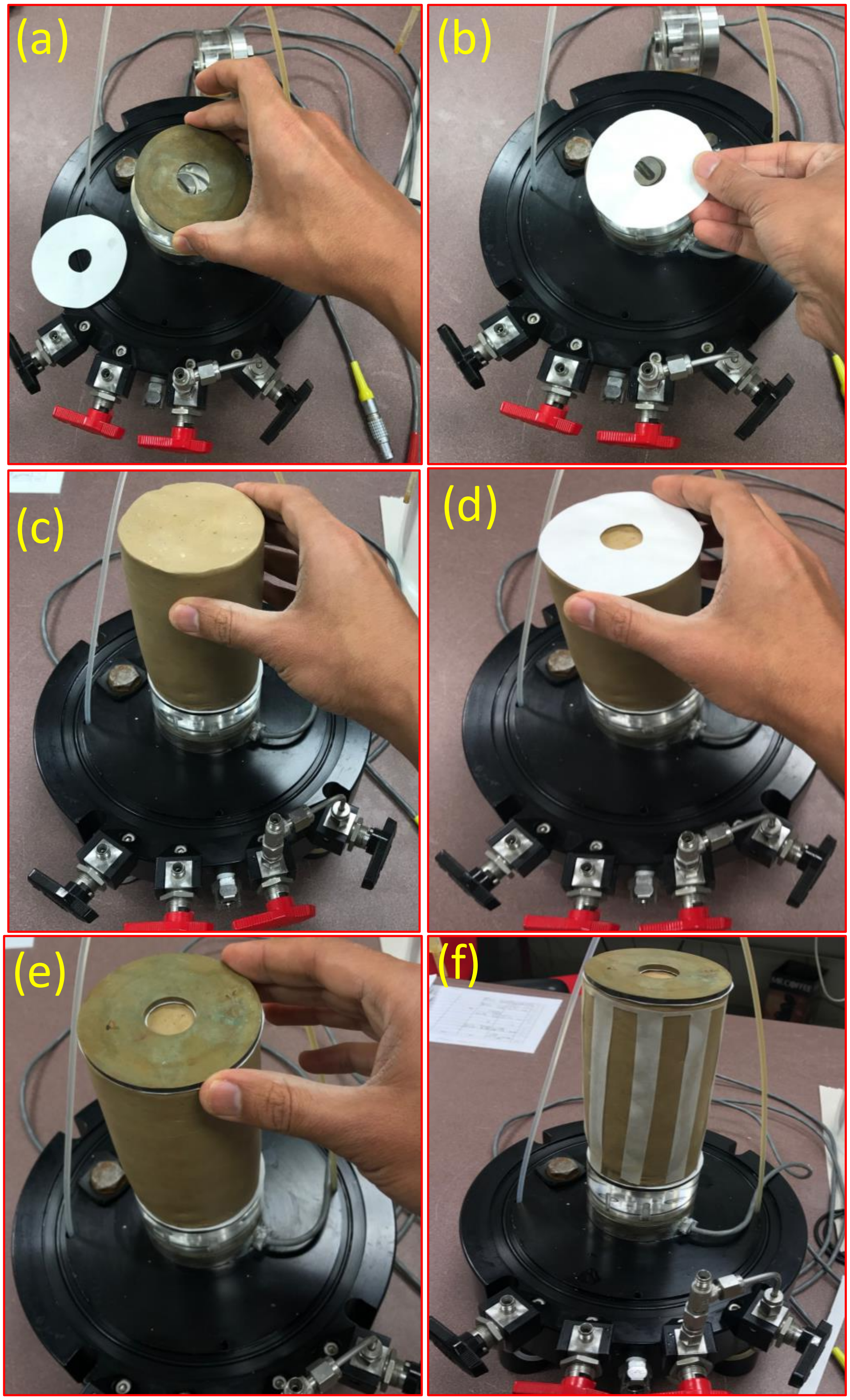

Figure D-4 steps of mounting the sample.

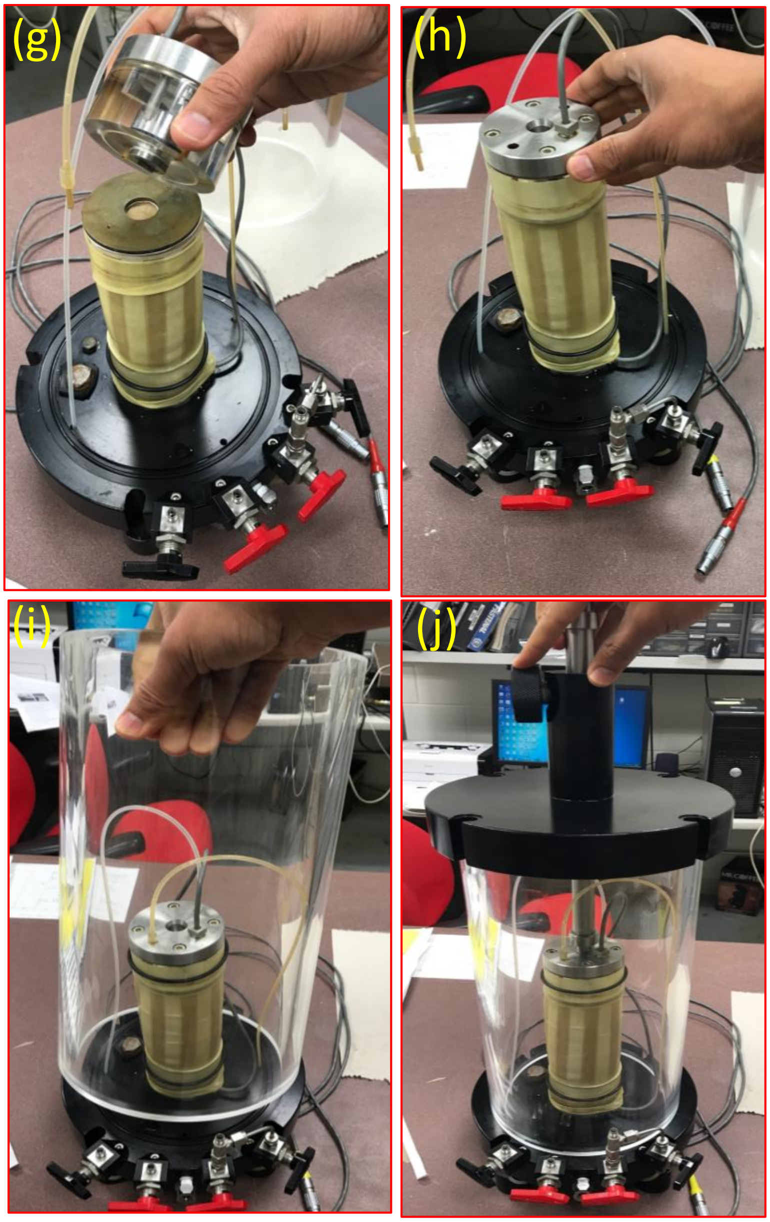

Figure D-5 (continued) steps of mounting of the sample.

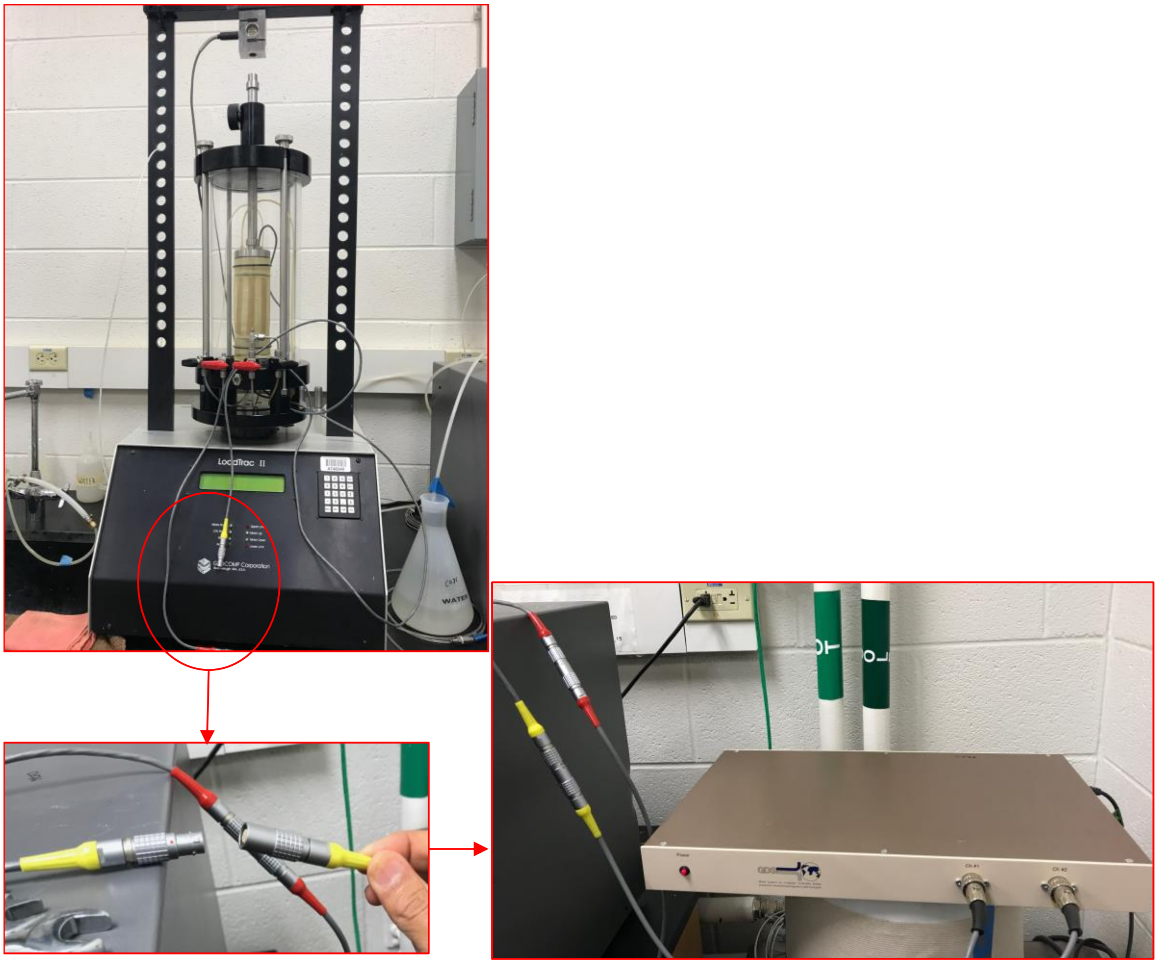

Figure D-6 connecting triaxial cell and signal processor that analyzes the generated waves.

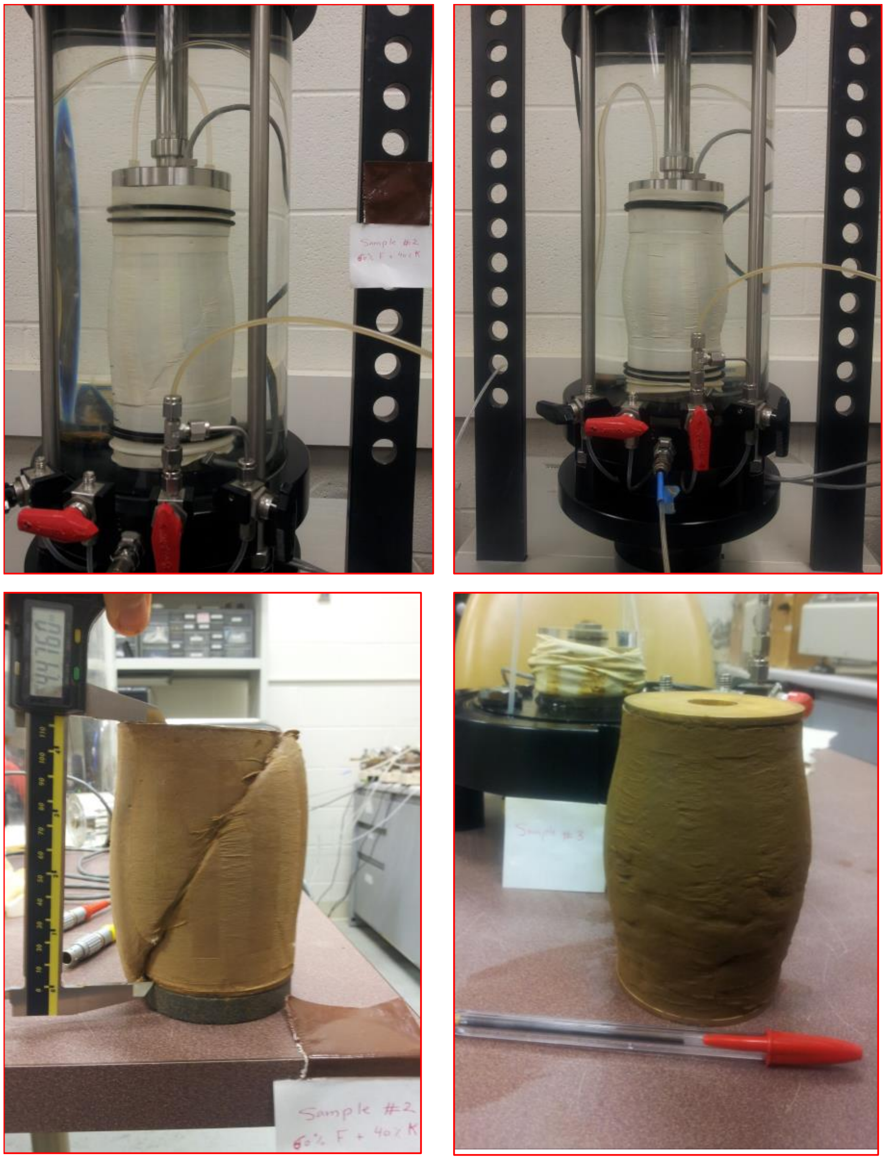

Figure D-7 Typical samples after shearing.

APPENDIX E

Consolidation and Shear Behavior Curves

E-1 Consolidation Testing Curves

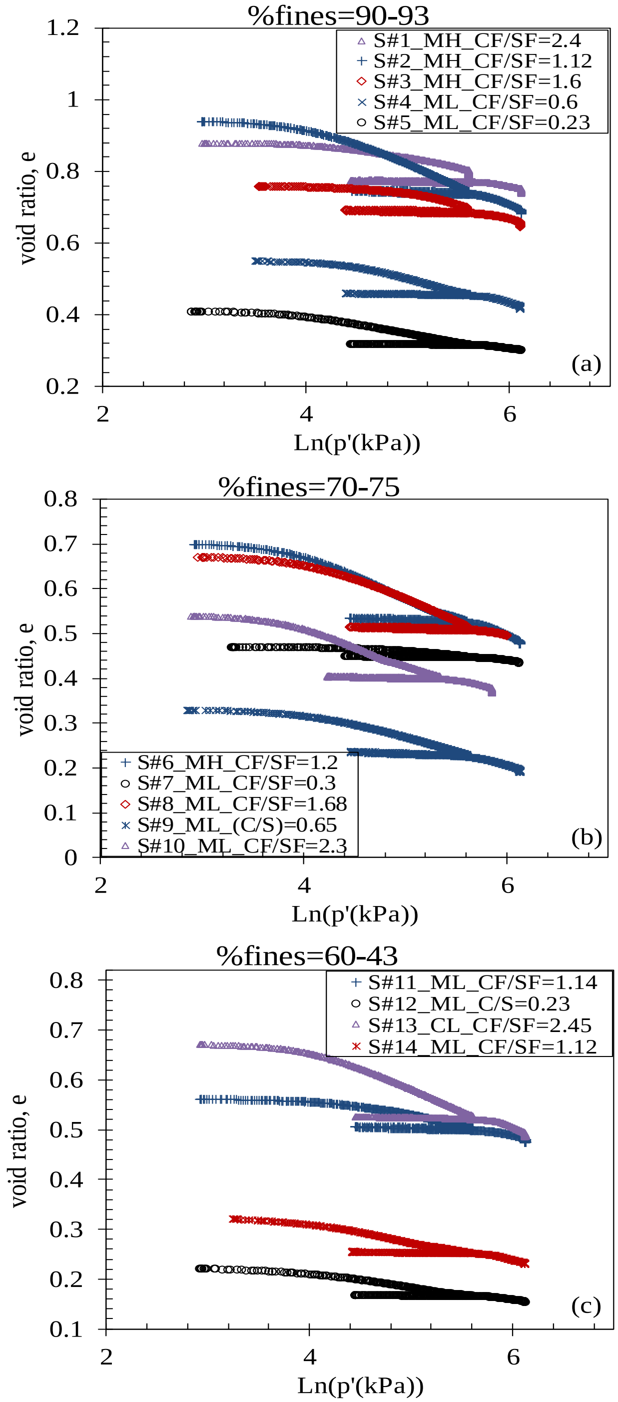

Figure E-1 e-log p’ curves of the tested samples

E-2 Shear Behavior Curves

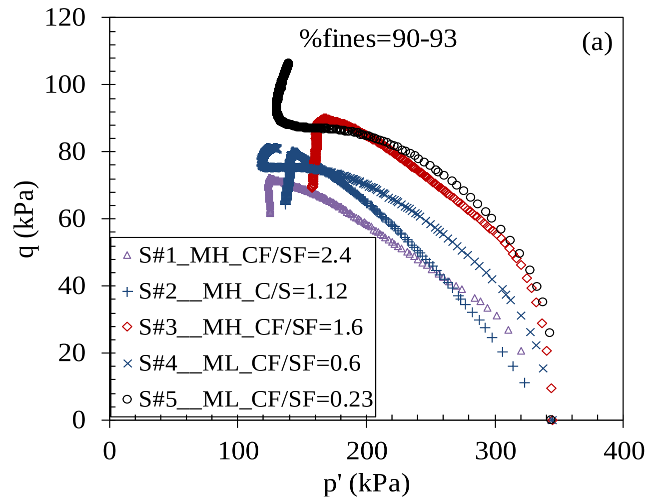

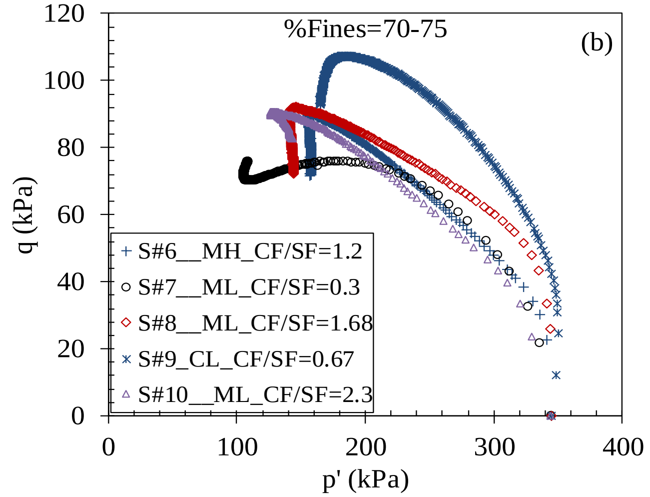

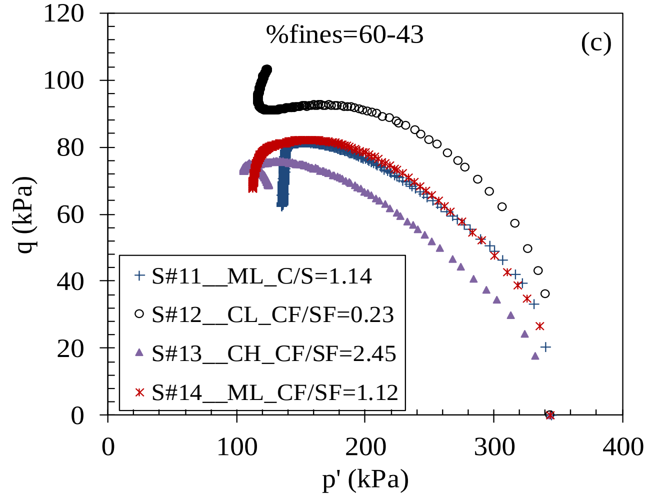

Figure E-3 q-p’ curves of the tested samples.

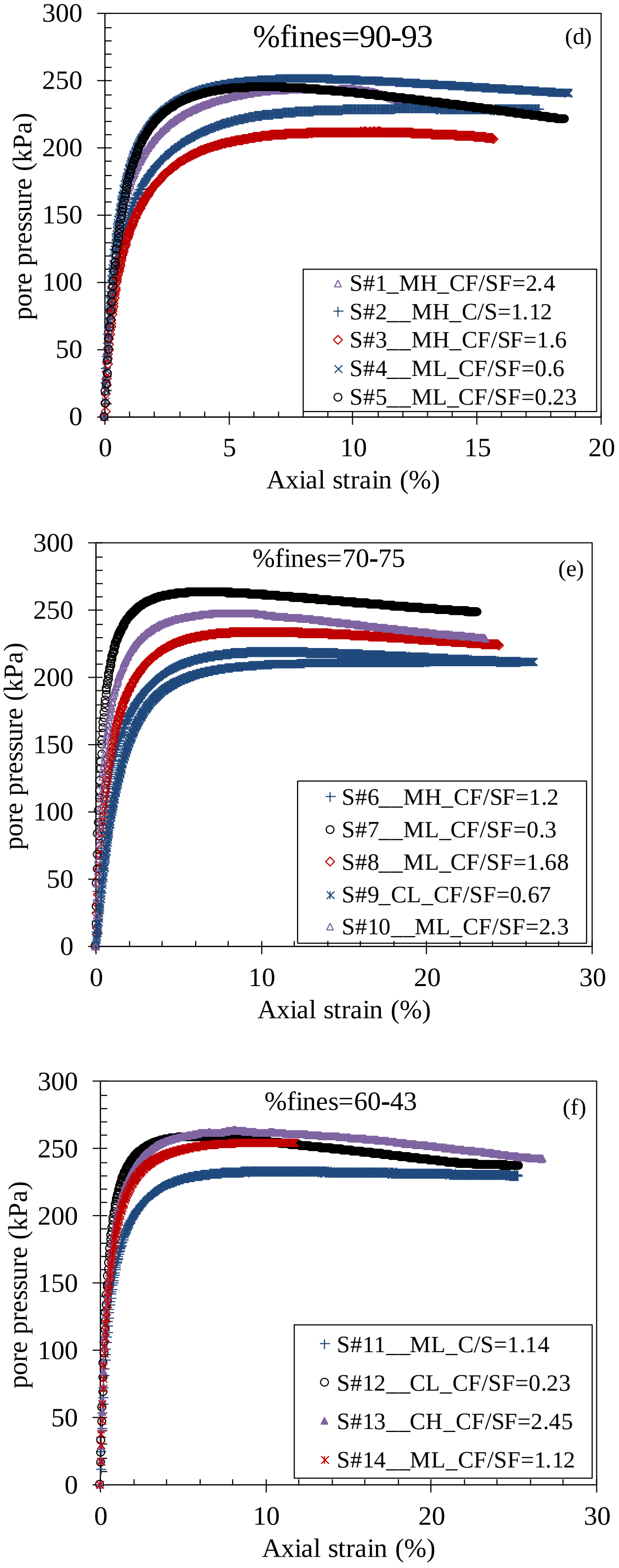

Figure E-4 q-axial strain curves of the tested samples.

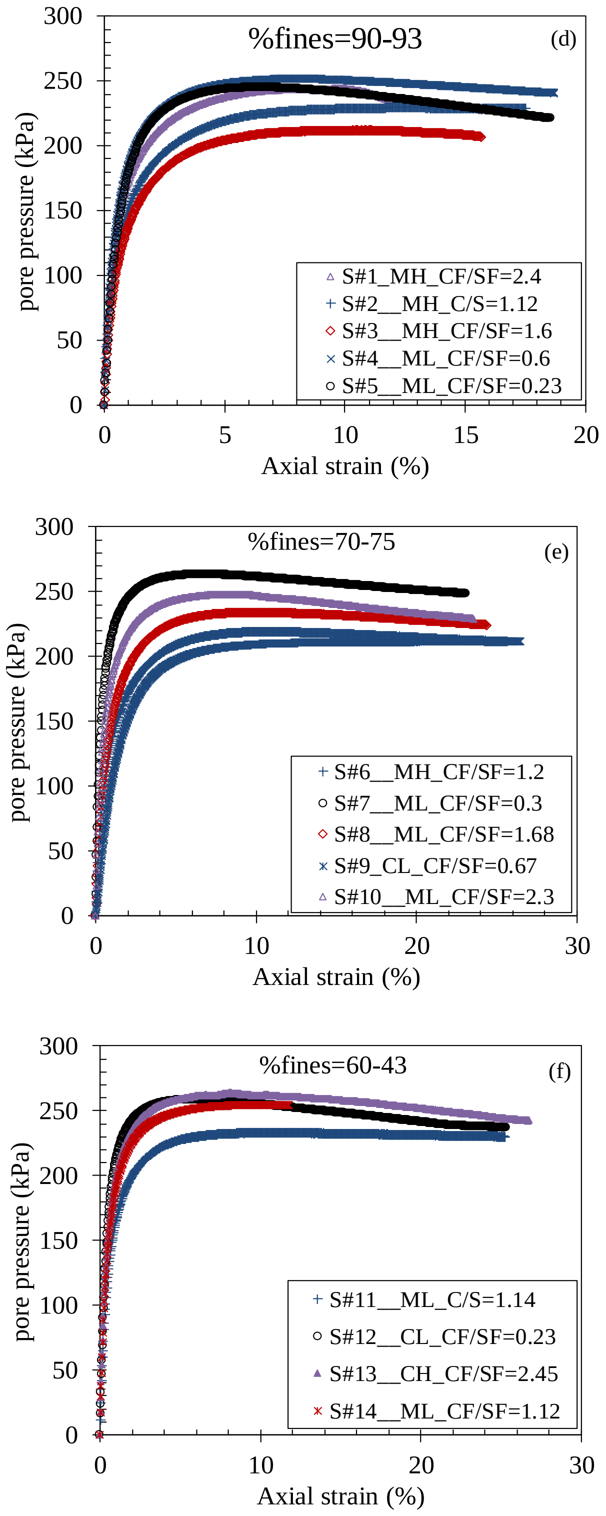

Figure E-5 pore pressure versus axial strain curves of the tested samples.

APPENDIX F

Important Input and Element of Model

Important model Input		**Type**
λ	Compression index	Material property
κ	Swelling index	Material property
φ_{CS}	Critical state friction angle	Material property
Γ	Reference value *csl* in *e* - *p'* space	Material property

Main model elements in terms of shear wave velocity, V_S	
Yield surface	$q = \mathrm{M} \cdot p'_o \cdot \left(a + b \left(\frac{V_S}{V_{So}} \right)^c \right) \cdot \ln \left(a + b \left(\frac{V_S}{V_{So}} \right)^c \right)$
Elastic volumetric strain ε_p^e	$\varepsilon_p^e = -\varepsilon_p^p = \frac{k}{1+e_o} \ln \left(\frac{\left(a + b \left(\frac{V_S}{V_{So}} \right)^c \right)_{previous}}{\left(a + b \left(\frac{V_S}{V_{So}} \right)^c \right)} \right)$
Elastic deviatoric strains, ε_q^e	$\varepsilon_q^e = \frac{q}{3G} = \frac{q}{3\left(\rho \cdot V_S^2\right)}$ where $G = \rho . {V_S}^2$
Plastic shear strain	$\varepsilon_q^p = \varepsilon_p^p \cdot \frac{q}{\mathrm{M}^2 \left[p_o \left(a + b \left(\frac{V_S}{V_{So}} \right)^c \right) - \left(- p'_o / 2 \right) \right]}$

APPENDIX G

Selected Shear Wave Velocity Measurements

G-1: Shear Wave Velocities Measurements under Drained Conditions (Chapter 2):

Sample#1			**Sample#2**		
Shear wave velocity, Vs, (m/s)	Mean effective Stress, p' (kPa)	Void Ratio, *e*	Shear wave velocity, Vs, (m/s)	Mean effective Stress, p' (kPa)	Void Ratio, *e*
128.4	19.2	0.410	151.4	27.6	0.470
131.5	27.1	0.408	152.8	33.9	0.470
137.4	35.7	0.404	155.9	38.9	0.470
151.0	54.3	0.394	186.9	72.4	0.467
169.6	83.7	0.377	191.5	88.1	0.466
179.3	119.7	0.359	199.1	111.3	0.464
190.6	154.4	0.346	204.3	134.2	0.462
203.4	194.7	0.334	212.9	156.7	0.460
209.0	229.5	0.326	218.9	186.7	0.457
221.4	272.5	0.318	225.4	209.1	0.455
-	-	-	228.7	228.9	0.453
-	-	-	179.0	262.8	0.449
-	-	-	195.3	269.8	0.447
-	-	-	197.9	269.5	0.447
-	-	-	187.8	270.2	0.446

Sample#3			**Sample#4**		
Shear wave velocity, Vs, (m/s)	Mean effective Stress, p' (kPa)	Void Ratio, *e*	Shear wave velocity, Vs, (m/s)	Mean effective Stress, p' (kPa)	Void Ratio, *e*
136.0	19.7	0.220	115.0	18.4	0.330
144.1	31.1	0.216	119.5	25.1	0.328
151.7	39.4	0.213	121.5	31.4	0.326
155.0	46.6	0.211	126.7	39.9	0.323
162.0	57.5	0.208	131.3	48.2	0.319
167.7	65.2	0.205	140.1	66.7	0.310
171.7	74.6	0.202	148.6	89.1	0.297
178.0	87.5	0.198	169.6	111.1	0.286
184.9	99.7	0.194	177.8	132.8	0.276
189.8	109.4	0.192	191.7	172.9	0.260
192.3	118.3	0.189	202.4	199.9	0.251
200.4	131.3	0.186	211.2	227.3	0.242
203.1	143.3	0.183	217.4	255.0	0.235
212.2	159.3	0.180	227.7	272.9	0.228
215.3	177.1	0.176	-	-	-
222.0	195.2	0.173	-	-	-
229.0	218.4	0.170	-	-	-
236.6	237.8	0.168	-	-	-
244.7	260.3	0.166	-	-	-
249.0	272.5	0.165	-	-	-
253.5	272.4	0.164	-	-	-

Sample#5			**Sample#6**		
Shear wave velocity, Vs, (m/s)	Mean effective Stress, p’ (kPa)	Void Ratio, *e*	Shear wave velocity, Vs, (m/s)	Mean effective Stress, p’ (kPa)	Void Ratio, *e*
105.0	20.0	0.740	110.4	20.2	0.940
112.5	36.8	0.730	114.4	28.5	0.937
119.0	65.4	0.707	117.7	39.4	0.929
132.5	86.2	0.689	124.2	52.8	0.916
146.3	119.0	0.662	130.2	70.0	0.898
143.9	159.3	0.633	144.5	106.8	0.860
155.7	194.2	0.612	162.7	151.4	0.820
163.0	208.2	0.605	177.6	193.7	0.788
175.3	272.2	0.576	198.1	262.7	0.749
-	-	-	209.2	272.6	0.739
-	-	-	212.2	272.5	0.737
-	-	-	215.3	272.3	0.736

Sample#7			**Sample#8**		
Shear wave velocity, Vs, (m/s)	Mean effective Stress, p’ (kPa)	Void Ratio, *e*	Shear wave velocity, Vs, (m/s)	Mean effective Stress, p’ (kPa)	Void Ratio, *e*
164.5	26.6	0.320	161.4	19.4	0.560
172.2	30.1	0.318	164.6	24.5	0.560
178.4	37.6	0.315	173.8	36.9	0.558
194.9	56.4	0.308	179.8	50.4	0.556
202.9	70.0	0.302	186.3	58.4	0.554
227.6	112.1	0.284	183.8	74.6	0.549
246.6	142.3	0.273	198.0	86.1	0.546
250.7	154.5	0.270	205.8	103.2	0.541
259.5	170.4	0.266	214.2	123.7	0.536
268.9	193.7	0.263	226.8	144.4	0.530
278.9	222.1	0.258	233.4	166.7	0.524
290.0	244.0	0.255	248.4	195.4	0.517
302.0	269.4	0.252	256.5	221.1	0.512
308.3	270.6	0.250	265.2	252.4	0.506
-	-	-	274.6	272.3	0.502
-	-	-	284.9	272.6	0.499

Sample#9			**Sample#10**		
Shear wave velocity, Vs, (m/s)	Mean effective Stress, p’ (kPa)	Void Ratio, *e*	Shear wave velocity, Vs, (m/s)	Mean effective Stress, p’ (kPa)	Void Ratio, *e*
121.6	34.7	0.760	93.0	20.5	0.670
124.0	47.6	0.759	107.9	21.9	0.670
128.7	72.1	0.755	111.7	34.4	0.665
132.0	87.5	0.752	114.0	46.3	0.658
134.3	103.6	0.749	126.4	57.5	0.650
137.9	123.0	0.745	130.5	69.8	0.639
156.5	162.5	0.736	133.8	80.4	0.630
161.4	185.1	0.729	137.2	92.3	0.620
166.5	218.0	0.717	142.2	105.7	0.609
170.0	241.2	0.709	146.2	116.9	0.601
175.8	267.2	0.700	153.4	139.6	0.585
179.9	267.4	0.694	159.7	159.4	0.572
182.0	267.0	0.690	166.6	181.8	0.559
-	-	-	174.2	200.4	0.549
-	-	-	178.1	221.5	0.539
-	-	-	146.9	243.8	0.529
-	-	-	151.2	266.4	0.520
-	-	-	174.9	272.3	0.514
-	-	-	160.9	272.5	0.509
-	-	-	162.7	272.3	0.508

Sample#11			**Sample#12**		
Shear wave velocity, Vs, (m/s)	Mean effective Stress, p’ (kPa)	Void Ratio, *e*	Shear wave velocity, Vs, (m/s)	Mean effective Stress, p’ (kPa)	Void Ratio, *e*
107.4	19.4	0.540	121.6	19.5	0.670
112.8	26.5	0.536	128.6	29.9	0.667
121.1	32.8	0.532	130.7	37.0	0.664
125.5	43.2	0.523	135.1	47.6	0.658
130.0	48.3	0.517	142.5	58.4	0.649
134.5	55.1	0.509	147.7	70.5	0.639
137.1	59.8	0.504	165.3	87.8	0.624
140.6	67.3	0.495	172.6	103.9	0.612
145.8	76.8	0.483	180.5	120.9	0.598
155.0	92.3	0.468	187.1	134.6	0.589
161.5	106.0	0.455	191.6	146.5	0.582
166.7	115.3	0.446	196.6	156.3	0.577
171.0	125.3	0.439	199.0	166.4	0.571
177.1	135.0	0.435	204.4	172.9	0.567
181.4	146.5	0.430	209.9	189.9	0.559
185.6	157.1	0.425	215.8	205.7	0.552
189.9	168.9	0.419	218.9	214.3	0.548
195.6	179.3	0.415	225.3	231.6	0.541
201.2	187.8	0.412	232.3	246.8	0.535
206.3	202.7	0.407	247.4	272.5	0.523
219.4	209.1	0.400	256.1	272.5	0.521

G-2: Shear Wave Velocities Measurements during Undrained Shear Conditions (Chapter 3):

Sample#1				
Shear wave velocity, Vs, (m/s)	Vertical (axial) strain (%)	Porewater pressure, *u*, (kPa)	Mean effective Stress, p’ (kPa)	Deviatoric stress, *q*, (kPa)
198.2	0.00	0.0	344.1	-0.1
195.1	0.21	87.8	269.7	40.2
188.3	1.04	173.8	190.6	60.7
187.3	1.60	196.4	169.7	65.8
186.2	2.14	209.6	157.2	68.0
182.6	2.78	220.1	147.2	69.5
181.4	3.42	227.4	140.2	70.2
159.8	4.81	236.7	131.2	71.3
158.6	5.55	239.9	128.1	71.6

Sample#2

Shear wave velocity, Vs, (m/s)	Vertical (axial) strain (%)	Porewater pressure, *u*, (kPa)	Mean effective Stress, p' (kPa)	Deviatoric stress, *q*, (kPa)
237.7	0.00	0.0	344.3	0.0
237.5	0.05	35.7	314.1	16.2
237.2	0.19	72.9	282.2	32.2
236.6	0.44	108.0	251.8	45.8
235.0	1.11	156.4	208.6	62.0
233.9	1.60	175.0	191.9	67.4
232.8	2.07	186.5	181.4	70.5
229.2	3.56	208.6	161.2	75.9
225.7	5.00	219.3	151.1	78.0
223.7	5.90	223.1	147.6	78.9
218.6	11.17	229.0	141.8	79.2

Sample#3

Shear wave velocity, Vs, (m/s)	Vertical (axial) strain (%)	Porewater pressure, *u*, (kPa)	Mean effective Stress, p' (kPa)	Deviatoric stress, *q*, (kPa)
186.3	0.00	0.0	344.3	0.0
186.2	0.03	19.9	331.9	22.3
186.0	0.31	108.0	255.3	56.8
184.0	0.83	173.9	194.3	71.2
182.4	2.10	222.4	147.1	75.5
174.2	5.18	248.6	120.9	75.6

Sample#4				
Shear wave velocity, Vs, (m/s)	Vertical (axial) strain (%)	Porewater pressure, *u*, (kPa)	Mean effective Stress, p' (kPa)	Deviatoric stress, *q*, (kPa)
266.6	0.00	0.0	344.4	0.0
259.4	0.83	122.1	244.8	67.3
252.2	1.73	163.7	207.0	78.8
247.6	3.52	196.8	176.6	86.7
241.9	7.50	216.9	157.7	90.3
243.2	8.77	218.4	156.2	90.3

Sample#5				
Shear wave velocity, Vs, (m/s)	Vertical (axial) strain (%)	Porewater pressure, *u*, (kPa)	Mean effective Stress, p' (kPa)	Deviatoric stress, *q*, (kPa)
333.7	0.00	0.0	345.0	0.0
318.1	0.37	106.1	259.6	62.1
310.2	0.69	143.7	225.1	71.3
302.5	1.12	171.5	199.1	76.7
295.1	1.52	187.3	184.1	79.0
293.9	1.95	198.3	173.4	80.3
292.0	2.56	209.3	162.9	81.3

Sample#6				
Shear wave velocity, Vs, (m/s)	Vertical (axial) strain (%)	Porewater pressure, *u*, (kPa)	Mean effective Stress, p' (kPa)	Deviatoric stress, *q*, (kPa)
295.1	0.00	0.0	344.4	0.0
282.3	0.22	90.6	278.4	73.8
265.3	0.54	164.6	209.8	89.9
259.6	0.78	193.0	182.1	92.2
254.0	1.10	216.0	159.1	92.3

Sample#7				
Shear wave velocity, Vs, (m/s)	Vertical (axial) strain (%)	Porewater pressure, *u*, (kPa)	Mean effective Stress, p' (kPa)	Deviatoric stress, *q*, (kPa)
289.6	0.03	18.1	332.5	17.7
283.2	0.24	102.5	258.8	49.9
277.2	0.43	140.3	224.6	60.5
276.5	0.64	170.2	197.0	67.6
270.5	0.89	192.1	176.5	71.6
264.5	1.24	211.6	157.9	74.1
263.4	1.66	226.7	143.1	75.5

Sample#8				
Shear wave velocity, Vs, (m/s)	Vertical (axial) strain (%)	Porewater pressure, *u*, (kPa)	Mean effective Stress, p' (kPa)	Deviatoric stress, *q*, (kPa)
360.9	0.00	0.0	344.6	0.0
342.2	0.33	114.2	252.2	65.7
324.7	0.79	174.8	196.2	79.0
315.2	1.49	212.4	159.6	82.2
313.8	1.92	223.9	148.0	82.1

REFERENCES

Adu-Gyamfi, K., L. S. Bryson and L. Janbakhsh 2011. Prediction of moisture-density characteristics of compacted fill using mixture theory. 14th Pan-American Conference on Soil Mechanics and Geotechnical Engineering (PCSMGE).

Ahmed, S. M. 2017. Correlating the shear wave velocity with the cone penetration test. Proceedings of the 2nd World Congress on Civil, Structural, and Environmental Engineering (CSEE'17). Barcelona, Spain.

Allen, P. A., N. A. Michael, M. D'Arcy, D. C. Roda-Boluda, A. C. Whittaker, R. A. Duller and J. J. Armitage 2017. Fractionation of grain size in terrestrial sediment routing systems. Basin Research 29 (2), 180-202.

Aris, M., N. Benahmed and S. Bonelli 2012. Experimental geomechanics: a laboratory study on the behaviour of granular material using bender elements. European Journal of Environmental and Civil Engineering 16 (1), 97-110.

Assier-Rzadkieaicz, S., P. Heinrich, P. Sabatier, B. Savoye and J. Bourillet 2000. Numerical modelling of a landslide-generated tsunami: the 1979 Nice event. Pure and Applied Geophysics 157 (10), 1707-1727.

ASTM D422 2007. Standard test method for particle-size analysis of soils. ASTM International, West Conshohocken, PA, USA.

ASTM D2487 2006. Standard practice for classification of soils for engineering purposes (Unified Soil Classification System). ASTM International, West Conshohocken, PA, USA.

ASTM D4318 1994. Standard test method for liquid limit, plastic limit and plasticity index of soils. Annual book of ASTM Standards, West Conshohocken, PA, USA.

ASTM D4767 2004. Standard test method for consolidated undrained triaxial compression test for cohesive soils. ASTM International, West Conshohocken, PA, USA.

Bartetzko, A. and A. J. Kopf 2007. The relationship of undrained shear strength and porosity with depth in shallow (< 50 m) marine sediments. Sedimentary Geology 196 (1-4), 235-249.

Blott, S. J. and K. Pye 2012. Particle size scales and classification of sediment types based on particle size distributions: Review and recommended procedures. Sedimentology 59 (7), 2071-2096.

Brain, M. J., A. J. Long, D. N. Petley, B. P. Horton and R. J. Allison 2011. Compression behaviour of minerogenic low energy intertidal sediments. Sedimentary Geology 233 (1-4), 28-41.

Brierley, G. J. and K. A. Fryirs 2013. Geomorphology and river management: applications of the river styles framework. Hoboken, New Jersey, John Wiley and Sons.

Bryson, L. S., M. Mahmoodabadi and K. Adu-Gyamfi 2017. Prediction of consolidation and shear behavior of Fly Ash–soil mixtures using mixture theory. Journal of Materials in Civil Engineering 29 (11), 04017222.

Burland, J. 1990. On the compressibility and shear strength of natural clays. Géotechnique 40 (3), 329-378.

Caldwell, R. L. and D. A. Edmonds 2014. The effects of sediment properties on deltaic processes and morphologies: A numerical modeling study. Journal of Geophysical Research: Earth Surface 119 (5), 961-982.

Cha, M., J. C. Santamarina, H.-S. Kim and G.-C. Cho 2014. Small-strain stiffness, shear-wave velocity, and soil compressibility. Journal of Geotechnical and Geoenvironmental Engineering 140 (10), 06014011.

Chai, J.-C., S.-L. Shen, H.-H. Zhu and X.-L. Zhang 2004. Land subsidence due to groundwater drawdown in Shanghai. Geotechnique 54 (2), 143-147.

Chang, I., T.-H. Kwon and G.-C. Cho 2011. An experimental procedure for evaluating the consolidation state of marine clay deposits using shear wave velocity. Smart Structures and Systems 7 (4), 289-302.

Cheng, Z. and H. Liu 2015. Digital grain-size analysis based on autocorrelation algorithm. Sedimentary Geology 327, 21-31.

Choo, H., H. Jun and H.-K. Yoon 2018. Porosity estimation of unsaturated soil using Brutsaert equation. Soil Dynamics and Earthquake Engineering 104, 33-39.

Chung, C. K. and R. J. Finno 1992. Influence of depositional processes on the geotechnical parameters of Chicago glacial clays. Engineering Geology 32 (4), 225-242.

Connor, D. W., J. H. Allen, N. Golding, K. L. Howell, L. M. Lieberknecht, K. O. Northen and J. B. Reker 2004. The marine habitat classification for britain and ireland. Version 04.05. Joint Nature Conservation Committee, Peterborough.

Dalrymple, R. W., B. A. Zaitlin and R. Boyd 1992. Estuarine facies models: conceptual basis and stratigraphic implications: perspective. Journal of Sedimentary Research 62 (6), 1130-1146.

Dipova, N. 2011. Geotechnical characterization and facies change detection of the Bogacay coastal plain (Antalya, Turkey) soils. Environmental Earth Sciences 62 (4), 883-896.

Edmonds, D. A. and R. L. Slingerland 2010. Significant effect of sediment cohesion on delta morphology. Nature Geoscience 3 (2), 105-109.

Erguler, Z. A. 2016. A quantitative method of describing grain size distribution of soils and some examples for its applications. Bulletin of Engineering Geology and the Environment 75 (2), 807-819.

Fam, M. and J. Santamarina 1997. A study of consolidation using mechanical and electromagnetic waves. Geotechnique 47 (2), 203-219.

Flemming, B. W. 2000. A revised textural classification of gravel-free muddy sediments on the basis of ternary diagrams. Continental shelf research 20 (10-11), 1125-1137.

Folk, R. L. 1980. Petrology of sedimentary rocks. Austin, Texas, Hemphill Publishing Company.

Friedman, G. M. 1979. Differences in size distributions of populations of particles among sands of various origins: addendum to IAS Presidential Address. Sedimentology 26 (6), 859-862.

Garcia-Romero, E., J. Vegas, J. L. Baldonedo and R. Marfil 2005. Clay minerals as alteration products in basaltic volcaniclastic deposits of La Palma (Canary Islands, Spain). Sedimentary Geology 174 (3), 237-253.

GeoComp 2015. User's Manual, LoadTrac-II. 125 Nagog Park, Acton, MA 01720 U.S.A., GeoComp Corp.

Germaine, J. T. and A. V. Germaine 2009. Geotechnical laboratory measurements for engineers, John Wiley & Sons.

Geyer, R. A. 2018. Handbook of geophysical exploration at sea: 2nd Editions-Hard Minerals, CRC Press.

Geyer, R. A. and M. Ashwell 1991. Handbook of geophysical exploration at sea, CRC Press.

Hardin, B. O. and V. P. Drnevich 1972. Shear modulus and damping in soils: measurement and parameter effects. Journal of Soil Mechanics & Foundations Div 98 (sm6).

Hathaway, J. C. 1971. Data file, continental margin program, Atlantic coast of the United States: vol. 2 sample collection and analytical data. Woods Hole, Massachustts, Woods Hole Oceanographic Institution.

Horpibulsuk, S., M. D. Liu, Z. Zhuang and Z.-S. Hong 2016. Complete compression curves of reconstituted clays. International Journal of Geomechanics 16 (6), 06016005.

Irfan, M., T. Uchimura and Y. Chen 2017. Effects of soil deformation and saturation on elastic wave velocities in relation to prediction of rain-induced landslides. Engineering Geology 230, 84-94.

Jang, J. and C. J. Santamarina 2015. Fines classification based on sensitivity to pore-fluid chemistry. Journal of Geotechnical and Geoenvironmental Engineering 142 (4), 06015018.

Kawaguchi, T., T. Mitachi and S. Shibuya 2001. Evaluation of shear wave travel time in laboratory bender element test. Proceedings of the International Conference on Soil Mechanics and Geotechnical Engineering, AA BALKEMA PUBLISHERS.

Kim, H.-S., G.-C. Cho, J. Y. Lee and S.-J. Kim 2013. Geotechnical and geophysical properties of deep marine fine-grained sediments recovered during the second Ulleung Basin Gas Hydrate expedition, East Sea, Korea. Marine and Petroleum Geology 47, 56-65.

Klein, K. and J. C. Santamarina 2005. Soft sediments: Wave-based characterization. International Journal of Geomechanics 5 (2), 147-157.

Kuecher, G. J. 1994. Geologic framework and consolidation settlement potential of the lafourche delta, topstratum valley fill; implications for wetland loss in Terrebonne and Lafourche Parishes, Louisiana.

Kulhawy, Fred H., and Paul W. Mayne. 1990. Manual on estimating soil properties for foundation design, No. EPRI-EL-6800, Electric Power Research Inst., Palo Alto, CA (USA); Cornell Univ., Ithaca, NY (USA). Geotechnical Engineering Group.

Kwon, T.-H., K.-R. Lee, G.-C. Cho and J. Y. Lee 2011. Geotechnical properties of deep oceanic sediments recovered from the hydrate occurrence regions in the Ulleung Basin, East Sea, offshore Korea. Marine and Petroleum Geology 28 (10), 1870-1883.

Lee, J.-S. and J. C. Santamarina 2005. Bender elements: performance and signal interpretation. Journal of geotechnical and geoenvironmental engineering 131 (9), 1063-1070.

Leong, E. C., J. Cahyadi and H. Rahardjo 2009. Measuring shear and compression wave velocities of soil using bender–extender elements. Canadian geotechnical journal 46 (7), 792-812.

Li, B. and X. Zeng 2014. Effects of fabric anisotropy on elastic shear modulus of granular soils. Earthquake Engineering and Engineering Vibration 13 (2), 269-278.

Liu, M. D., K. Xu and S. Horpibulsuk 2013. A mathematical function to represent S-shaped relationships for geotechnical applications. Proceedings of the Institution of Civil Engineers - Geotechnical Engineering 166 (3), 321-327.

Liu, M. D., Z. Zhuang and S. Horpibulsuk 2013. Estimation of the compression behaviour of reconstituted clays. Engineering Geology 167, 84-94.

Marinho, F. 2017. Fundamentals of soil shrinkage. PanAm Unsaturated Soils 2017, 198-222.

Mason, C. C. and R. L. Folk 1958. Differentiation of beach, dune, and aeolian flat environments by size analysis, Mustang Island, Texas. Journal of Sedimentary Research 28 (2).

Masson, D., C. Harbitz, R. Wynn, G. Pedersen and F. Løvholt 2006. Submarine landslides: processes, triggers and hazard prediction. Philosophical Transactions of the Royal Society of London A: Mathematical, Physical and Engineering Sciences 364 (1845), 2009-2039.

Meehan, C. 2006. An experimental study of the dynamic behavior of slickensided slip surfaces, Ph. D. thesis, Virginia Tech.

Mitchell, J. K. and K. Soga 2005. Fundamentals of soil behavior. Hoboken, New Jersey, John Wiley & Sons New York.

Moore, D. G. 1964. Shear strength and related properties of sediments from experimental Mohole (Guadalupe site). Journal of Geophysical Research 69 (20), 4271-4291.

Moreno-Maroto, J. M. and J. Alonso-Azcárate 2018. What is clay? A new definition of "clay" based on plasticity and its impact on the most widespread soil classification systems. Applied Clay Science 161, 57-63.

Muttashar, W. R. 2005. Analysis of mechanisms used in desiccation of southern marshes in Iraq, and the possibility of exploitation this mechanism positively. Marina Mesopotamia Journal 1 (20), 183-196.

Muttashar, W. R., L. S. Bryson, M. McGlue and E. Woolery 2018. A Methodology for characterizing and classifying unconsolidated inorganic fine-grained sediments. in press.

Muttashar, W. R., L. S. Bryson and E. Woolery 2018. Determining the effects of depositional processes on consolidation behavior of sediment using shear-wave velocity. Marine Georesources & Geotechnology, 1-12.

Net, L. I., M. S. Alonso and C. O. Limarino 2002. Source rock and environmental control on clay mineral associations, Lower Section of Paganzo Group (Carboniferous), Northwest Argentina. Sedimentary Geology 152 (3), 183-199.

Oh, T.-M., E.-S. Bang, G.-C. Cho and E.-S. Park 2017. Estimation of undrained shear strength for saturated clay using shear wave velocity. Marine Georesources and Geotechnology 35 (2), 236-244.

Petrakis, E. and R. Dobry 1987. Micromechanical modeling of granular soil at small strain by arrays of elastic spheres, Rensselaer Polytechnic Inst Troy NY Deptartment of Civil Engineering.

Polidori, E. 2009. Reappraisal of the activity of clays. Activity chart. Soils and foundations 49 (3), 431-441.

Polidori, E. 2015. Proposal for a new classification of common inorganic soils for engineering purposes. Geotechnical and Geological Engineering 33 (6), 1569-1579.

Reaves, C. A., and Nichols, M. L. 1955. Surface soil reaction to pressure. Agric. Eng 36, 813-816.

Rees, S., A. Le Compte and K. Snelling 2013. A new tool for the automated travel time analyses of bender element tests. Proceedings of the 18th International Conference on Soil Mechanics and Geotechnical Engineering.

Santamarina, J. and M. Aloufi 1999. Small strain stiffness: A micromechanical experimental study. Proceedings of Pre-failure Deformation Characteristics of Geomaterials, 451-458.

Santamarina, J. and G. Cascante 1996. Stress anisotropy and wave propagation: a micromechanical view. Canadian Geotechnical Journal 33 (5), 770-782.

Santamarina, J., K. Klein and M. Fam 2001. Soils and waves, 488 pp, John Wiley, New York.

Sarti, G., V. Rossi and A. Amorosi 2012. Influence of Holocene stratigraphic architecture on ground surface settlements: A case study from the City of Pisa (Tuscany, Italy). Sedimentary Geology 281, 75-87.

Skempton, A. W. 1953. The Colloidal "Activity" of Clays. Proceddings of the 3th International Conference on Soil Mechanics and Foundation Engineering, Switzerland.

Stewart Jr, H. B. 1958. Sedimentary reflections of depositional environment in San Miguel lagoon, Baja California, Mexico. AAPG bulletin 42 (11), 2567-2618.

Terzaghi, K., R. B. Peck and G. Mesri 1996. Soil mechanics in engineering practice. .John Wiley & Sons ,Hoboken, New Jersey

Tong, L., J. Zhang, K. Sun, Y. Guo, J. Zheng and D.-S. Jeng 2018. Experimental study on soil response and wave attenuation in a silt bed. Ocean Engineering 160, 105-118.

Truong, M. H., V. L. Nguyen, T. K. O. Ta and J. Takemura 2011. Changes in late Pleistocene–Holocene sedimentary facies of the Mekong River Delta and the influence of sedimentary environment on geotechnical engineering properties. Engineering geology 122 (3), 146-159.

Vanneste, M., N. Sultan, S. Garziglia, C. F. Forsberg and J.-S. L'Heureux 2014. Seafloor instabilities and sediment deformation processes: the need for integrated, multi-disciplinary investigations. Marine Geology 352, 183-214.

Verruijt, A. 2018. Stress strain relations. An introduction to soil mechanics, Springer, 97-107.

Viggiani, G. and J. Atkinson 1995. Interpretation of bender element tests. International Journal of Rock Mechanics and Mining Sciences and Geomechanics Abstracts.

Wu, T. H. 1958. Geotechnical properties of glacial lake clays. Journal of the Soil Mechanics and Foundations Division 84 (3), 1-34.

Yamashita, S., T. Kawaguchi, Y. Nakata, T. Mikami, T. Fujiwara and S. Shibuya 2009. Interpretation of international parallel test on the measurement of Gmax using bender elements. Soils and foundations 49 (4), 631-650.

Zhang, X., Z. Li, P. Li, S. Cheng, Y. Zhang, S. Tang and T. Wang 2015. A model to study the grain size components of the sediment deposited in aeolian–fluvial interplay erosion watershed. Sedimentary Geology 330, 132-140.

Zhang, Y., Y.-Q. Xue, J.-C. Wu, J. Yu, Z.-X. Wei and Q.-F. Li 2008. Land subsidence and earth fissures due to groundwater withdrawal in the southern Yangtse Delta, China. Environmental Geology 55 (4), 751.

Zhang, Z., H. Qiu, X. Zhang and H. Zhang 2017. Application and analysis of measurement model for calibrating spatial shear surface in triaxial test. IOP Conference Series: Materials Science and Engineering, IOP Publishing.

VITA

Wisam Razzaq Muttashar

A. EDUCATION

Ph.D. Candidate:	Spring 2016 – present, Earth and Environmental Sciences, University of Kentucky, Recently.
Master of Sciences:	2002, Engineering Geology, University of Basrah, Iraq.
Bachelor of Sciences:	1999, Geology. University of Basrah, Iraq.

B. PROFESSIONAL EXPERIENCE

Researcher in Engineering Geology, Marine Sciences Center, University of Basrah 2002 till 2013.

C. SELECTED PUBLICATIONS

1- **Muttashar**, **W.R**, Bryson, L.S., Woolery, E. (2018). "Determining the effects of depositional processes on consolidation behavior of sediment using shear-wave velocity". Marine Georesources & Geotechnology: 1-12.

2- **Muttashar**, **W.R**, Bryson, L.S., Woolery, E. and McGlue M. (2018). " A Methodology for characterizing and classifying unconsolidated inorganic fine-grained sediments". Conference paper, GSA annual meeting, 2018.

3- **Muttashar, W.R**, Al-Mosawi, W. M., Al-Aesawi Q. M. and Abass N. (2012). "Detection of subsurface layers by Sub Bottom Profiling (SBP) of cross section of Shatt Al-Arab River at Al-Rebat branch, Basrah, southern Iraq. Mesopotamian Journal of Marine Science. Vol.(1), No. 27, p 49-58.

4- **Muttashar**, **W. R.**, & Al-Amari, F. K. (2012). Geotechnical analysis for types of surficial fine-grained Soils at eastern side of Basra region, Southern Iraq. *Journal of Univesity of Thi-Qar, 7*(2), 1-11.

5- **Muttashar, W. R.**, Al-Tai, M. A., Al-Amari, F. K., & Ali, A. H. (2010). Geotechnical properties of some tidal flat sediments of Khor-Abdullah coast, southern Iraq. Mesopotamian Journal of Marine Science, 25(1), 75-82**.**

6- **Muttashar, W. R.** (2010). Some geotechnical soil properties of western bank of Khor Al-Zubair coast at Khor Al-Zubair port location, Basrah, Iraq. *Mesopotamian Journal of Marine Science, 25*(2), 124-133.